



Benha University
Benha Faculty of Engineering
Basic Engineering Sciences Department

Novel Multi-Junction Solar Cell Structures **Based on Silicon Substrates**

A thesis Submitted in Partial Fulfillment of the Requirements of
the Ph.D. in Engineering Physics.

By

Eng. Mohamed Okil Shawky Abdel-Wahab

*M.Sc. Degree in Engineering Physics, Department of Basic Engineering
Sciences, Benha Faculty of Engineering, Benha University
(2019)*

Supervised by

Prof. Dr. Tarek Mohammad Abdolkader

*Department of Basic Engineering
Sciences*

*Benha Faculty of Engineering
Benha University*

Prof. Dr. Ahmed Shaker Ahmed Ghazala

*Department of Engineering Physics
and Mathematics*

*Faculty of Engineering
Ain Shams University*

Dr. Ibrahim Sayed Ahmed Ibrahim Maged

Department of Basic Engineering Sciences

*Benha Faculty of Engineering
Benha University*

Benha 2023

The undersigned committee had examined the thesis entitled

***Novel Multi-Junction Solar Cell Structures
Based on Silicon Substrates***

Presented by

Eng. Mohamed Okil Shawky Abdel-Wahab

*M.Sc. Degree in Engineering Physics, Department of Basic Engineering
Sciences, Benha Faculty of Engineering, Benha University
(2019)*

a candidate for the degree of

Ph.D. in Engineering Physics

and hereby certify that it is worthy of acceptance

Prof. Dr. Wael Fikry Farouk Fikry (Committee Chairperson)

Professor Emeritus of Engineering Physics
Faculty of Engineering, Ain Shams University

Prof. Dr. Nadia Hussein Rafat Ahmed (Committee Member)

Professor of Engineering Physics
Faculty of Engineering, Cairo University

Prof. Dr. Tarek Mohammad Abdolkader (Committee Member)

Professor of Engineering Physics
Benha Faculty of Engineering, Benha University

Prof. Dr. Ahmed Shaker Ahmed Ghazala (Committee Member)

Professor of Engineering Physics
Faculty of Engineering, Ain Shams University

Accepted from Basic Engineering Sciences Department

Prof. Dr. (Department Chairman)

Tarek Mohammad Abdolkader Hassan

Accepted from the Postgraduate Affairs

Prof. Dr. (Vice Dean for Postgraduate Studies)

Ashraf Yahya Hassan Ali

Accepted from the Faculty

Prof. Dr. (Dean of the Faculty)

Elsayed Ali Ibrahim Fouad

The undersigned committee had examined the thesis entitled

***Novel Multi-Junction Solar Cell Structures
Based on Silicon Substrates***

Presented by

Eng. Mohamed Okil Shawky Abdel-Wahab

*M.Sc. Degree in Engineering Physics, Department of Basic Engineering
Sciences, Benha Faculty of Engineering, Benha University
(2019)*

a candidate for the degree of
Ph.D. in Engineering Physics

and hereby certify that it is worthy of acceptance

Prof. Dr. Wael Fikry Farouk Fikry (Committee Chairperson)
Professor Emeritus of Engineering Physics
Faculty of Engineering, Ain Shams University

Prof. Dr. Nadia Hussein Rafat Ahmed (Committee Member)
Professor of Engineering Physics
Faculty of Engineering, Cairo University

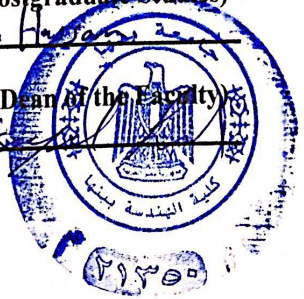
Prof. Dr. Tarek Mohammad Abdolkader (Committee Member)
Professor of Engineering Physics
Benha Faculty of Engineering, Benha University

Prof. Dr. Ahmed Shaker Ahmed Ghazala (Committee Member)
Professor of Engineering Physics
Faculty of Engineering, Ain Shams University

Accepted from Basic Engineering Sciences Department
Prof. Dr. Tarek Mohammad Abdolkader Hassan (Department Chairman)

Accepted from the Postgraduate Affairs
Prof. Dr. Ashraf Yahya Hassan Ali (Vice Dean for Postgraduate Studies)

Accepted from the Faculty
Prof. Dr. Elsayed Ali Ibrahim Fouad (Dean of the Faculty)



ACKNOWLEDGEMENTS

*First and foremost, all praises to Allah for the strengths and His blessing in completing this thesis (**Thanks to Allah**).*

*Words are insufficient in offering my thanks to my advisor who had been a source of inspiration **Prof. Dr. Tarek Mohammad Abdolkader**, Professor of Engineering Physics, Benha Faculty of Engineering, Benha University, for his able guidance and useful suggestions, which helped me in completing this work.*

*I feel immense pleasure in thanking my advisor **Prof. Dr. Ahmed Shaker Ahmed**, Professor of Engineering Physics, Faculty of Engineering, Ain Shams University, for his valuable assistance by having permitted me to carry out this work. I wish to extend my heartfelt gratitude to **Dr. Ibrahim Sayed Ahmed**, whose invaluable guidance has played a pivotal role in shaping this work.*

*I would also like to express my sincere appreciation to **Dr. Marwa Sayed Salem** and **Dr. Mostafa Mohamed Salah** for their valuable assistance.*

*Finally, I would like to thank my family for their continuous support and encouragement. For my parents, who raised me with a love of science and supported me in all my pursuits. I am particularly grateful for my loving, supportive and patient wife **Radwa** and to my beautiful girls, **Karma** and **Tamara**, without their support, sound, and smile I could never have accomplished this work.*

Mohamed Okil

Benha University, Egypt

LIST OF PUBLICATIONS

1. **M. Okil**, M.S. Salem, T.M. Abdolkader, A. Shaker, *From Crystalline to Low-cost Silicon-based Solar Cells : a Review*, Silicon. 14 (2022) 1895–1911.
<https://doi.org/10.1007/s12633-021-01032-4>.
2. **M. Okil**, A. Shaker, I.S. Ahmed, T.M. Abdolkader, M.S. Salem, *Design and analysis of Sb₂S₃/Si thin film tandem solar cell*, Sol. Energy Mater. Sol. Cells. 253 (2023) 112210.
<https://doi.org/10.1016/j.solmat.2023.112210>.
3. **M. Okil**, A. Shaker, I.S. Ahmed, T.M. Abdolkader, M.S. Salem, *Evaluation of a proposed barium di-silicide tandem solar cell using TCAD numerical simulation*, Opt. Quantum Electron. 55 (2023) 475.
<https://doi.org/10.1007/s11082-023-04734-8>.
4. **M. Okil**, A. Shaker, M.M. Salah, T.M. Abdolkader, I.S. Ahmed, *Investigation of Polymer/Si Thin Film Tandem Solar Cell using TCAD Numerical Simulation*, Polymers. 15 (2023) 2049.
<https://doi.org/10.3390/polym15092049>.

TABLE OF CONTENTS

ACKNOWLEDGEMENTS	I
LIST OF PUBLICATIONS	II
TABLE OF CONTENTS	III
LIST OF FIGURES	VI
LIST OF TABLES	XI
LIST OF ABBREVIATIONS AND SYMBOLS	XII
ABSTRACT.....	XV
1 INTRODUCTION.....	1
1.1 Motivation	1
1.2 Problem Statement	1
1.3 Organization of the Thesis	2
2 SOLAR CELLS FUNDAMENTALS AND LITERATURE REVIEW.....	4
2.1 Introduction	4
2.2 Solar Radiation.....	4
2.3 Optical Properties of Solar Cells.....	6
2.4 Electrical Properties of Solar Cells	7
2.5 Literature Review of Solar Cells.....	10
2.6 Summary	18
3 SILVACO ATLAS SIMULATION SOFTWARE	19
3.1 Introduction	19
3.2 Silvaco Simulation Environment	19
3.3 Silvaco Command Group and Statements.....	21
3.3.1 Structure Specification.....	22
3.3.2 Materials Model Specification.....	25

3.3.3	Numerical Method	28
3.3.4	Solution Specification	29
3.3.5	Results Analysis.....	30
3.4	Simulation of Tandem Cells.....	32
3.5	Summary	34
4	BARIUM DI-SILICIDE TANDEM CELL.....	35
4.1	Introduction	35
4.2	Simulator Validation and Sub-Cells Structure	36
4.2.1	Validation of Silvaco Atlas Simulator	36
4.2.2	Structures of Individual Sub-Cells.....	38
4.3	All Barium Di-Silicide Tandem Configuration.....	40
4.3.1	Proposed Tandem Cell	40
4.3.2	Tandem Cell with Variable-bandgap Top Cell	41
4.4	Tandem Cell Optimization	42
4.4.1	The Effect of Absorber Layer Doping	43
4.4.2	The Effect of Absorber Layer Thickness	44
4.4.3	Current Matching Point.....	44
4.4.4	The Defect Density of Absorber Layers	46
4.4.5	Work Functions of The Front and Rear Contacts	48
4.5	Summary	52
5	ANTIMONY SULFIDE/SILICON TANDEM CELL	53
5.1	Introduction	53
5.2	Simulator Validation and Device Structure	54
5.2.1	Validation of Silvaco Atlas Simulator	54
5.2.2	Initial Sb ₂ S ₃ /Si tandem cell.....	59
5.3	Initial Enhancement of Sb ₂ S ₃ Top Cell.....	60

5.4	Tandem Cell Optimization	67
5.4.1	Thickness and Doping of The Top Cell ETL.....	68
5.4.2	Defect Density of The Sb ₂ S ₃ Absorber.....	70
5.4.3	Series Resistance of The Top Cell	72
5.4.4	Thicknesses of The Absorber Layers.....	72
5.4.5	Current Matching Point.....	73
5.5	Summary	77
6	POLYMER/SILICON TANDEM CELL	78
6.1	Introduction	78
6.2	Simulator Validation and Device Structures	79
6.2.1	Validation of Silvaco Atlas Simulator	79
6.2.2	Initial Polymer/Si Tandem Cell	81
6.3	Tandem Cell Optimization	83
6.3.1	Valence Band Offset of The Top Cell	83
6.3.2	Defect Density of The Polymer Absorber	88
6.3.3	Thicknesses of The Absorber Layers.....	89
6.3.4	Current Matching Point.....	90
6.4	Summary	91
7	CONCLUSIONS AND FUTURE WORK.....	93
7.1	Conclusions	93
7.2	Future Work	95
	REFERENCES.....	97

ملخص الرسالة باللغة العربية

LIST OF FIGURES

Figure 2.1 Basic structure of photovoltaic systems [12].	4
Figure 2.2 The power spectral distribution of solar radiation [13].	5
Figure 2.3 Generation process.	7
Figure 2.4 The PV effect	8
Figure 2.5 The I - V characteristics curve for light impact on a solar cell.	8
Figure 2.6 I - V and P - V curves of a solar cell showing I_{sc} , V_{oc} , and FF.	10
Figure 2.7 Tandem solar cell types: (a) two terminals monolithic and (b) four terminals mechanically stacked.	14
Figure 2.8 2T monolithic tandem solar cell: (a) with, and (b) without a tunnel junction, showing the direction of an electrostatic field.	16
Figure 3.1 Silvaco Atlas simulator flowchart indicating the involved input parameters along with the main semiconductor equations.	20
Figure 3.2 Silvaco Atlas command groups and primary statements.	21
Figure 3.3 Example for an Atlas mesh.	23
Figure 3.4 Atlas regions with materials and electrodes defined.	24
Figure 3.5 Atlas doping.	25
Figure 3.6 TONYPLOT samples: (a) J - V , and (b) EQE curves.	31
Figure 3.7 TONYPLOT sample: Recombination rate through an absorber layer.	32
Figure 4.1 (a) Basic layers structure and (b) Energy band diagram after contact at the dark condition of the p -BaSi ₂ / n -Si heterojunction solar cell. (c) Comparison of the simulated J - V characteristics with the measured data [77] under AM 1.5 illumination condition.	38
Figure 4.2 The main configuration of (a) Ba(C _x Si _{1-x}) ₂ top cell, and (b) BaSi ₂ bottom cell. The energy band diagram after contact at the dark condition of (c) Ba(C _x Si _{1-x}) ₂ top cell, and (d) BaSi ₂ bottom cell.	39

Figure 4.3 Schematic representation of a $\text{Ba}(\text{C}_x\text{Si}_{1-x})_2/\text{BaSi}_2$ tandem cell comprising of an n^+pp^+ - $\text{Ba}(\text{C}_x\text{Si}_{1-x})_2$ top sub-cell and an n^+pp^+ - BaSi_2 bottom sub-cell.....	41
Figure 4.4 (a) Illuminated $J-V$, and (b) EQE curves of a $\text{Ba}(\text{C}_x\text{Si}_{1-x})_2/\text{BaSi}_2$ tandem cell.....	42
Figure 4.5 Impact of absorber layer doping on PCE of (a) $\text{Ba}(\text{C}_{0.78}\text{Si}_{0.22})_2$ top cell, and (b) BaSi_2 bottom cell.....	43
Figure 4.6 Tandem efficiency dependency on the thickness of the top and bottom absorber layers.....	44
Figure 4.7 Variation of cell parameters versus top cell absorber thickness from 0.85 to 1.25 μm (a) J_{sc} of top and bottom sub-cells and (b) PCE of the bottom, top and tandem cells.....	45
Figure 4.8 Device characteristics at the current matching point (a) $J-V$ curves, and (b) EQE spectra of the bottom, top, and tandem cells.....	46
Figure 4.9 Contour graphs of TSC performance figure of merit dependency on the defect density of top and bottom absorber layers.....	47
Figure 4.10 The recombination rate behavior drawn at the illuminated short-circuit condition for (a) the top absorber layer and (b) the bottom absorber layer.....	48
Figure 4.11 Schematic energy diagram illustrating Schottky barrier (Φ_b) at (a) the metal/ n^+ - semiconductor interface ($\varphi_m > \varphi_s$), and (b) the metal/ p^+ - semiconductor interface ($\varphi_m < \varphi_s$).....	49
Figure 4.12 Energy band diagram at short-circuit and dark conditions of (a) the top 10 nm for different values of front contact work function, and (b) the bottom 10 nm for distinct values of rear contact work function.....	50
Figure 4.13 Contour graphs of tandem cell performance parameters dependence on front and rear contact work function.....	51
Figure 5.1 (a) Basic layers structure, and (b) Energy band diagram after contact at the dark condition of Sb_2S_3 -based cell. (c) Illuminated $J-V$ and (d) EQE curves of both simulated and experimental Sb_2S_3 cells [90].....	57

Figure 5.2 (a) Basic layers structure, and (b) Energy band profile after contact at the dark condition of a thin c-Si cell. (c) Illuminated $J-V$ and (d) EQE curves of both simulated and experimental thin c-Si cells [97].	58
Figure 5.3 (a) Schematic illustration indicating basic layers, (b) the illuminated $J-V$ characteristics, and (c) EQE curve of an initial Sb_2S_3/Si tandem cell.	60
Figure 5.4 The proposed structure of HTL-free Sb_2S_3 top cell.	61
Figure 5.5 Schematic energy band diagram illustrating various cases of CBOs: (a) a cliff-like band offset, (b) a flat band offset, and (c) a spike-like band offset.	62
Figure 5.6 Variation in (a) E_g and χ and (b) CBO of $ZnO_{1-x}S_x$ depending on the S content percent.	63
Figure 5.7 Performance parameters of $ZnO_{1-x}S_x$ with different S content.	64
Figure 5.8 Energy band diagrams of three various cases of CBOs (a) a cliff-like band appears regarding $ZnO_{0.8}S_{0.2}/Sb_2S_3$, (b) a spike-like band occurs regarding $ZnO_{0.1}S_{0.9}/Sb_2S_3$ and (c) almost flat band regarding $ZnO_{0.2}S_{0.8}/Sb_2S_3$. (d) recombination rate along the Sb_2S_3 absorber layer.	66
Figure 5.9 A comparison between (a) the illuminated $J-V$ and (b) EQE curves for the initial and HTL-free cells using TiO_2 , $ZnO_{0.4}S_{0.6}$, and $ZnO_{0.2}S_{0.8}$ as ETLs.	67
Figure 5.10 The proposed structure utilized in different optimization steps of the Sb_2S_3/Si tandem cell.	68
Figure 5.11 Variation in tandem performance parameters depending on variation in doping concentration of the top cell ETL.	69
Figure 5.12 (a) The electric field distribution, and (b) the spatial distribution of the electron conductivity at the MPP before and after optimizing the top cell ETL.	70
Figure 5.13 Variation in tandem performance parameters depending on the variation of the Sb_2S_3 absorber defect density.	71
Figure 5.14 The generation and recombination rate behavior drawn at the illuminated short-circuit condition for the top absorber layer.	71

Figure 5.15 Variation of tandem performance parameters for different values of external series resistance.	72
Figure 5.16 Tandem efficiency dependency on the thickness of the two absorber films.....	73
Figure 5.17 (a) J_{sc} of front- and rear-cells versus top absorber thickness. (b) $J-V$ characteristics of tandem-, front-, and back-cells under current matching point and 30 μ m bottom cell absorber.	74
Figure 5.18 Calculated efficiency improvements for different cases of tandem cells showing the enhancement relative percentage.	75
Figure 5.19 A comparison between (a) illuminated $J-V$ and (b) EQE curves of an initial and a final optimized tandem cell.....	76
Figure 5.20 (a) J_{sc} of front- and rear-cells versus d of top cell absorber film. (b) $J-V$ characteristics of tandem-, front-, and back-cells under current matching point and 50 μ m bottom cell absorber.	76
Figure 6.1 (a) Basic layers structure, (b) Energy band profile before contact, (c) Comparison of the simulated $J-V$ curve with the measured data [122] under AM 1.5 illumination condition, and (d) EQE of a polymer-based cell.....	81
Figure 6.2 (a) Basic layers structure, (b) Illuminated $J-V$, and (c) EQE curves of an initial polymer/Si TSC.....	82
Figure 6.3 Energy band profile of tandem top cell with initial transport layers (ZnO and PEDOT:PSS).....	83
Figure 6.4 Schematic energy band diagram illustrating various cases of VBOs: (a) a cliff-like band offset, (b) a flat band offset, and (c) a spike-like band offset.....	85
Figure 6.5 A theoretical study for conversion efficiency dependency on VBO of top HTL layer with different electron barriers.	85
Figure 6.6 A comparative analysis between the illuminated $J-V$ characteristics for the initial and TSCs utilizing P3HT, CuO, Cu ₂ O and CBTS as top HTLs.....	86
Figure 6.7 Energy band diagrams of (a) a cliff-like band occurs concerning P3HT/Absorber and (b) a flat band concerning CBTS/Absorber.....	87

Figure 6.8 Variation in tandem performance parameters depending on the variation of the polymer absorber defect density.....	88
Figure 6.9 The generation and recombination rate behavior drawn at the illuminated short-circuit condition for the polymer absorber layer.....	89
Figure 6.10 Tandem efficiency dependency on the thickness of the two absorber films.....	90
Figure 6.11 (a) J_{sc} dependence of the two sub-cells on the top absorber thickness (t_{TA}), (b) illuminated J - V and (c) EQE spectra of the polymer/Si TSC and its sub-cells under CMP.	91

LIST OF TABLES

Table 2.1 Comparison between 2T and 4T tandem solar cells.	15
Table 4.1 Basic parameters of the BaSi ₂ /Si heterojunction cell layers [76–78].	37
Table 4.2 Primary parameters of the sub-cells’ layers used for the design of Ba(C _x Si _{1-x}) ₂ /BaSi ₂ tandem solar cell [58,77,78].	40
Table 4.3 A comparison between the performance metrics for Ba(C _x Si _{1-x}) ₂ /BaSi ₂ tandem cells.	42
Table 4.4 Inorganic rear contact materials showing their work function values [33,83,85–87].	49
Table 5.1 Basic parameters of the Sb ₂ S ₃ and thin c-Si solar cell layers	56
Table 5.2 Defects parameters in the Sb ₂ S ₃ solar cell layers and at the interfaces.	56
Table 5.3 A comparison between the solar cell performance metrics concerning the initial and HTL-free cells when utilizing TiO ₂ , ZnO _{0.4} S _{0.6} , and ZnO _{0.2} S _{0.8} as ETLs.	67
Table 5.4 A comparison between the performance metrics for Sb ₂ S ₃ /Si tandem cells under various optimization steps.	75
Table 6.1 Basic parameters of polymer sub-cell layers.	80
Table 6.2 Defects parameters in the top absorber layer and at the interfaces [19,20].	80
Table 6.3 Basic parameters of various top HTL materials.	86
Table 6.4 PV parameters for the initial and TSCs using P3HT, CuO, Cu ₂ O and CBTS as top HTLs.	86
Table 7.1 A state-of-art comparison between performance parameters of our proposed tandem cells and state-of-the-art tandem cells stated in the literature.	95

LIST OF ABBREVIATIONS AND SYMBOLS

List of Abbreviations:

<i>AM1.5G</i>	Air Mass 1.5 Global
<i>AM0</i>	Air Mass 0
<i>AUGER</i>	Auger Recombination
<i>BaSi₂</i>	Barium Di-Silicide
<i>BaTiO₃</i>	Barium Titanium Oxide
<i>BSF</i>	Back Surface Field
<i>c-Si</i>	Crystalline Silicon
<i>CBO</i>	Conduction Band Offset
<i>CdS</i>	Cadmium Sulfide
<i>CuO</i>	Copper Oxide
<i>CBTS</i>	Copper Barium Thiocyanate
<i>CIGS</i>	Copper Indium Gallium Sulfide
<i>CZTS</i>	Copper Zinc Tin Sulfide
<i>CONMOB</i>	Concentration-Dependent Low-Field Mobility
<i>EB</i>	Electron Barrier
<i>EHP</i>	Electron-Hole Pairs
<i>EQE</i>	External Quantum Efficiency
<i>ETL</i>	Electron Transport Layer
<i>ETM</i>	Electron Transport Material
<i>FF</i>	Fill Factor
<i>FTO</i>	Fluorine Tin Oxide
<i>Fermi</i>	Fermi-Dirac Statistics
<i>HTL</i>	Hole Transport Layer
<i>HTM</i>	Hole Transport Material
<i>ITO</i>	Indium Tin Oxide
<i>J-V</i>	Current Density–Voltage Curve
<i>OPTR</i>	Optical Recombination
<i>PCE</i>	Power Conversion Efficiency
<i>P3HT</i>	Poly-3-Hexylthiophene

<i>PC₇₁BM</i>	Phenyl-C71-Butyric Acid Methyl Ester
<i>PDTBTBz-2F</i>	Poly[(5,6-bis(2-Hexyldecyloxy)Benzo[c][1,2,5]Thiadiazole-4,7-Diyl)-alt-(5,5'-(2,3-Difluoro-1,4-Phenylene) Bis(Thiophen-2-yl))]
<i>PVs</i>	Photovoltaics
<i>PVK</i>	Perovskite
<i>PSC</i>	Perovskite Solar Cell
<i>SC</i>	Solar Cell
<i>Sb₂S₃</i>	Antimony Sulfide
<i>SRH</i>	Shockley–Read–Hall
<i>TSC</i>	Tandem Solar Cell
<i>TRJ</i>	Tunnel Recombination Junction
<i>TCO</i>	Transparent Conducting Oxide
<i>ZnO</i>	Zinc Oxide
<i>ZnOS</i>	Zinc Oxysulfide
<i>ZnSe</i>	Zinc Selenide
<i>2T</i>	Two-Terminal
<i>4T</i>	Four-Terminal

List of Symbols:

α	(cm ⁻¹)	Absorption Coefficient
χ	(eV)	Electron Affinity
ϵ	(F/cm)	Permittivity of The Materials
ϵ_r	(-)	Relative Permittivity
E_g	(eV)	Bandgap Energy
$I(\lambda)$	(W/m ² μm)	Spectral Irradiance
λ	(μm)	Wavelength
$I(x)$	(W/m ²)	Incident Light Intensity
I_L	(mA)	Light-Generated Current
I_{sc}	(mA)	Short-circuit Current
J_{sc}	(mA/cm ²)	Short-circuit Current Density
k	(J/K)	Boltzmann Constant

L_d	(μm)	Minority-carrier Diffusion Length
μ_n	(cm^2/Vs)	Electron and Hole mobility
μ_p		
N_A	(cm^{-3})	Acceptor Concentration
N_c	(cm^{-3})	Effective Conduction Band Density of States
N_D	(cm^{-3})	Donor Concentration
N_t	(cm^{-3})	Defect Density
N_v	(cm^{-3})	Effective Valence Band Density
P_{in}	W/m^2	Incident Power
q	(C)	Electron Charge
G	($\text{cm}^{-3} \text{s}^{-1}$)	Generation Rate
R	($\text{cm}^{-3} \text{s}^{-1}$)	Recombination Rate
R_s	($\Omega \text{ cm}^2$)	External Series Resistance
R_{sh}	($\Omega \text{ cm}^2$)	External Shunt Resistance
t_{TA}	(nm)	Top Absorber Thickness
t_{BA}	(μm)	Bottom Absorber Thickness
T	(K)	Temperature
V_{oc}	(V)	Open-circuit Voltage
V_T	(V)	Thermal Voltage

ABSTRACT

Solar cells have emerged as a popular and sustainable source of energy in recent years. These cells convert sunlight directly into electricity and can be used to power a wide range of applications, from small household appliances to large industrial complexes. As a result, they are becoming an increasingly popular choice for both residential and commercial applications, contributing to a cleaner and more sustainable future.

The present thesis is devoted to investigating three novel monolithic tandem structures using TCAD numerical simulation. The proposed cells are:

(i) A 2T (two-terminal) monolithic all-BaSi₂ (Barium di-silicide) tandem cell which combines a BaSi₂ bottom sub-cell with a bandgap of 1.3 eV, and a Ba(C_xSi_{1-x})₂ top sub-cell with a tunable bandgap. It was found that a bandgap of 1.8 eV, which corresponds to $x = 0.78$, is the optimum choice to obtain the maximum initial power conversion efficiency (PCE) of 30%. Then, the tandem performance is optimized by investigating the impact of doping and the thickness of both absorber layers. Further, the current matching point is monitored whilst altering the thickness of the top cell in the range (0.85 – 1.25 μm) resulting in PCE = 32.83%. Additionally, we have explored the influence of the defect density in the absorbers, and the work function of contacts on the performance parameters.

(ii) A 2T monolithic Sb₂S₃/Si tandem cell which combines a Sb₂S₃ (Antimony sulfide) top sub-cell with a bandgap of 1.7 eV and a thin c-Si bottom sub-cell with a bandgap of 1.12 eV. The calibrated standalone top and bottom cells provide a PCE of 4.31% and 14.26%, respectively. Upon incorporating the two cells into a monolithic tandem cell, a PCE of 10.10% is attained, implying that the top cell should be optimized in order to surpass the PCE of the bottom cell. Thus, the Sb₂S₃ cell is optimized by designing the cell without the organic hole transport layer (HTL) and engineering the conduction band offset (CBO)

between the electron transport layer (ETL) and the Sb_2S_3 absorber. Then, the tandem structure is optimized starting from the ETL thickness and doping concentration. Also, the impact of changing the absorber defect density and the series resistance of the top cell on the tandem performance is investigated to demonstrate the maximum available PCE. At reduced defect density and series resistance, the overall efficiency of the tandem cell is improved to 19.51%. Furthermore, we explored the impact of top and bottom absorber thicknesses on TSC working metrics. Additionally, we have inspected the consequence of the top absorber thickness on TSC performance parameters for two cases of bottom absorber thickness (t_{Si}). At the designed matching point for each case, the optimum efficiency was achieved giving $J_{\text{sc}} = 17.24 \text{ mA/cm}^2$, and $\text{PCE} = 23.25\%$ for $t_{\text{Si}} = 30 \text{ }\mu\text{m}$, while $J_{\text{sc}} = 18.04 \text{ mA/cm}^2$, and $\text{PCE} = 24.34\%$ for $t_{\text{Si}} = 50 \text{ }\mu\text{m}$.

(iii) A 2T monolithic polymer/Si tandem cell comprises a polymer-based top sub-cell and a thin c-Si bottom sub-cell. The photoactive layer of the top sub-cell is a blend of PDTBTBz-2F (poly[(5,6-bis(2-hexyldecyloxy)benzo[c][1,2,5]thiadiazole-4,7-diyl)-*alt*-(5,5'-(2,3-difluoro-1,4-phenylene)bis(thiophen-2-yl))]) as a polymer donor and PC_{71}BM (phenyl-C71-butyric acid methyl ester) as a fullerene acceptor. Initially, a calibration of the two sub-cells is carried out against experimental studies, providing a PCE of 10% for the top sub-cell and 14.26% for the bottom sub-cell. Upon incorporating into a tandem structure, the resulting cell shows a PCE of 16.58% and a J_{sc} of 13.39 mA/cm^2 . Then, the tandem performance is optimized by controlling the valence band offset (VBO) of the top cell. Furthermore, we inspected the influences of the top absorber defect density as well as both absorber thicknesses for better tandem performance. After optimizing and designing the current matching point, the J_{sc} and PCE of the tandem cell are enhanced to 16.42 mA/cm^2 and 24.21%, respectively.

These simulation studies are intended to provide tandem configurations that are based on an all-thin-film design which may be suitable for applications like flexible electronics.

This page is intentionally left blank

CHAPTER 1

INTRODUCTION

This page is intentionally left blank

CHAPTER 1

INTRODUCTION

1.1 Motivation

Currently, a widespread belief is that clean energy sources can substitute fossil fuels. Among these renewable options, solar energy is considered an efficient replacement source [1]. Since the 1970s, photovoltaics (PVs) have demonstrated the potential to supply a portion of electricity needs without relying on fossil fuels. PVs benefit from mitigating the hazards associated with traditional power production methods. As sunlight is accessible to everyone, PVs can provide electricity to those living in remote areas beyond the reach of the electric grid. PVs have powered satellites for more than six decades. The first silicon-based solar cell, which boasted a power conversion efficiency (PCE) of 6%, was developed in Bell Labs in 1954 [2]. The first commercial silicon solar cell with a PCE of 2% was introduced in 1955. Unlike batteries, solar cells do not require charging [3].

1.2 Problem Statement

Nowadays, the energy demand is sharply increased [1,4]. Solar cells (SCs) are a promising solution to meet this demand cleanly and sustainably [5]. Single-junction solar cells made from silicon dominate the solar cell industry, accounting for 90% of it [6–8]. Despite their high efficiencies of over 25%, these cells are relatively expensive to produce. Therefore, there is a need to develop solar cell structures and techniques based on low-cost and readily available materials, with easy fabrication processes [6]. The performance of a single-junction solar cell is restricted as it can solely capture photons with energies equivalent to or exceeding the energy gap (E_g) of the material employed. However, tandem (multi-junction) PV systems are considered a promising solution

to overcome this limitation. Such systems consist of sub-cells that absorb diverse wavelengths of the light spectrum, leading to better performance than single-junction solar cells [9].

Tandem cells have not yet achieved their maximum PCE, and certain materials are more appropriate for serving as the absorber layer on the top and/or bottom sub-cells [10]. Moreover, there are numerous potential combinations of top and bottom sub-cells that could result in effective tandem cell structures. Designing these structures prior to fabrication can save time and resources [10].

This thesis offers a potential solution to address these challenges by proposing the design of tandem solar cells.

In this thesis, the main contributions are:

- Calibration of some single-junction cells against experimental studies.
- Modeling and simulation of novel tandem solar cells.
- Using new efficient materials as ETL and HTL in the Sb_2S_3 and polymer-based solar cells instead of the conventional materials.
- Propose an HTL-free Sb_2S_3 cell with high efficiency and good stability.
- Propose and investigate a polymer/Si tandem cell for the first time.
- Investigating and optimizing the significant parameters of the used materials and studying their impact on the performance parameters.
- Designing three tandem solar cells with good stability and PCEs up to 34.25%.

1.3 Organization of the Thesis

The rest of this thesis is organized as follows:

Chapter 2: presents the solar cell fundamentals and literature review on tandem solar cells.

Chapter 3: illustrates the working mechanism of the used simulator, Silvaco ATLAS, and its various features.

Chapter 4: presents the proposed design and various optimization steps of all-BaSi₂ tandem cell.

Chapter 5: presents the calibration of standalone sub-cells (Sb₂S₃ and c-Si), the proposed design and different optimization stages of Sb₂S₃/Si tandem cell.

Chapter 6: presents the calibration of standalone polymer-based sub-cell, the proposed design and different optimization stages of polymer/Si tandem cell.

Chapter 7: concludes the overall work in this thesis and suggests future work.

This page is intentionally left blank

CHAPTER 2
SOLAR CELLS FUNDAMENTALS
AND LITERATURE REVIEW

This page is intentionally left blank

CHAPTER 2

SOLAR CELLS FUNDAMENTALS AND LITERATURE REVIEW

2.1 Introduction

The sun provides the primary source of energy for our planet, with a power of 10^{17} W [11]. However, due to the low density and variability of solar radiation, there is no direct method to utilize it effectively. **Figure 2.1** depicts the block diagram of a PV system, where PV arrays transform solar radiation into direct current (DC). Each array is composed of modules that consist of a matrix of SCs connected in parallel and series. Therefore, the solar cell serves as the fundamental unit of PV systems. Battery storage is necessary for times when sunlight is unavailable, and the AC load requires a power conditioning circuit that uses inverters to convert DC to AC.

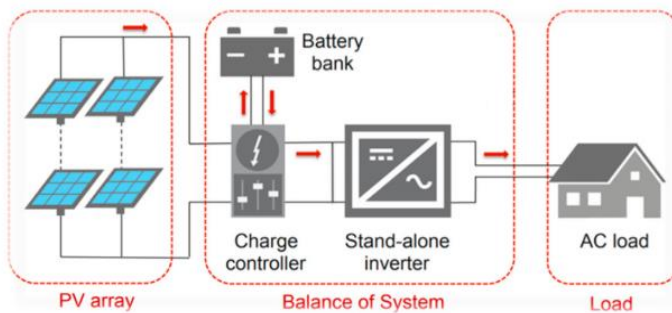


Figure 2.1 Basic structure of photovoltaic systems [12].

The remainder of this chapter covers the basics of solar cells, starting with solar radiation, followed by the optical and electrical parameters of solar cells, and concluding with a literature review on tandem solar cells.

2.2 Solar Radiation

Solar radiation serves as the incident power (P_{in}) to the SCs. The sun's surface temperature is 6000 K, and the solar constant represents the received

power of solar radiation at a unit area perpendicular to the radiation at the mean sun-earth distance, defined as one astronomical unit (AU). AU is approximately 1.5×10^{11} m, and the solar constant is around 1.4 kW/m^2 . At other distances, the solar radiation intensity is expressed in terms of the solar constant. In space, the solar cells receive illumination from the air mass zero (AM0) spectrum, which is equivalent to 1 solar constant. The spectrum of solar radiation contains a broad range of wavelengths. **Figure 2.2** shows the power spectral distribution of solar radiation, where $I(\lambda)$ and λ represent the spectral irradiance and wavelength, respectively. The spectral irradiance $I(\lambda)$ is the solar power density at a certain wavelength expressed in units of $\text{W/m}^2\mu\text{m}$ and is given in **Eq. 2.1**, where $\delta\lambda$ is the respective wavelength range in μm .

$$I(\lambda) = \frac{P(\lambda)}{A \delta\lambda} \quad (2.1)$$

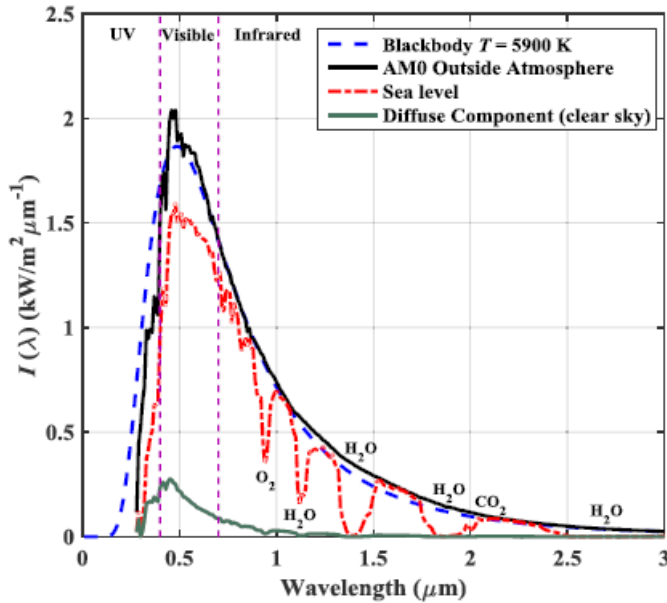


Figure 2.2 The power spectral distribution of solar radiation [13].

The spectral irradiance of solar radiation is highest at a wavelength of 0.5 μm , as shown in **Figure 2.2**. However, the irradiance decreases due to absorption and scattering by air molecules. The black dashed line in the figure represents black body radiation at a temperature of 5900 K. After passing through one air mass perpendicular to the earth (zenith), the solar power intensity is referred to as AM1, which has a value of 925 W/m^2 and is determined by the angle of incidence (θ) with respect to the earth's surface, as given by **Eq. 2.2**. The performance of solar cells is typically measured under the air mass 1.5 global (AM1.5G) spectrum with an incident power of 1000 W/m^2 .

$$AM = \frac{1}{\cos(\theta)} \quad (2.2)$$

2.3 Optical Properties of Solar Cells

When solar radiation reaches a solar cell, it is divided into three parts: reflection, absorption, and transmission [13]. The energy of the photons in the light can be expressed in terms of their wavelength and speed of light using **Eq. 2.3**. As shown, The photon energy (E_{ph}) is inversely proportional to its wavelength. The absorption of light in a solar cell is determined by the absorption coefficient of the materials used in the cell. The absorption coefficient and the light intensity $I(x)$ as a function of the position (x) and the absorption coefficient (α) is given in **Eq. 2.4**. The light intensity decreases exponentially with x . When the photon energy is equal to or greater than the energy of the absorber material in the solar cell, the photons can generate electron-hole pairs, this process is known as the generation process, as illustrated in **Figure 2.3**.

$$E_{\text{ph}} = \frac{hc}{\lambda} \quad (2.3)$$

$$I(x) = I_0 \exp(-\alpha x) \quad (2.4)$$

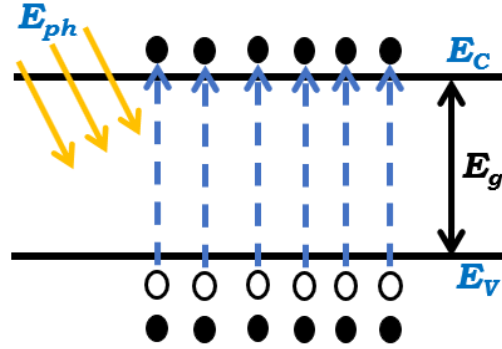


Figure 2.3 Generation process.

2.4 Electrical Properties of Solar Cells

The process of generating an electric field in a solar cell during illumination is known as the PV effect, as shown in **Figure 2.4**. When photons pass through the solar cell, electron-hole pairs are generated if their energy is sufficient, as discussed earlier. These pairs are separated by the electric field created within the solar cell, with the electrons and holes moving towards the n -side and p -side of the cell, respectively. These carriers then flow to the outer load circuit. However, carriers generated outside the field region diffuse towards the field region. Only carriers within a diffusion length from the edges succeed in reaching the field region. Carriers generated outside these diffusion regions are lost due to recombination.

The current–voltage (I – V) characteristics curve of a solar cell is the most critical measurable output and is given by the equation:

$$I = I_L - I_o \left(\exp \left(\frac{V + IR_s}{nV_T} \right) - 1 \right) - \frac{V + IR_s}{R_{sh}} \quad (2.5)$$

where I_L is the light-generated current, n is the ideality factor, R_s is the series resistance, R_{sh} is the shunt resistance, and V_T is the thermal voltage given by the equation:

$$V_T = \frac{kT}{q} \quad (2.6)$$

where k is the Boltzmann Constant, T is the temperature in Kelvin (K), and q is the electron charge (1.6×10^{-19} C). The I - V curve helps to extract key performance metrics such as short-circuit current, open-circuit voltage, fill factor, and power conversion efficiency. **Figure 2.5** shows the impact of light on a solar cell and the corresponding I - V characteristics curve.

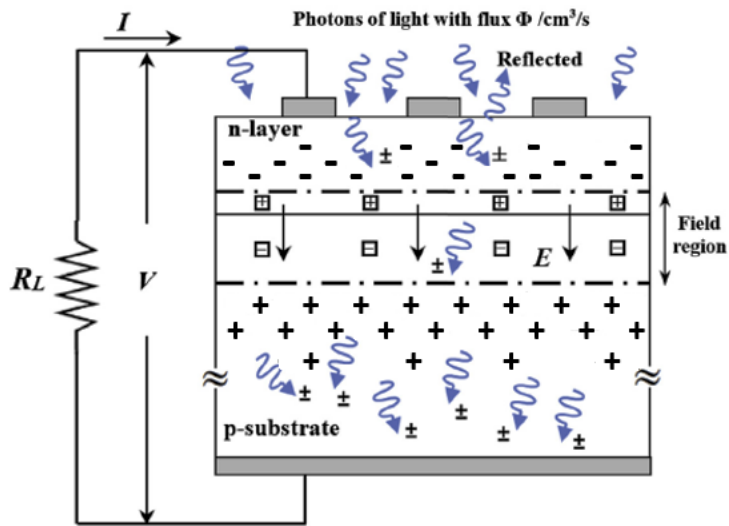


Figure 2.4 The PV effect .

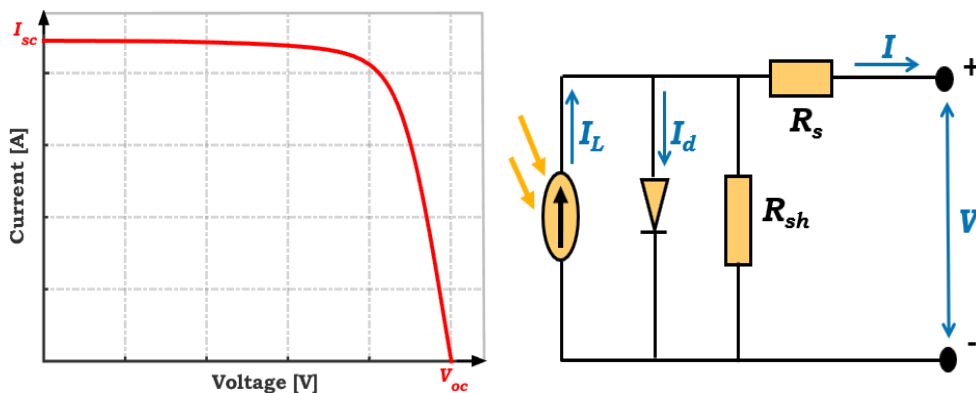


Figure 2.5 The I - V characteristics curve for light impact on a solar cell.

The short-circuit current (I_{sc}) is the maximum possible current from a solar cell when there is no voltage drop across it and it is short-circuited [14]. In ideal solar cells, the short circuit current is equal to the light current. The short-circuit current density (J_{sc}), obtained by dividing I_{sc} by the top surface area of the solar cell, is a more commonly used term than I_{sc} . The open-circuit voltage (V_{oc}) is the maximum possible voltage from a solar cell when the net current is zero, and it is caused by the bias of the cell junction with the light-generated current [14]. V_{oc} is calculated using the equation:

$$V_{oc} \approx nV_T \ln \frac{I_L}{I_o} \quad (2.7)$$

At either short-circuit or open-circuit conditions, the extracted power from the solar cell is equal to zero. The maximum output power (P_{max}) is attained at a certain current and voltage values of I_{mp} and V_{mp} , respectively and can be calculated using **Eq. 2.8**. The fill factor (FF) is the ratio between the maximum power and the product of I_{sc} and V_{oc} . FF measures the squareness of the $I-V$ curve, and ideally, it should be equal to unity. FF can be calculated using **Eq. 2.9**. The power conversion efficiency (PCE) is the ratio between the maximum output power of the solar cell and its input power (P_{in}) as shown in **Eq. 2.10**, and it is the most used metric for comparing the performance of solar cells [14]. This efficiency depends on several parameters such as the input spectrum, layer thickness, temperature. **Figure 2.6** illustrates all the other performance parameters.

$$p_{max} = V_{mp} I_{mp} \quad (2.8)$$

$$FF = \frac{p_{max}}{V_{oc} I_{sc}} \quad (2.9)$$

$$PCE = \frac{P_{max}}{P_{in}} \quad (2.10)$$

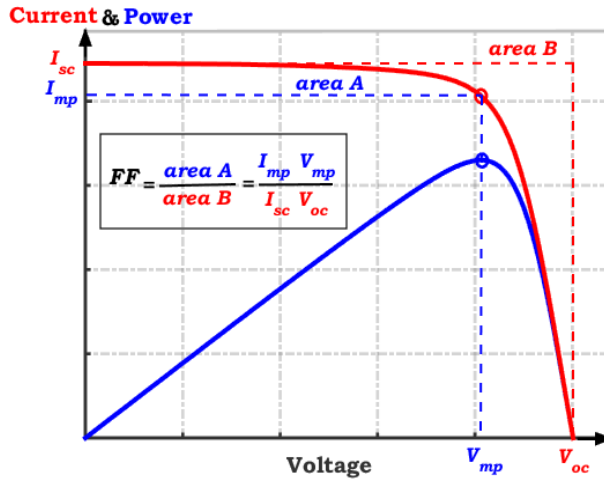


Figure 2.6 I - V and P - V curves of a solar cell showing I_{sc} , V_{oc} , and FF.

2.5 Literature Review of Solar Cells

Photovoltaics propose promising solutions to handle the energy demand issue. Various types of solar cells have been widely presented and published. The central goal of recent research is to achieve efficient solar cells with low cost of fabrication [8,13,15]. The generations of solar cells could be summarized in four generations. Firstly, a generation based on the crystalline-silicon (c-Si), and gallium arsenide. Secondly, a generation based on amorphous and microcrystalline thin films silicon, copper indium gallium selenide (CIGS), cadmium sulfide (CdS), and cadmium telluride (CdTe). New compounds like organics, polymers and perovskites, and structures like tandem solar cells (TSCs) are the base of the third generation [16–20]. Finally, the fourth generation includes thin film polymers along with inorganic nanostructures such as metal oxides and metal nanoparticles or organic-based nanomaterials such as graphene, carbon nanotubes and graphene derivatives [3,21,22]. According to the non-toxicity, stability, abundancy, and well-known technology of silicon, silicon solar cells demonstrate the highest share of solar cells' market. PCE of silicon solar cells exceeds 26% [23]. Additionally, many efforts have been conducted in order to achieve low-cost silicon solar cells [24–28]. Recently, a

generation based on the insertion of the stable inorganic generation into the flexible, and low-cost polymers like metal-nanoparticles, and metal-oxides has been developed.

There has been extensive research and development into various types of solar cell technologies, including thin-film solar cells (TFSCs). TFSCs are a cost-effective solution due to their low material consumption. They consist of multiple semiconducting layers that can be applied to different substrates, such as plastic, glass, or metal. As a result of intensive research and development efforts in material exploration and device engineering, several new TFSC technologies have emerged. These technologies include, among others, barium di-silicide (BaSi_2), antimony sulfide (Sb_2S_3), bulk heterojunction polymer and perovskite solar cells (PSCs).

Perovskite solar cells have low-cost, simple fabrication processes, and high performance, which allowed them to be extensively employed [29]. Also, PSCs have unique electronic properties such as a tunable bandgap, a high V_{oc} , low-cost deposition methods, large charge carrier diffusion distances, and low-recombination speeds. Because of these characteristics, the PSCs are an excellent candidate for traditional solar cells. The perovskite substance has the composition ABX_3 . The first perovskite photovoltaic solar cell of barium titanium oxide (BaTiO_3) was observed in 1956 [30]. From 2009 to 2016, PSCs manufactured from hybrid-halide materials of methylammonium lead-halides (MAPbX_3) by various designs, satisfied an enhanced the PCE which is around 25% [31]. The development of PSC in recent years has produced simulated PCE results of up to more than 30% [32]. The majority of high-performance perovskite cells are lead-based; however, the toxicity of such cells is a severe issue that limits their application [33].

Notably, an ultimate alternate absorbing material ought to have a high absorption coefficient (α), high minority-carrier lifetime, and suitable bandgap

for use as a single junction or in tandem cells. These characteristics are shared by orthorhombic BaSi₂, which is stable, environmentally friendly, and has abundant constituent elements [34]. BaSi₂ has a 1.3 eV bandgap, and its α value is $3 \times 10^4 \text{ cm}^{-1}$ at 1.5 eV [35], almost forty times that of c-Si. The undoped BaSi₂ is an *n*-type semiconductor that has an approximate electron density of about $5 \times 10^{15} \text{ cm}^{-3}$ [36], roughly 10 μm minority-carrier diffusion length (L_d) [37], and about 10 μs minority-carrier lifetime [38] that is appropriate for TFSC applications. Due to the reported values of L_d and α , an efficiency that is higher than 25% could be estimated from the BaSi₂ *p*-*n* junction diode having a thickness of 2 μm [34]. An efficiency of 23.17% has been achieved from *p*-type Zn₃P₂/*n*-type BaSi₂ heterojunction thin-film cell [39]. In 2018, Y. Tian et al. fabricated polycrystalline BaSi₂ thin films via an industrially applicable sputtering process [40]. Recently, Y. Tian et al. deposited a Si/BaSi₂/Si heterostructure by magnetron sputtering with different Si layer thicknesses and it was found that the thickness of the Si layer has a great effect on oxide layer growth, Ba depletion, and multiphase Si layer formation at the heterojunction interfaces [41]. These findings contribute to the development of BaSi₂/Si heterojunction solar cells and may allow the introduction of BaSi₂ to be used in conjunction with other materials thanks to the progress in material quality. To increase the viability of BaSi₂ to be used in tandem cells, bandgap engineering should be performed to increase the E_g from its initial value of 1.3 eV. By substituting part of Ba with Sr atoms to create Ba_{1-x}Sr_xSi₂, the E_g of the compound can be adjusted to 1.4 eV [42]. In the meantime, when replacing some Si atoms with isoelectric C, the corresponding bandgap of Ba(C_xSi_{1-x})₂ can steadily increase from 1.3 to 3 eV [43].

In addition, Sb₂S₃ is one of the most appropriate top cell candidates for next-generation TSCs owing to its desired broad bandgap of 1.7 eV [44], intrinsic stability [45,46], non-toxicity, and less expensive constituent elements.

As well, it has been theoretically shown that combining c-Si as a bottom sub-cell along with a top sub-cell whose material bandgap is 1.72 eV in a 2T TSC, an efficiency near 43% can be reached [47]. Consequently, Sb_2S_3 , whose bandgap is 1.7 eV, can be a proper top cell partner combined with an optimal bottom cell like silicon in TSCs. Recently, Bulk heterojunction polymer solar cells are gaining attention as they have the potential to provide flexible, lightweight, and cost-effective alternatives to silicon-based solar cells [48]. In 2014, Ambade et al. have been working on improving the charge selectivity of inverted polymer-based solar cells by inserting a sub-monolayer of dyes containing functional cyano-carboxylic at the interface between the inorganic metal oxide (ZnO) and organic active layer, resulting in an improved conversion efficiency to 3.52% [49]. Y. Yan et al. recently synthesized and used TiO_2 nanoparticles as the electron-transport layer in single-junction inverted polymer solar cells, resulting in a high FF of 72% and the best PCE of 10.55%, making it one of the best single-junction inverted polymer solar cells ever reported, with superior stability under ambient conditions when compared to conventional device configuration [50].

The PCE of a single-junction solar cell has limitations since it can only convert photons with energies equal to or greater than the energy gap of the materials employed [13]. This implies that any remaining incident photons are not utilized and are ineffectively wasted. Additionally, photons with higher energies dissipate their excess energy through thermalization. In 1961, Shockley and Queisser computed that a maximum PCE of 33.7% could be achieved with a bandgap of 1.34 eV [51]. Tandem solar cells offer a solution to this limitation by utilizing sub-cells that can absorb a range of wavelengths [13]. These solar cells consist of more than one absorber layer, allowing them to overcome the constraint of single-junction cells. The top sub-cell, which has a high energy gap, absorbs the shorter wavelength radiation, while the longer

wavelength radiation that is not absorbed by the top sub-cell is transmitted to the bottom cell [9]. The maximum theoretical limit of multi-junction solar cells with an infinite number of sub-cells is a PCE of 68.2% [52].

Schematically, tandem devices can be designed in various configurations such as two-terminal (2T) and four-terminal (4T) configurations, as shown in **Figure 2.7**. The 2T tandem configuration combines wide and narrow bandgap p - n junctions which serve as the top and bottom cells, respectively. The two sub-cells are electrically and optically connected. However, although the two cells of the 4T tandem device are electrically separated, they are optically coupled to combine their full output power [53]. A full comparison between both configurations is presented in **Table 2.1**.

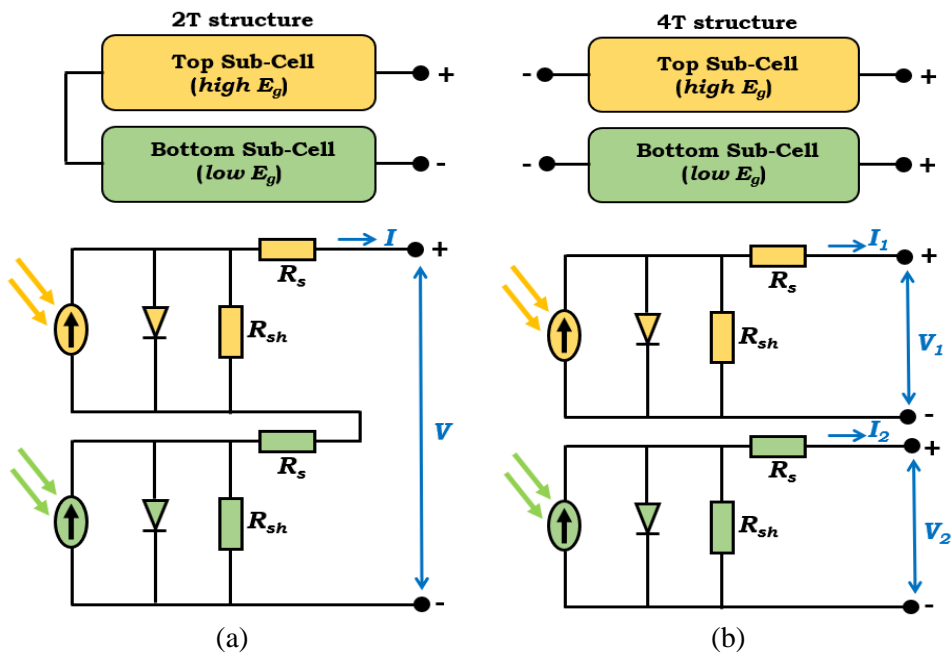


Figure 2.7 Tandem solar cell types: (a) two terminals monolithic and (b) four terminals mechanically stacked.

Table 2.1 Comparison between 2T and 4T tandem solar cells.

	2T	4T
Optical coupling	Yes	Yes
Electrical coupling	Yes, series connection	No
Fabrication	Top cell is fabricated directly on the top of bottom cell.	Sub-cells are fabricated separately.
Advantages	<ol style="list-style-type: none"> 1. It converts larger share of the solar irradiance to electricity. 2. It requires less processing step and less contact layers. 3. It provides larger output voltage than each of the sub-cell. 4. Less parasitic absorption from glass substrate. 	<ol style="list-style-type: none"> 1. It converts larger share of the solar irradiance to electricity. 2. Current matching is not required and the sub-cells can be optimized independently. 3. Easy to maintain and fix by replacing a new sub-cell if it is not working. 4. The overall device efficiency is not sensitive to solar spectrum.
Disadvantages	<ol style="list-style-type: none"> 1. Current matching between the sub-cells is required. 2. Solution-processed deposition may not be applicable to fabricate a top sub-cell on a bottom one. 3. Lifetime of the tandem cell will be determined by the lowest stable sub-cell. 	<ol style="list-style-type: none"> 1. More processing steps since the sub-cells are fabricated separately. 2. Conductive glass substrate of the top sub-cell will cause optical losses due to its parasitic absorption.

To obtain a good 2T monolithic TSC, the junction between the two sub-cells is a crucial feature. This junction, usually named tunnel recombination junction (TRJ) interconnects the sub-cells and prevent the formation of parasitic $p-n$ junctions [54], as illustrating in **Figure 2.8**. The parasitic junction generates an electrostatic field that opposes carrier flow towards the contacts, preventing the cell from producing any current. The practical design of the tunnel junction is a critical task in order to maintain proper functionality leading to the enhancement of the tandem performance [55]. The junction has to be transparent, and it should not absorb any part of the input radiation spectrum reaching the bottom cell. Such requirements have been met by fulfilling two design conditions: (1) the tunnel junction has to be heavily doped, and (2) both sides of the junction should be very thin in the nanometer range [56]. The

heavily-doped layers form intermediate junctions between the sub-cells and the tunnel junction, conducting the current from the p to the p^+ regions and from the n^+ to the n regions, as shown in **Figure 2.8(a)**. Furthermore, the 2T tandem cell current is controlled by the smaller current transporting through either the top or the bottom sub-cell. Therefore, the current matching condition should be maintained to minimize the current loss.

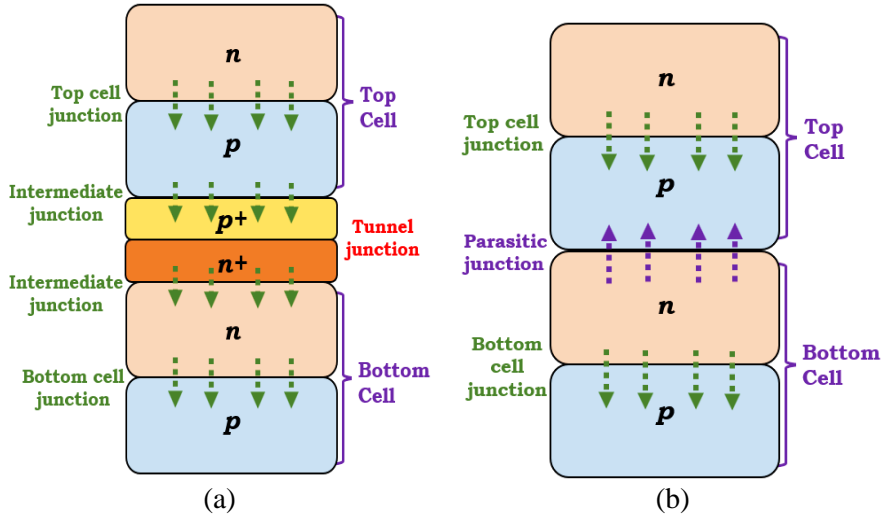


Figure 2.8 2T monolithic tandem solar cell: (a) with, and (b) without a tunnel junction, showing the direction of an electrostatic field.

Although numerous combinations of top and bottom sub-cells have been provided in the literature, only two studies have investigated BaSi₂ as a tandem sub-cell. A perovskite/ BaSi₂ thin film tandem cell with a PCE up to 28% was recorded in 2016 [57]. It was shown that a 2- μ m thick BaSi₂-based thin-film solar cell can exhibit an implied photo-current density equal to 41.1 mA/cm², which is higher than that of a state-of-the-art wafer-based c-Si hetero-junction solar cell. This performance makes BaSi₂ an attractive absorber for high-performance thin-film and multi-junction solar cells. In 2019, Tianguo have investigated Ba(C_xSi_{1-x})₂ (1.7eV)/c-Si (1.12eV) tandem solar cell [58]. The cur-

rent matching point was found with $J_{sc} = 17.6 \text{ mA/cm}^2$ at a top absorber thickness of 500 nm. At this point, the PCE reached a maximum value of 30.3% with an $V_{oc} = 1.94 \text{ V}$. Based on these promising results, we can state that BaSi_2 may be a very good candidate to be used in thin-film and tandem solar cell applications in recent future. Consequently, an efficient all- BaSi_2 tandem cell is proposed in this work.

A few studies have recently investigated Sb_2S_3 as a top cell in Si-based TSCs [59–61]. In 2016, Gao et al. presented the first study on Sb_2S_3 as a top absorber, in which they deposited Sb_2S_3 on *n*-type Si-substrates using reactive sputtering at 350 °C. They concluded that Sb_2S_3 meets all requirements for a potential top sub-cell in silicon-based TSCs [61]. Recently, a tandem cell based on Sb_2S_3 and Sb_2Se_3 as top and bottom cells was fabricated and a PCE of 7.93% was reported which surpasses the independently top Sb_2S_3 and bottom Sb_2Se_3 cells [62]. This experimental study proves the suitability of Sb_2S_3 -based solar cell as a top cell of TSC and establishes a proof of concept. As a result, a 2T monolithic $\text{Sb}_2\text{S}_3/\text{Si}$ tandem cell is investigated in this work.

Many studies have recently investigated polymer-based tandem cells using CIGS and Lead-free perovskite cells such as All-polymer/CIGS [19] and Lead-free perovskite/organic tandem [20]. However, there is no research report on tandem devices based on organic polymers and c-Si to the best of our knowledge except H. Park et al. in 2021 [63]. They experimentally investigated polymer-based organic/c-Si tandem solar cells for the first time with a PCE of 8.32% for 2-T cells and 15.25% for 4-T cells [63]. Thus, the integration of polymer and Silicon in a TSC deserves more attention. Implementing polymer/silicon TSC can achieve higher efficiencies than single-junction solar cells. In addition to reduced material cost compared to other Silicon based TSCs, flexibility and lightweight are other advantages that may make thin film

polymer/silicon TSC suitable for a wider range of applications. In this work, we propose and investigate a polymer/Si thin-film tandem cell.

2.6 Summary

This chapter began with a discussion of the fundamental structure of photovoltaic systems. After that, solar radiation and the optical and electrical properties of solar cells are introduced. There is also an explanation of the PV effect and the output metrics of the solar cells. Finally, various types of thin-film solar cells are demonstrated, focusing on tandem solar cells. This work's significance has been highlighted.

This page is intentionally left blank

CHAPTER 3
SILVACO ATLAS
SIMULATION SOFTWARE

This page is intentionally left blank

CHAPTER 3

SILVACO ATLAS SIMULATION SOFTWARE

3.1 Introduction

Most research centers and PV cell manufacturers follow the construction of experimental specimens to evaluate cell performance. However, this method can be both time-consuming and expensive. In contrast, modeling with software provides a relatively fast, consistent, and cost-effective means of designing solar cells. Through modeling and simulation, thousands of combinations can be explored prior to the actual fabrication of specimens.

This work focuses on utilizing the Silvaco ATLAS simulation software to model tandem solar cells and assess their performances under different variations of cell parameters. All tandems used in this work are based on Silicon substrate. This chapter presents Silvaco Atlas and its various features.

3.2 Silvaco Simulation Environment

To simulate a PV cell in ATLAS, a text input deck called DeckBuild is utilized, which creates a run-time environment where various parameters related to the cell's structure and composition must be defined. The first step in the simulation process is to define the cell's structure. This involves specifying the physical dimensions and thicknesses of the different cell layers and building a mesh with the suitable spacing in different regions of the device. This is an indispensable step that should be made carefully because, at each grid point, known as nodes, a set of differential equations are solved to simulate carrier transport and describe the cell's behavior. The resolution of the simulation is determined by the density of the mesh's triangles, which affects the accuracy of cell representation and the time required for program iterations. ATLAS is a physically-based device simulator, so, the second step is the definition of the

cell's composition and bias conditions. The mesh is divided into regions, with different materials assigned to each. Electrodes are then assigned to obtain the device's electrical characteristics or specific regions [64]. All defined materials must be associated with doping values and material properties should be declared for the most accurate simulation. The user must then choose among different models to find the most suitable one to evaluate the structure and achieve a better outline for the specific cell simulation. A light beam is specified to illuminate the cell, simulating different regions of the solar spectrum depending on the selected beam. The user must also choose a method from the various options provided by the ATLAS library for solving the differential equations through which the cell's operating characteristics arise. The simulation's output can be saved in a log file and used to create plots using TONYLOT, the interactive graphics and analysis package included in the program. **Figure 3.1** depicts a flowchart of the Atlas simulator, illustrating the main semiconductor equations and the necessary input physical and geometrical parameters.

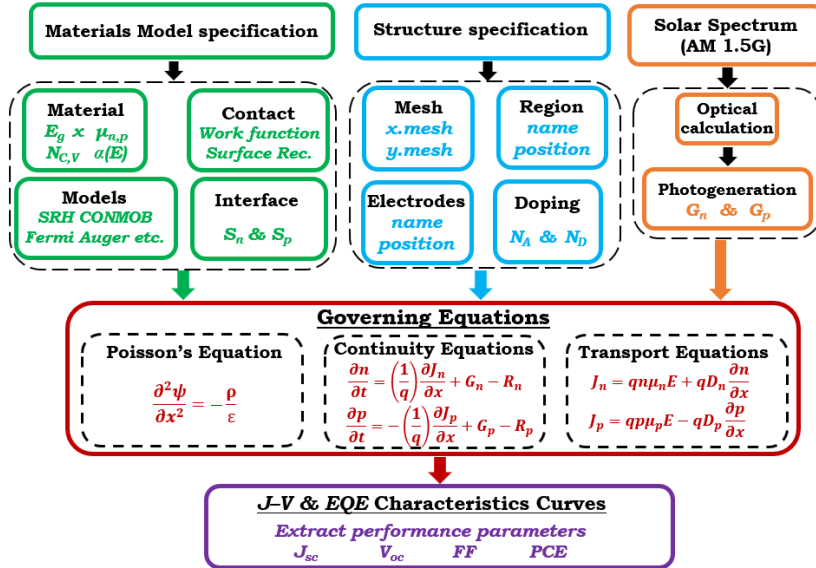


Figure 3.1 Silvaco Atlas simulator flowchart indicating the involved input parameters along with the main semiconductor equations.

3.3 Silvaco Atlas Command Group and Statements

Initiating Silvaco Atlas, input files are first created using DeckBuild. The command to execute Atlas is "go atlas" and the input file must follow a specific pattern, as outlined in the command groups listed in **Figure 3.2**.

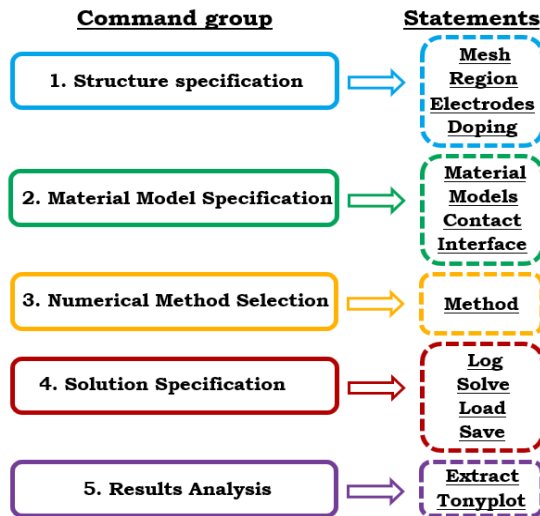


Figure 3.2 Silvaco Atlas command groups and primary statements.

Atlas conforms to a specific format for both statements and parameters:

<STATEMENT> <PARAMETER> = <Value>

The subsequent line of code serves as an illustration:

```
DOPING REGION = 1 P.TYPE UNIFORM \
      CONCENTRATION = 2e19 OUTFILE = HTL.DOP
```

An example line of code in Atlas involves the statement "DOPING" and its associated parameters: REGION, P.TYPE, UNIFORM, CONCENTRATION, and OUTFILE. The keyword statement must precede statements, but the order of parameters within statements is insignificant. In addition, the <Value> of each parameter can be of four different types: Integer, Logical, real, and Character. The Integer parameter in the previous statement line is REGION, which accepts only integer numbers as input, and the Logical parameters are P.TYPE and UNIFORM. When logical parameters are present on

the line, their values are set to true. Otherwise, they use the default values (usually false). CONCENTRATION is a Real parameter that accepts floating-point numbers as input. Finally, the OUTFILE is a Character parameter type that accepts strings as input. A backslash (\) at the end of the line continues the code on the following line. The default value of statement parameters can be found in the Silvaco Atlas manual.

3.3.1 Structure Specification

The process of specifying the structure in Silvaco Atlas involves defining the mesh, regions, electrodes, and doping levels.

a) Mesh

For this thesis, a two-dimensional mesh is utilized, where only the x and y parameters are defined. The mesh consists of a series of horizontal and vertical lines with defined spacing between them, as shown in **Figure 3.3**. The mesh statements are specified in the following format:

```
X.MESH LOCATION = <Value> SPACING = <Value>  
Y.MESH LOCATION = <Value> SPACING = <Value>
```

As shown in the figure, y.mesh starts at $0.510\mu\text{m}$ and has a spacing of $0.001\mu\text{m}$, this indicates a relatively coarse mesh. However, the mesh becomes finer between 0.525 and $0.535\mu\text{m}$ with a spacing of $0.0001\mu\text{m}$. The x.mesh follows a uniform pattern, with a spacing of $0.1\mu\text{m}$ for the entire range. The choice of a coarse or fine mesh has an impact on the accuracy of the simulation. A coarse mesh leads to faster simulations but produces less accurate results, while a fine mesh leads to slower simulations but produces more accurate results. The areas of the structure that have a steep change in physical parameters should be of finer mesh than others and are of particular interest in the simulation. As shown in **Figure 3.3**, the mesh is finer between $y = 0.525$ and $y = 0.535\mu\text{m}$ where the interface between the electron transport layer and the absorber layer.

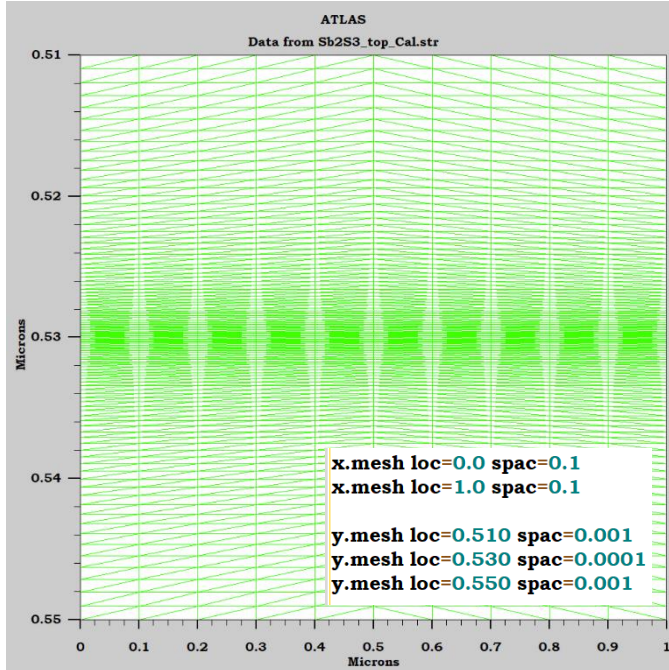


Figure 3.3 Example for an Atlas mesh.

b) Region

Once the mesh is defined, the regions of the structure must be specified. The format to define regions is as follows:

```
REGION NUMBER = <Integer> NAME = <Region_Name> \
          <Material_Type>      <Position_Parameters>
```

An example for the code that defines the regions can be identified from **Figure 3.4**, where four regions are defined with explicit limits along the x - and y -axes. In addition, each region must then be assigned a material where the code specifies the material for each region. It is important to note that the color coding is used to identify the material assigned to each region, and the boundaries of the regions are marked by vertical and horizontal lines.

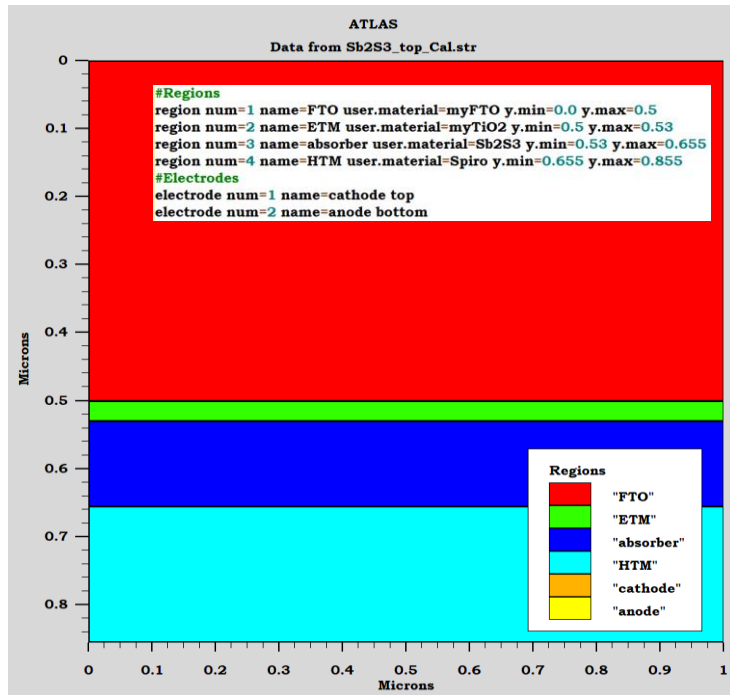


Figure 3.4 Atlas regions with materials and electrodes defined.

c) *Electrodes*

The next step in the structure specification involves defining electrodes. Usually, in this simulation, only the anode and cathode electrodes are defined. However, Silvaco Atlas allows for up to 50 electrodes to be defined. The format to define electrodes is as follows:

ELECTRODE NAME=<Electrode_Name> <Position_Parameters>

An example of an electrode statement for the anode and cathode is shown in **Figure 3.4**. The cathode is defined at the top of the cell for the entire x -range at $y = 0$. Meanwhile, the anode is defined at the bottom of the cell for the entire x -range at $y = 0.855\mu\text{m}$.

d) Doping

The final aspect of structure specification involves defining the doping levels in the structure. The format of the Atlas statement used to define doping is as follows:

```
DOPING <Dopant_Type> <Distribution_Type> <Position_Parameters>
```

Figure 3.5 specifies the doping types and levels for the structure. Doping can either be *n*-type or *p*-type, and the distribution type can be uniform or Gaussian.

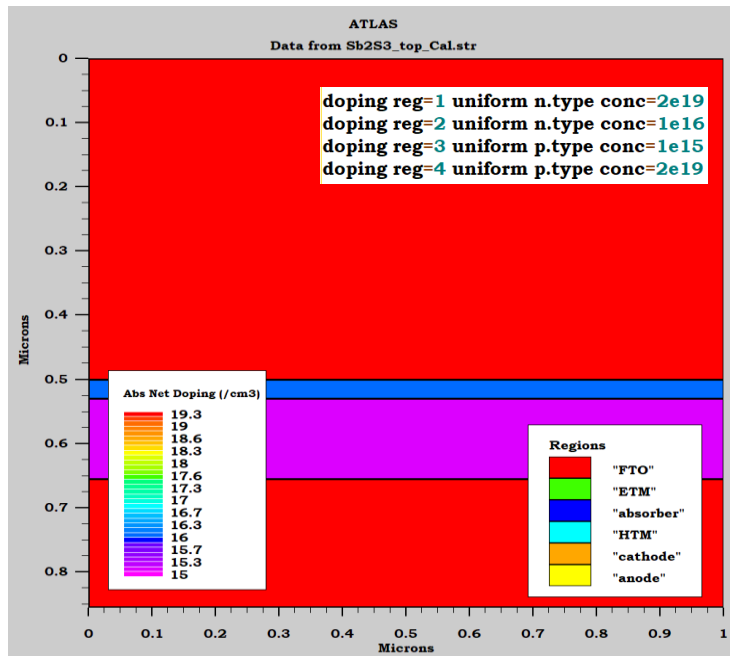


Figure 3.5 Atlas doping.

3.3.2 Materials Model Specification

The next step after structure specification is the materials model specification. It was shown in **Figure 3.2** that the materials model specification is divided into four categories: material, models, contact, and interface.

a) Material

The code for the material statement in Atlas is as follows:

```
MATERIAL <Localization> <Material_Definition>
```

Here are three examples of the material statement in Atlas:

1. MATERIAL Material = Sb2S3 EG300 = 1.7 Affinity = 3.7
2. MATERIAL Region = 3 NC300 = 3e19 NV300 = 7e19
3. MATERIAL Name = absorber MUN = 0.8 MUP = 0.2

In all of the given examples, the first appearance of the keyword "MATERIAL" is considered as a statement, whereas in the first example, the second occurrence of "Material" is regarded as a localization parameter, whereas in the second and third examples, "Region" and "Name" are the localization parameters, respectively. Apart from these parameters, the material statement can also contain other parameters, such as carrier mobility (MUN & MUP), carrier recombination lifetime (TAUN0 & TAUP0), band density of states at room temperature (NC300 & NV300), and band gap at room temperature (EG300), among others.

b) Models

There are different categories of physical models, which include mobility, recombination, carrier statistics, impact ionization, and tunneling. The format for the model statement is as follows:

```
MODELS <Model_Flag> <General_Parameter> \  
      <Model_Dependent_Parameters>
```

The selection of a model to use depends on the materials specified for simulation. An example of activating several models is shown below:

```
MODELS SRH AUGER FERMI CONMOB
```

Here, the Shockley-Read-Hall model is called SRH, while the Auger recombination model is called AUGER. Meanwhile, the Fermi-Dirac statistics

and the concentration-dependent mobility are referred to as Fermi and CONMOB, respectively.

c) Contact

The contact statement is used to specify the attributes of the electrode, such as work function and contact resistance. The code for the contact statement is as follows:

```
CONTACT NAME = <Electrode_Name> <Electrode_Parameters>
```

Below is an example of the contact statement:

```
CONTACT NAME = Cathode Workf = 4 Surf.Rec \
          VSURFN = 1e7 VSURFP = 1e6 Con.Resist = 10
```

Here, "Workf" and "Con.Resist" are the work function and the distributed resistance of the cathode electrode in units of eV and $\Omega\text{-cm}^2$, respectively. The "Surf.Rec" parameter activates its surface recombination velocity, while "VSURFN" and "VSURFP" specify the electron and hole surface recombination velocities in units of cm/s, respectively.

d) Interface

The interface statement is used to determine the boundaries between the semiconductor or insulator regions. The format of the interface statement is:

```
INTERFACE <Interface_Parameters>
```

The usage of the interface statement is demonstrated in the following example:

```
INTERFACE S.S X.Min = 0 X.Max = 1 Y.Min = 0.525 \
          Y.Max = 0.535 S.N = 1E5 S.P = 1E5
```

To clarify, the "Max" and "Min" values in the interface statement refer to the position of the interface. The "S.S" parameter denotes the interface between two semiconductor materials, while "S.N" and "S.P" specify the electron and hole surface recombination velocities in units of cm/s at the interface, respectively.

3.3.3 Numerical Method

After specifying the materials model, the next step is to select the numerical method used to solve the semiconductor device problem. The method statement is used for this purpose, as shown in **Figure 3.2**. Silvaco Atlas offers various numerical methods for solving semiconductor device problems, including the finite difference method, the finite volume method, and the Monte Carlo method. Silvaco Atlas uses three types of solution techniques to calculate solutions to semiconductor device problems:

1. decoupled (GUMMEL)
2. fully coupled (NEWTON)
3. BLOCK

The GUMMEL method is employed to solve for each unknown while keeping all other unknowns constant, and this process is repeated until there is a stable solution. The NEWTON method, on the other hand, solves all unknowns simultaneously, while the BLOCK method solves some equations with the GUMMEL method and others with the NEWTON method. The GUMMEL method is utilized for a system of equations that are weakly coupled and have linear convergence, while the NEWTON method is used when the equations are strongly coupled and have quadratic convergence. An example of the method statement is presented below:

```
METHOD GUMMEL NEWTON
```

The example demonstrates that the equations are first solved using the GUMMEL method. In the case where convergence is not achieved with the GUMMEL method, the NEWTON method is used for solving the equations.

3.3.4 Solution Specification

After choosing the numerical method, the solution specification follows. This specification involves the log, solve, load, and save statements.

a) Log

The LOG statement is used to save all terminal characteristics to a file. Any DC, transient, or AC data generated by a SOLVE statement that follows a LOG statement will also be saved. Below is an example of a LOG statement:

```
LOG  OUTFILE = Cell_IV.log
```

The current-voltage information is saved into Cell_IV.log in the previous example.

b) Solve

The SOLVE statement is used to perform a solution for one or more bias points and follows the LOG statement. Here is an example of the SOLVE statement:

```
SOLVE  B1= 1  VANODE = 0  NAME = Anode  \  
        VSTEP= 0.02  VFINAL =0.64
```

Here, B1 represents the optical spot power for the optical beam 1, where the beam number is an integer from 1 to 10. NAME denotes the electrode to which the bias voltage is applied. VANODE indicates an initial bias voltage. VSTEP represents the incremental step of the bias voltage. VFINAL denotes the final bias voltage.

c) Load and Save

The LOAD statement is used to input solutions from previous simulations as initial guesses for other bias points. On the other hand, the SAVE statement is used to output all node point information into a file. Below are examples of the LOAD and SAVE statements:

```
SAVE  OUTFILE = Top_Cell.str
```

This example demonstrates how to use the LOAD statement to load a previously saved solution. The solution is saved in the Top_Cell.str file after a SOLVE statement in one simulation, and then loaded in a different simulation using the LOAD statement as shown below:

```
LOAD INFILE = Top_Cell.str
```

3.3.5 Results Analysis

The final command group is the results analysis, which employs the EXTRACT and TONYPLOT statements, as illustrated in **Figure 3.2**. The EXTRACT statement is used to extract device parameters from a solution, while TONYPLOT is a graphical tool used to display the results. In the following examples, the J - V characteristics and EQE curves of a solar cell are extracted using the EXTRACT statement and saved into the JV_Sb2S3.dat and EQE_Cal.dat files, respectively. These files are then plotted using TONYPLOT to display the results graphically.

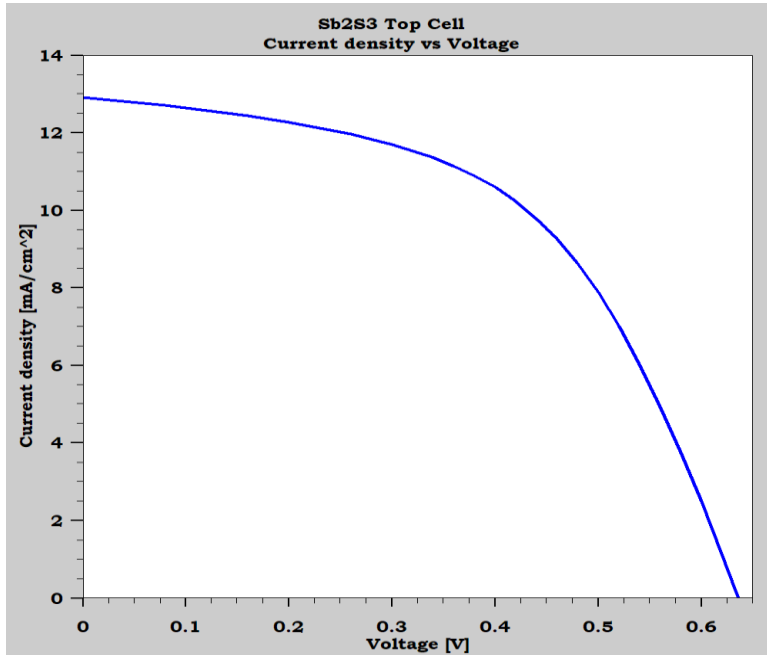
The syntax for the J - V curve of the Sb_2S_3 top cell is:

```
EXTRACT NAME = "JV" Curve(v."anode", i."cathode"*1e11) \
OUTFILE = "JV_Sb2S3.dat"
TONYPLOT JV_Sb2S3.dat
```

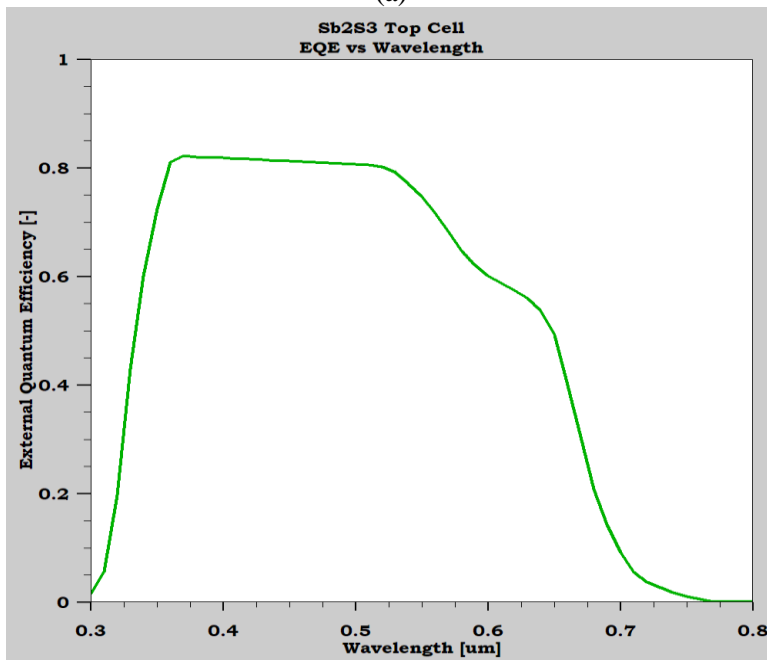
The syntax for the EQE curve of the Sb_2S_3 top cell is:

```
EXTRACT NAME = "EQE" Curve(elect."optical wavelength",
(i."cathode")/elect."source photo current") OUTFILE="EQE_Sb2S3.dat"
TONYPLOT EQE_Sb2S3.dat
```

Figure 3.6 and **3.7** present TONYPLOT samples for J - V characteristics and EQE curves of a Sb_2S_3 cell as well as the recombination rate through the absorber layer.



(a)



(b)

Figure 3.6 TONYPLOT samples: (a) J - V , and (b) EQE curves.

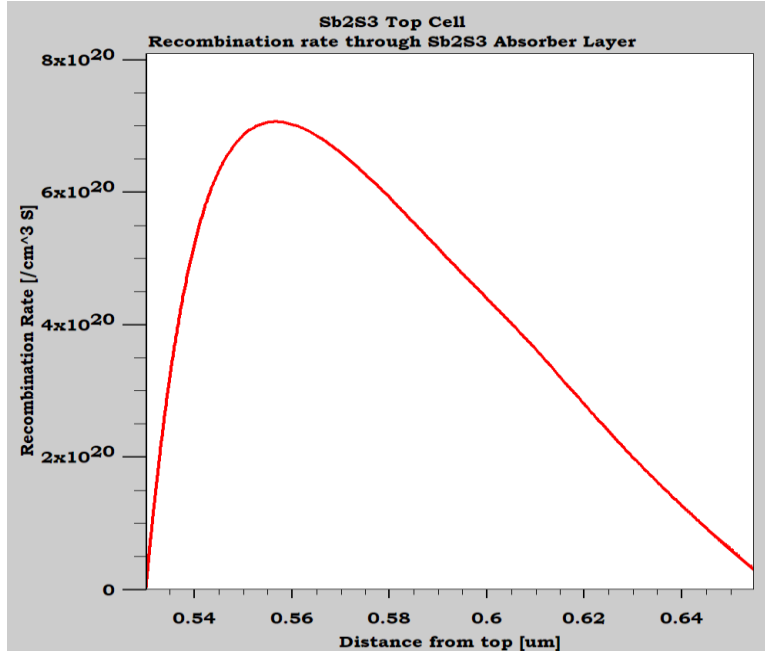


Figure 3.7 TONYPLOT sample: Recombination rate through an absorber layer.

3.4 Simulation of Tandem Cells

In a 2T monolithic tandem cell, the two sub-cells are interconnected using a tunnel junction [65–67] or thin interlayers of Silver (Ag) or Gold (Au) [68]. Additionally, an indium oxide (InO) interlayer, which has been experimentally verified to be efficient for both optical and electrical behavior, can be used as an interlayer [69]. As previously stated, the practical design of the tunnel junction is crucial in order to retain optimum functionality and hence improve tandem performance. Recently, a simple and straight forward method is utilized to model the interlayer between the sub-cells of the 2T tandem cell [58,70]. This method is to add an electrode that exactly overlays the interlayer and attach a lumped resistance to it using the following contact statement.

```
CONTACT NAME = Interlayer Resist = 1E16
```

Here, the statement specifies a lumped resistance of $1 \times 10^{16} \Omega$. Note that in 2D Atlas simulations, this passive element value is scaled by the width in the third dimension (z -direction). Since in 2D ATLAS assumes a $1 \mu\text{m}$ width, the resistance becomes $1 \times 10^{16} \Omega\text{-}\mu\text{m}$. This is totally different from the distributed contact resistance (Con.resist) described in **subsection 3.3.2**. In doing this, the tandem current is forced to transport from Anode to Cathode and prevent any current to flow in the added electrode. Physically, it is justified by the fact that the added common electrode is acting like a resistor letting current flows without significant limitation [71] and hence can be correlated with tunnel junction. The value of the resistance can be used to adjust the amount of current allowing to flow through the added electrode thus controlling the interlayer resistance. In this work, we utilize a 10 nm interlayer of ITO material as a common electrode allowing effective current transports across the tandem sub-cells [70]. Appropriate lumped resistance ($10^{16} \Omega$) is added to the common electrode.

Regarding the optics part, first, the optical intensity profiles inside the solar cell are estimated using an illuminated input source which is AM1.5G. Then, photogeneration rates are calculated given the intensity. After that, the photogeneration rates are coupled into the continuity equations' generation terms. There are two models that are used concurrently at each bias in optoelectronic device simulation, namely the optical ray tracing and photogeneration models. Regarding the first model, the optical intensity is evaluated based on the real refractive index, while for the photogeneration model, the extinction coefficient is used to compute the carrier density [72,73]. The generation at a given point is computed by evaluating the integral of the generation rate, which is given by the equation [64]:

$$G = \eta_o \frac{P\lambda}{hc} \alpha \exp(-\alpha y) \quad (3.1)$$

where η_o is the internal quantum efficiency, P is the ray intensity, y is the relative distance for the incident ray from the cell surface, h is Planck's constant, λ is the wavelength, c is the speed of light, and α is the absorption coefficient, which is given by the equation:

$$\alpha = \frac{4\pi}{\lambda} k \quad (3.2)$$

where k is the extinction coefficient.

3.5 Summary

This chapter has provided an overview of Silvaco Atlas software which is a powerful tool for simulating semiconductor devices, including single and multi-junction solar cells. Its input file structure and various statements allow for the specification of device geometry, materials properties, numerical methods, and solution parameters. The software can generate solutions for one or more bias points and save the results to files for further analysis and visualization. When it comes to simulating tandem solar cells, Silvaco Atlas can handle the complex device structures and materials required for these types of devices. By simulating the individual sub-cells and their electrical connections, the software can predict the overall performance of the tandem cell, including the efficiency and current-voltage characteristics. Overall, using Silvaco TCAD in simulating solar cells and tandem solar cells allows for a deeper understanding of the physical processes that govern device operation, and provides a valuable tool for optimizing device performance and exploring new design concepts.

CHAPTER 4
BARIUM DI-SILICIDE
TANDEM CELL

This page is intentionally left blank

CHAPTER 4

BARIUM DI-SILICIDE TANDEM CELL

4.1 Introduction

Barium di-silicide (BaSi_2) material has attracted noteworthy interest in photovoltaics, thanks to its stability, abundant nature, and excellent production feasibility. In addition, it has a high absorption coefficient (α), high minority-carrier lifetime, and suitable bandgap for use as a single junction or in tandem cells. To increase the viability of BaSi_2 to be used in tandem cells, bandgap engineering should be performed to increase E_g from its initial value of 1.3 eV. By substituting part of Ba with Sr atoms to create $\text{Ba}_{1-x}\text{Sr}_x\text{Si}_2$, E_g of the compound can be adjusted to 1.4 eV [42]. In the meantime, when replacing some Si atoms with isoelectric C, the corresponding bandgap of $\text{Ba}(\text{C}_x\text{Si}_{1-x})_2$ can steadily increase from 1.3 to 3 eV [43]. Lately, BaSi_2 -based TSCs have been demonstrated in association with perovskite and crystalline silicon [57,58].

This chapter proposes a 2T monolithic all- BaSi_2 tandem cell composed of a BaSi_2 bottom sub-cell with a 1.3 eV bandgap and a $\text{Ba}(\text{C}_x\text{Si}_{1-x})_2$ top sub-cell with a tunable bandgap. First, our simulation was calibrated against an experimental BaSi_2/Si heterojunction cell. Then, we investigate the effect of the top cell bandgap on the tandem performance, showing that the best performance is attained at a 1.8 eV bandgap ($x = 0.78$). Further, the performance of $\text{Ba}(\text{C}_{0.78}\text{Si}_{0.22})_2/\text{BaSi}_2$ TSC is optimized through various steps including the effect of doping and the thickness of the absorber layers. Additionally, the current matching point is monitored whilst altering the thickness of the top cell. Finally, the impact of changing the absorber defect density of both cells and the work function of both contacts on the tandem performance is also discussed to highlight the possible routes for boosting tandem efficiency.

4.2 Simulator Validation and Sub-Cells Structure

4.2.1 Validation of Silvaco Atlas Simulator

The simulation study is performed using the Silvaco Atlas simulation package which is a physics based 2- and 3-dimensional device simulator. The utilized physical models are included as follows. SRH recombination, the primary recombination mechanism in BaSi₂ [74], and Fermi-Dirac statistics have been considered. Carriers' mobility and lifetime values within cell layers have been taken according to available experimental values [75,76]. In addition, Auger recombination (AUGER), optical recombination (OPTR), and concentration-dependent low-field mobility (CONMOB) models are enabled. In a 2T TSC, the two sub-cells are interconnected using a 10 nm interlayer of ITO material as a common electrode allowing effective current transport across the tandem sub-cells [70]. Appropriate lumped resistance ($10^{16} \Omega$) is added to the common electrode to prevent the flow of current in the added electrode and to force the current to flow within the tandem cell without significant limitation.

Firstly, our simulation was calibrated against an experimental BaSi₂/Si heterojunction cell with a structure of indium-doped tin oxide (ITO)/*p*-BaSi₂/*n*-Si/Aluminum (Al) metal back contact [77]. In [77], BaSi₂/Si heterojunction cell was fabricated by forming B-doped *p*-BaSi₂ epitaxial films on Czochralski *n*-Si(111) substrate. Firstly, a 5-nm-thick BaSi₂ template layer was formed on Si substrate by reactive deposition epitaxy. Then, a B-doped *p*-BaSi₂ layer was formed through co-deposition of Ba, Si, and B on the template by molecular beam epitaxy. More details about the manufacturing and characterization steps can be found in [77]. **Figure 4.1**(a) and (b) depict the device design and energy band diagram of the BaSi₂/Si heterojunction cell. The essential parameters of cell layers derived from previously published stud-

ies are summarized in **Table 4.1** [76–78]. The work function of the ITO (transparent conducting front contact) is taken as 4.4 eV while that of the back Al metal is set to 4.28 eV. The absorption coefficients of the cell layers are derived from practical data [35,57,79]. After applying the listed parameters, the illuminated current density-voltage (J - V) curves for both experimental and simulated cells are presented in **Figure 4.1(c)**. The simulated cell achieves the following PV parameters: $J_{sc} = 35.52 \text{ mA/cm}^2$, $V_{oc} = 0.462 \text{ V}$, $FF = 59.40\%$, and $PCE = 9.74\%$. These parameters are quite close to the reported parameters, as shown in the inset of **Figure 4.1(c)**. As a result, an acceptable match between both cells is observed, implying that the simulation model employed in Silvaco Atlas software is validated.

Table 4.1 Basic parameters of the BaSi₂/Si heterojunction cell layers [76–78].

Parameters	<i>p</i> -BaSi ₂	<i>n</i> -Si
t (μm)	0.020	500
E_g (eV)	1.3	1.12
χ (eV)	3.2	4.05
ϵ_r	14	11.7
μ_n (cm^2/Vs)	500	1000
μ_p (cm^2/Vs)	30	500
N_c (cm^{-3})	2.6×10^{19}	2.8×10^{19}
N_v (cm^{-3})	2.0×10^{19}	1.0×10^{19}
N_D (cm^{-3})	-	2.0×10^{15}
N_A (cm^{-3})	2.0×10^{18}	-

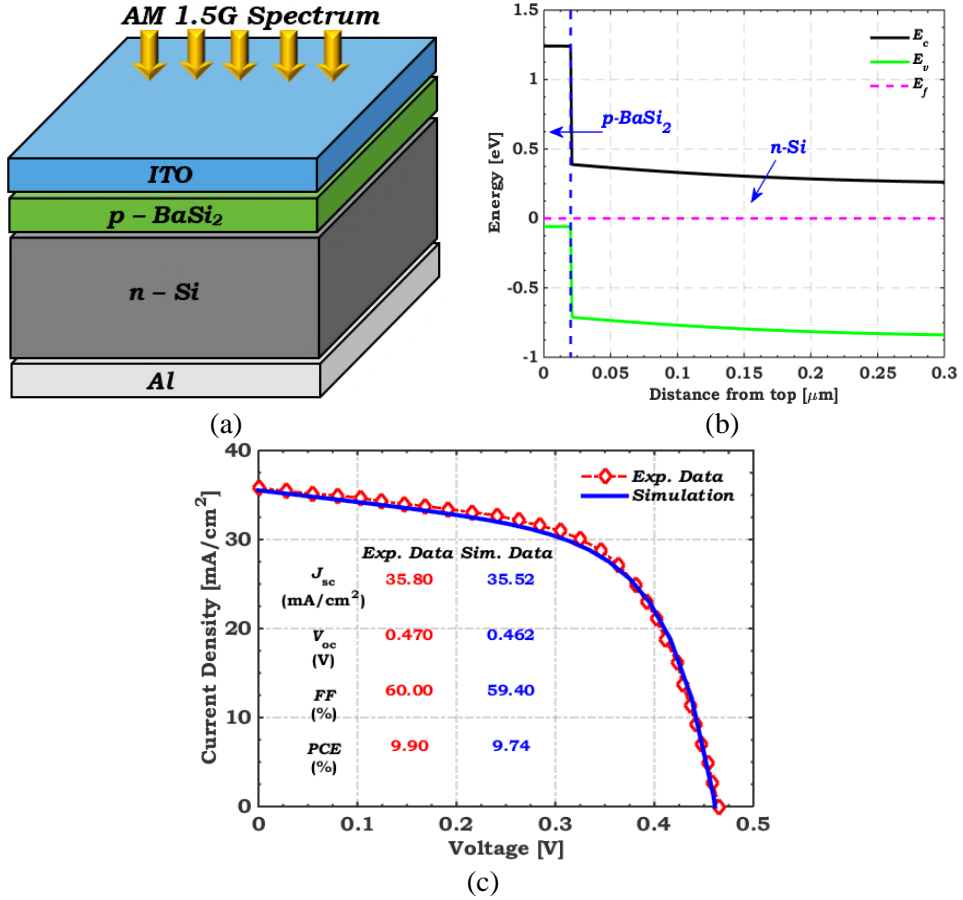


Figure 4.1 (a) Basic layers structure and (b) Energy band diagram after contact at the dark condition of the p -BaSi₂/ n -Si heterojunction solar cell. (c) Comparison of the simulated J - V characteristics with the measured data [77] under AM 1.5 illumination condition.

4.2.2 Structures of Individual Sub-Cells

A homojunction solar cell with the n^+pp^+ architecture is introduced based on the practical structure of a BaSi₂ cell [80]. **Figure 4.2** depicts the device design and energy band diagrams of the two sub-cells, containing an n^+pp^+ -BaSi₂ bottom cell and an n^+pp^+ -Ba(C_xSi_{1-x})₂ top cell. To create a homojunction solar cell, heavily doped n^+ - and p^+ - layers were positioned on opposite sides of a lightly doped p -absorber layer to extract photoexcited electron-hole pairs. The thickness of these added layers are maintained at 20 nm, which was

found experimentally to be the minimum thickness required to cover the entire surface adequately [77].

Table 4.2 summarizes the primary required parameters of the sub-cells layers used to design the tandem solar cell [58,77,78]. To model the optical properties, the refractive index n' and extinction coefficient κ as functions of a wavelength of barium di-silicide were extracted from experimental data [35,57,58], where κ was calculated from the relationship $\kappa = \alpha\lambda/4\pi$.

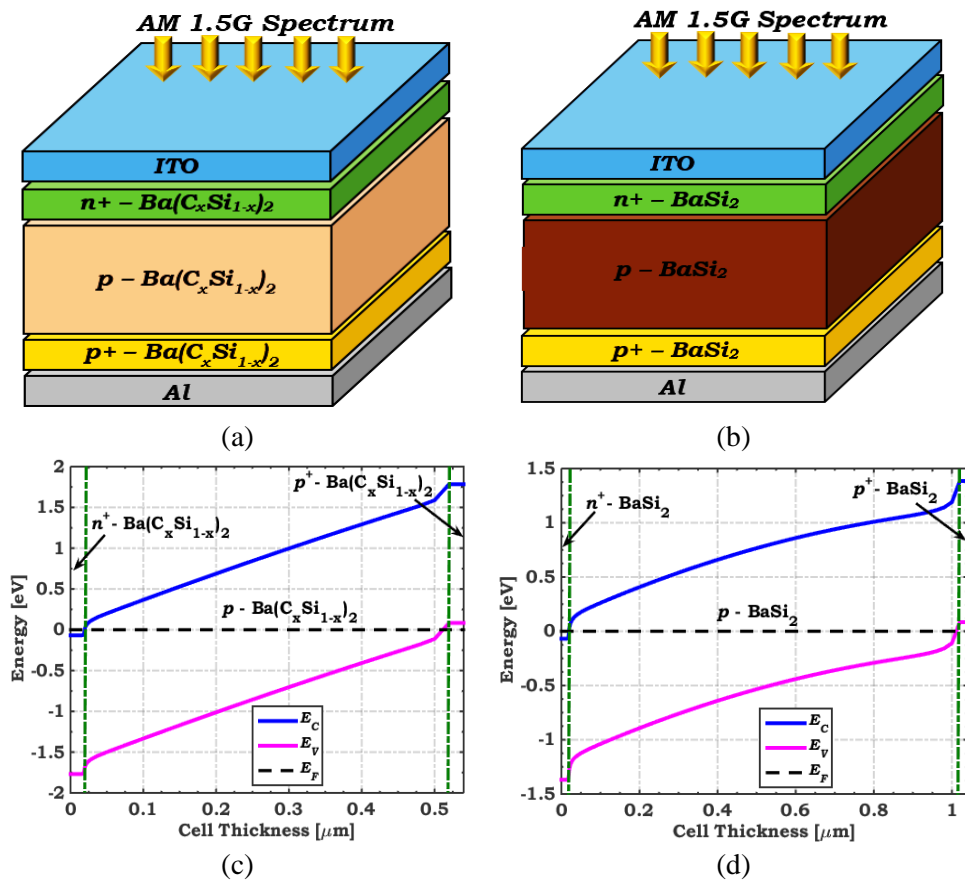


Figure 4.2 The main configuration of (a) $\text{Ba}(\text{C}_x\text{Si}_{1-x})_2$ top cell, and (b) BaSi_2 bottom cell. The energy band diagram after contact at the dark condition of (c) $\text{Ba}(\text{C}_x\text{Si}_{1-x})_2$ top cell, and (d) BaSi_2 bottom cell.

Table 4.2 Primary parameters of the sub-cells' layers used for the design of $\text{Ba}(\text{C}_x\text{Si}_{1-x})_2/\text{BaSi}_2$ tandem solar cell [58,77,78].

Parameters	Top Cell ($\text{Ba}(\text{C}_x\text{Si}_{1-x})_2$)			Bottom Cell (BaSi_2)		
	n^+	p	p^+	n^+	p	p^+
t (μm)	0.02	0.5	0.02	0.02	1	0.02
E_g (eV)	variable	variable	variable	1.3	1.3	1.3
χ (eV)	3.2	3.2	3.2	3.2	3.2	3.2
ϵ_r	14	14	14	14	14	14
μ_n (cm^2/Vs)	500	850	600	500	850	600
μ_p (cm^2/Vs)	20	100	30	20	100	30
N_c (cm^{-3})	2.6×10^{19}	2.6×10^{19}	2.6×10^{19}	2.6×10^{19}	2.6×10^{19}	2.6×10^{19}
N_v (cm^{-3})	2.0×10^{19}	2.0×10^{19}	2.0×10^{19}	2.0×10^{19}	2.0×10^{19}	2.0×10^{19}
N_D (cm^{-3})	1.0×10^{20}	-	-	1.0×10^{20}	-	-
N_A (cm^{-3})	-	1.0×10^{15}	1.0×10^{20}	-	1.0×10^{15}	1.0×10^{20}

4.3 All Barium Di-Silicide Tandem Configuration

4.3.1 Proposed Tandem Cell

In this subsection, the suggested structure of the tandem cell design ($\text{Ba}(\text{C}_x\text{Si}_{1-x})_2/\text{BaSi}_2$) is displayed in **Figure 4.3**. As mentioned before, in a 2T monolithic tandem cell, the two sub-cells are interconnected using a 10 nm interlayer of ITO material as a common electrode that is modeled by a lumped resistance. This layer has to be transparent, and it should not absorb any part of the input radiation spectrum reaching the bottom cell. Furthermore, the tandem cell current is controlled by the smaller current transporting through either the top or the bottom sub-cell. Once stacking the two sub-cells, the current matching condition should be maintained to minimize the current loss.

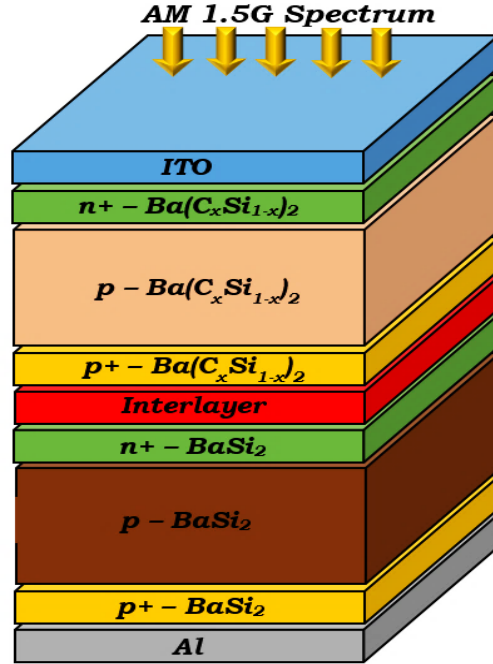


Figure 4.3 Schematic representation of a $\text{Ba}(\text{C}_x\text{Si}_{1-x})_2/\text{BaSi}_2$ tandem cell comprising of an n^+pp^+ - $\text{Ba}(\text{C}_x\text{Si}_{1-x})_2$ top sub-cell and an n^+pp^+ - BaSi_2 bottom sub-cell.

4.3.2 Tandem Cell with Variable-bandgap Top Cell

In this subsection, we investigate the effect of the top cell bandgap on the tandem performance where the compound $\text{Ba}(\text{C}_x\text{Si}_{1-x})_2$ as a top absorber is adopted. The variation of the top cell absorber bandgap depends on the composition (x) [43]. Here, the $\text{Ba}(\text{C}_x\text{Si}_{1-x})_2$ top cell bandgap is varied from 1.6 to 1.9 eV, which corresponds to x from 0.73 to 0.80. So, the $\text{Ba}(\text{C}_x\text{Si}_{1-x})_2/\text{BaSi}_2$ tandem cells are simulated using Atlas device simulator under 1-sun of AM1.5G spectrum to evaluate its performance parameters. The absorber thickness of the top cell was set to 500 nm, while the bottom BaSi_2 was fixed at 1 μm . **Figure 4.4** (a) and (b) depict a comparison between the illuminated J - V and EQE curves concerning the $\text{Ba}(\text{C}_x\text{Si}_{1-x})_2/\text{BaSi}_2$ tandem cells. The corresponding performance metrics are listed in **Table 4.3**. The results show that the best performance is obtained with a $\text{Ba}(\text{C}_{0.78}\text{Si}_{0.22})_2$ cell with a 1.8 eV

bandgap. These complementary bandgap values agree with those reported in [81] to achieve the maximum theoretical PCE. In the coming simulations, this value will be used for further optimization of the TSC under investigation.

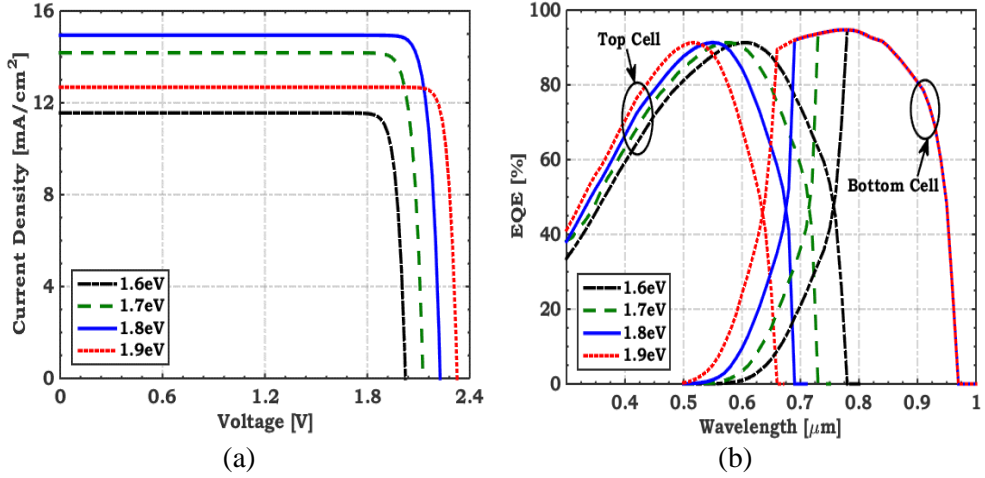


Figure 4.4 (a) Illuminated J - V , and (b) EQE curves of a $Ba(C_xSi_{1-x})_2/BaSi_2$ tandem cell.

Table 4.3 A comparison between the performance metrics for $Ba(C_xSi_{1-x})_2/BaSi_2$ tandem cells.

$Ba(C_xSi_{1-x})_2$ Top Cell		J_{sc} (mA/cm ²)	V_{oc} (V)	FF (%)	PCE (%)
x	E_g (eV)				
0.73	1.6	11.56	2.02	90.71	21.21
0.76	1.7	14.18	2.13	90.08	27.14
0.78	1.8	14.94	2.23	90.20	30
0.80	1.9	12.68	2.33	92	27.13

4.4 Tandem Cell Optimization

This section presents the optimization steps for a 2T monolithic $Ba(C_xSi_{1-x})_2/BaSi_2$ TSC. First, the impact of the absorber layers doping on the tandem performance is studied. Then, we investigate the influence of top and bottom absorber thicknesses on TSC working metrics. Furthermore, we inspect the current matching point to get the maximum available PCE. The effect of top and bottom absorber defect densities on TSC working metrics is then

investigated. Finally, we study the impact of front and rear contact work functions on the TSC performance.

4.4.1 The Effect of Absorber Layer Doping

The absorber layer doping is crucial in regulating bulk recombination. Its role in controlling the fill factor is also significant as increasing the doping level results in decreasing the series resistance which, in turn, increases the fill factor. However, increasing the doping level beyond a certain value may trigger some other undesirable effects like band gap narrowing and mobility degradation that causes an overall decline in performance. Herein, a parametric analysis study is done by changing the absorber layers doping from 1×10^{15} to $1 \times 10^{19} \text{ cm}^{-3}$ to investigate its impact on the tandem performance. **Figure 4.5** (a) and (b) demonstrate that the PCE attains its maximum value when the doping density is $1 \times 10^{17} \text{ cm}^{-3}$ for both cells. The electric field in a depletion region is responsible for separating photogenerated carriers and, in addition, depends on the carrier's doping on both junction sides. Increasing absorber doping increases the electric field in the depletion region for both sub-cells and, consequently, improves their conversion efficiency.

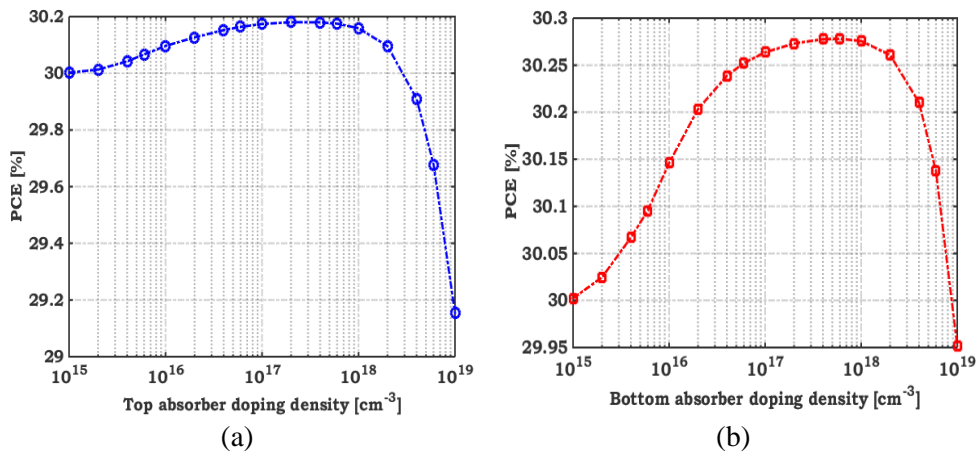


Figure 4.5 Impact of absorber layer doping on PCE of (a) $\text{Ba}(\text{C}_{0.78}\text{Si}_{0.22})_2$ top cell, and (b) BaSi_2 bottom cell.

4.4.2 The Effect of Absorber Layer Thickness

Figure 4.6 signifies the dependency of the tandem efficiency on the thickness of both absorber layers. To investigate device performance, the thickness top absorber (t_{TA}) was increased from 0.5 up to 1.5 μm and that of the bottom absorber (t_{BA}) was increased from 1 to 4 μm while the other parameters remain fixed. It can be depicted from **Figure 4.6** that there is an inconsiderable effect on PCE as t_{BA} grows from 2 to 4 μm and t_{TA} raises from 0.8 to 1.5 μm . As t_{TA} falls below 0.8 μm , the efficiency gradually decreases from 32.4% to 30.4%. In addition, changing t_{BA} from 2 to 4 μm does not affect PCE while keeping t_{TA} constant below 0.75 μm . The best performance can be determined when t_{TA} and t_{BA} are chosen to be 1.1 and 3 μm , respectively.

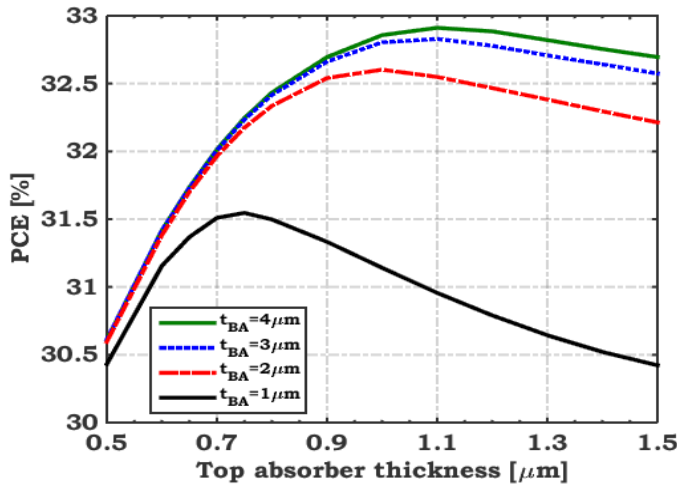


Figure 4.6 Tandem efficiency dependency on the thickness of the top and bottom absorber layers.

4.4.3 Current Matching Point

In this subsection, the absorber thickness (t_{TA}) of the top cell has been altered from 0.85 to 1.25 μm , while the bottom BaSi_2 was fixed at 3 μm . **Figure 4.7(a)** shows the J_{sc} of the top and bottom sub-cells versus the thickness of the $\text{Ba}(\text{C}_{0.78}\text{Si}_{0.22})_2$ absorber layer in the top cell, in which significant dependency on t_{TA} is shown. As t_{TA} becomes thicker, the J_{sc} of the top cell rises, and the

J_{sc} of the bottom cell, in turn, reduces. The reason is that the thicker is the top cell is, the more are the photons which can be absorbed leading to less transferred light to the bottom cell. A current matching point occurs at $J_{sc} = 16.47$ mA/cm² and is satisfied at $t_{TA} = 1.05$ μm for the absorbing film of the top cell. As displayed in **Figure 4.7(b)**, PCE of the tandem cell reaches a maximum value at the current matching point. In this condition, the performance of the Ba(C_{0.78}Si_{0.22})₂/BaSi₂ tandem cell has been simulated. The J - V characteristics of tandem, top, and bottom cells are drawn in **Figure 4.8(a)**. The maximum value of J_{sc} of the perfectly matched tandem cell is equal to 16.47 mA/cm² with $V_{oc} = 2.24$ V and PCE = 32.83%. The value of $V_{oc} = 2.24$ V is equal to the sum of those of the top cell (1.37 V) and bottom cell (0.87 V), indicating negligible drop on the recombination junction. Moreover, the EQE of both cells at the current matching condition is demonstrated in **Figure 4.8(b)**. The EQE of the bottom BaSi₂ sub-cell surpasses 95% at a wavelength around 800 nm.

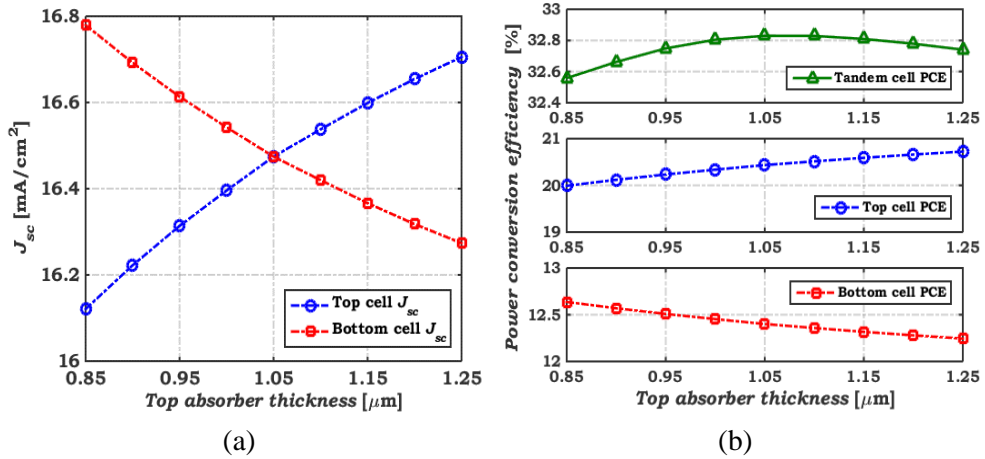


Figure 4.7 Variation of cell parameters versus top cell absorber thickness from 0.85 to 1.25 μm (a) J_{sc} of top and bottom sub-cells and (b) PCE of the bottom, top and tandem cells.

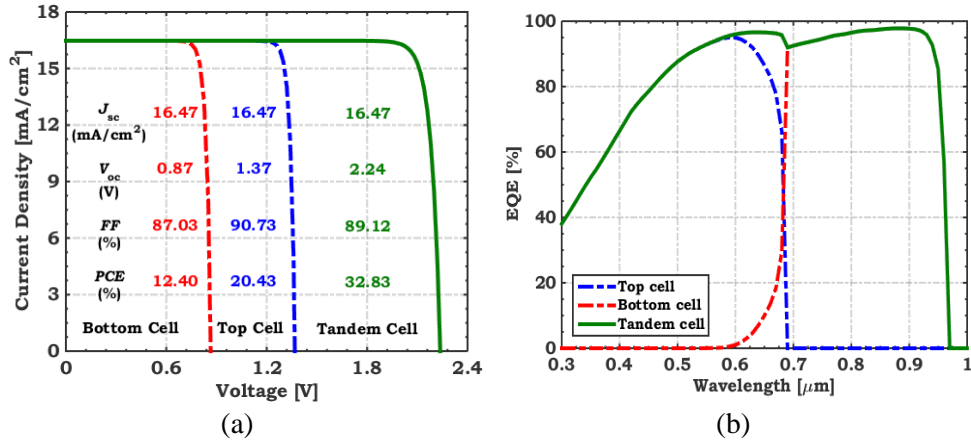


Figure 4.8 Device characteristics at the current matching point (a) J - V curves, and (b) EQE spectra of the bottom, top, and tandem cells.

4.4.4 The Defect Density of Absorber Layers

Figure 4.9 represents contour graphs of TSC performance metrics dependence on the defect concentration of both the top and bottom absorber layers. The defect density ranges from 10^{12} to 10^{18} cm⁻³ while preserving the other parameters unchanged to explore the device performance. As clear from **Figure 4.9(a)**, the J_{sc} significantly decreases as the defect density of the top and bottom absorber layers increases. For example, J_{sc} drops from 16 to 12 mA/cm² as the defect density of the bottom absorber rises from 10^{15} to 10^{18} cm⁻³, and that of the top layer grows from 10^{16} to 10^{18} cm⁻³. Besides, there is no change in J_{sc} as the defect density of the top absorber layer is below 10^{16} cm⁻³ or that of the bottom absorber layer is below 10^{15} cm⁻³.

It has been reported in the literature that V_{oc} is extremely affected by the defect concentration of the absorber layer [82]. In this context, it can be shown in **Figure 4.9(b)** that V_{oc} decreases from 2.10 to 1.55 V when the defect density of the absorber layers raises from 10^{15} to 10^{18} cm⁻³. For absorber layers defect density lower than 10^{15} cm⁻³, there is no appreciable effect on V_{oc} . **Figure 4.9(c)** shows that the FF gradually declines from 86 to 73% when the defect density of the absorber layers raises from 10^{15} to 10^{18} cm⁻³. Again, for small

values of defect density of absorber layers (below 10^{15} cm^{-3}), there is no significant effect on FF. Theoretically, FF is related to V_{oc} but in addition, it is strongly correlated to the recombination processes inside the depletion region.

Finally, as clarified in **Figure 4.9(d)**, we noticed an expected change in the profile of PCE due to its dependency on J_{sc} , V_{oc} , and FF. There is an insignificant effect on PCE as the defect density of the absorber layers is below 10^{15} cm^{-3} . PCE sharply decreases from 30 to 13% as the defect density of the absorber layers grows from 10^{15} to 10^{18} cm^{-3} .

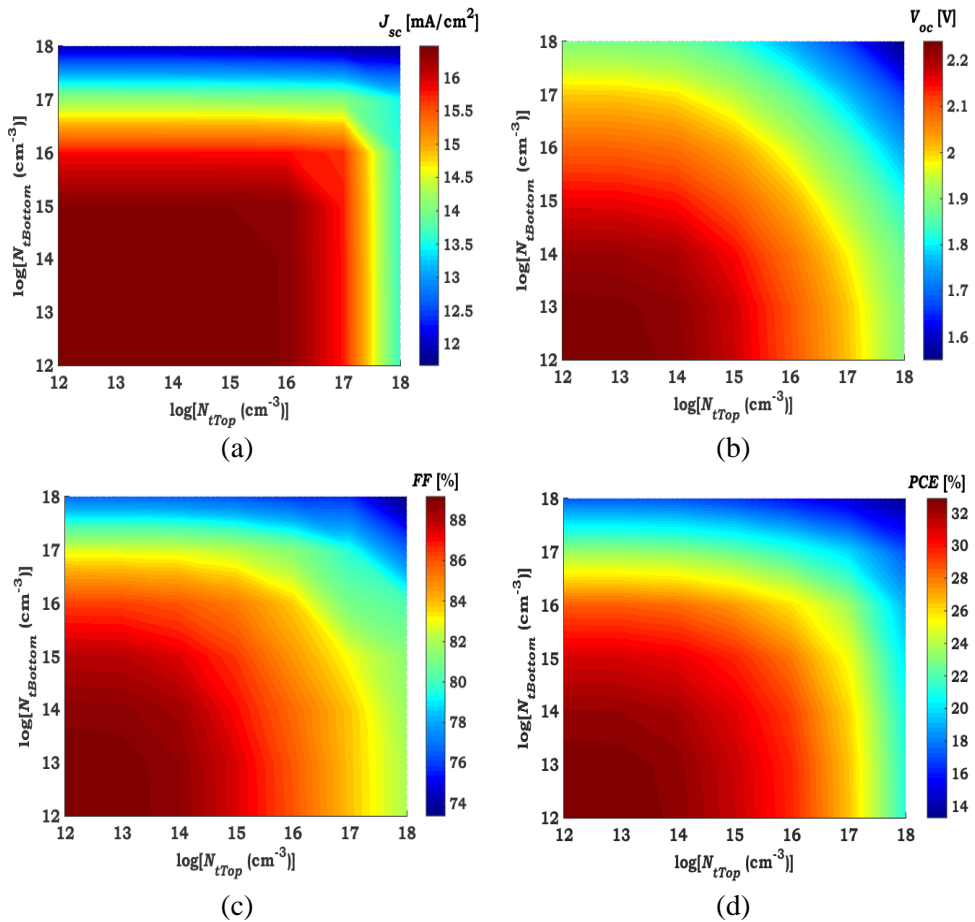


Figure 4.9 Contour graphs of TSC performance figure of merit dependency on the defect density of top and bottom absorber layers.

This significant decline in cell performance with increasing defect density is attributed to increased carrier recombination (which means lower diffusion lengths), as shown in **Figure 4.10**. The figure demonstrates the recombination rate (R) behavior for the absorber layer with various defect densities under short-circuit conditions. As expected, as trap density grows, the recombination rate climbs dramatically, indicating poor performance.

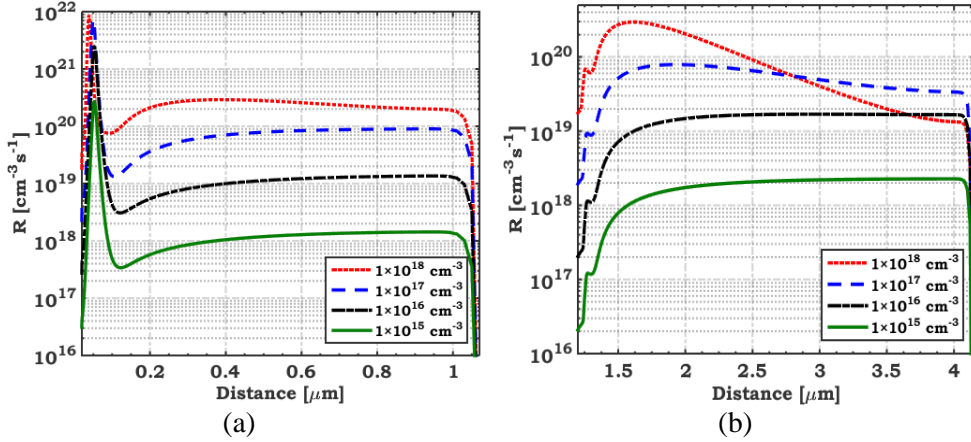


Figure 4.10 The recombination rate behavior drawn at the illuminated short-circuit condition for (a) the top absorber layer and (b) the bottom absorber layer.

4.4.5 Work Functions of The Front and Rear Contacts

Work functions of the front and rear contacts are crucial factors that affect the device's performance as they modulate the metal/semiconductor contact barrier height and therefore the transportation of charge carriers [83]. **Figure 4.11** show the energy band diagrams of the interfaces of the metal/ n^+ - semiconductor and the metal/ p^+ - semiconductor illustrating the bandgap (E_g), the electron affinity (χ), and the work function (ϕ_s) of the semiconductor material, in addition to the metal work function (ϕ_m) and the Schottky barrier (Φ_b). The front Schottky barrier at the metal/ n^+ - $\text{Ba}(\text{C}_{0.78}\text{Si}_{0.22})_2$ interface is computed using the equation [84]:

$$\phi_{b,\text{front}} = \phi_{m,\text{front}} - \chi \quad (4.1)$$

where $\varphi_{m,\text{front}}$ is the front contact work function, and χ is the electronic affinity of $\text{Ba}(\text{C}_{0.78}\text{Si}_{0.22})_2$. while the rear Schottky barrier at the metal/ p^+ - BaSi_2 interface is calculated using the equation [84]:

$$\phi_{b,\text{rear}} = \chi + E_g - \varphi_{m,\text{rear}} \quad (4.2)$$

where χ and E_g are the electronic affinity and the bandgap energy of BaSi_2 , respectively, and $\varphi_{m,\text{rear}}$ is the rear contact work function. The front contact work function is changed from 3 to 4.8 eV, while that of the rear contact materials is summarized in **Table 4.4**.

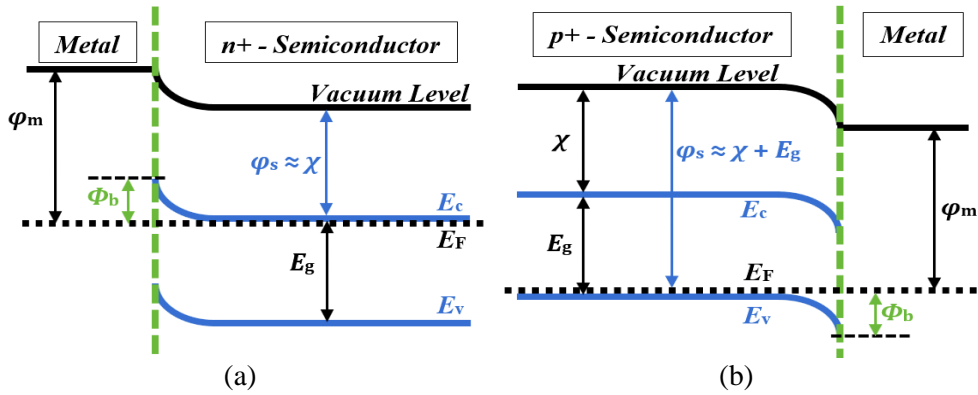


Figure 4.11 Schematic energy diagram illustrating Schottky barrier (Φ_b) at (a) the metal/ n^+ - semiconductor interface ($\varphi_m > \varphi_s$), and (b) the metal/ p^+ - semiconductor interface ($\varphi_m < \varphi_s$).

Table 4.4 Inorganic rear contact materials showing their work function values [33,83,85–87].

Material	Work function (eV)
Al (aluminum)	4.28
Mo (Molybdenum)	4.6
Ag (silver)	4.74
Fe (iron)	4.81
Nb (niobium)	4.9
Cu (copper)	5
Au (gold)	5.1
Pd (palladium)	5.3
C (carbon)	5.4
Ni (nickel)	5.5
Pt (platinum)	5.7

Figure 4.12(a) and (b) illustrate the energy band diagrams for various work function values of front and rear contacts at the short circuit and dark conditions. As apparent in **Figure 4.12(a)**, increasing $\phi_{m,\text{front}}$ results in increasing the front barrier height $\phi_{b,\text{front}}$, which leads to sufficient bending up of E_c close to metal/ n^+ -Ba(C_{0.78}Si_{0.22})₂ interface irrespective of n^+ -Ba(C_{0.78}Si_{0.22})₂ thickness. This bending impedes the transfer of photo-excited electrons to the front electrode. On the other hand, decreasing $\phi_{m,\text{front}}$ leads to a decrease of $\phi_{b,\text{front}}$, and thus, improves the device performance. Similarly, in **Figure 4.12(b)**, the rear barrier height $\phi_{b,\text{rear}}$ produces sufficient bending down of E_v adjoining to the p^+ -BaSi₂/metal interface and so the series resistance increases at the contact interface which results in impeding the transport of photoexcited holes to the back electrode. In addition, $\phi_{b,\text{rear}}$ decreases with increasing $\phi_{m,\text{rear}}$ and improves the device performance.

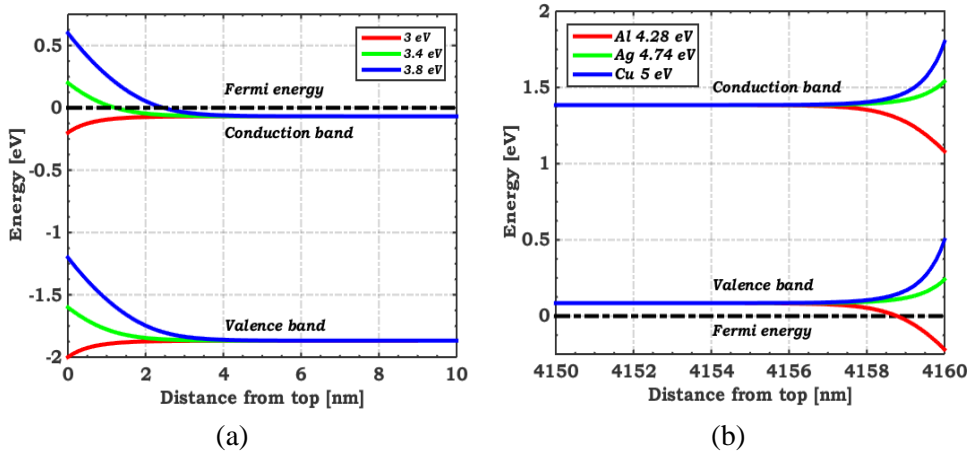


Figure 4.12 Energy band diagram at short-circuit and dark conditions of (a) the top 10 nm for different values of front contact work function, and (b) the bottom 10 nm for distinct values of rear contact work function.

Figure 4.13 exhibits contour graphs of the photovoltaic parameters of Ba(C_{0.78}Si_{0.22})₂/BaSi₂ tandem solar cells under different values of the work function for both contacts. As apparent in **Figure 4.13**, there is no effect on the performance parameters as $\phi_{m,\text{rear}}$ is larger than 4.5 eV while $\phi_{m,\text{front}}$

remains constant. On the other hand, with increasing $\varphi_{m,\text{front}}$ from 3.8 to 4.8 eV, J_{sc} and FF values gradually decrease while V_{oc} drastically drops from 2.18 to 1.18 V. Finally, as clarified in **Figure 4.13(d)**, an expected trend in PCE is observed due to its dependency on J_{sc} , V_{oc} , and FF. There is an insignificant effect on PCE when $\varphi_{m,\text{front}}$ is below 3.8 eV, and $\varphi_{m,\text{rear}}$ remains constant, while it sharply decreases from 31 to 15% as $\varphi_{m,\text{front}}$ is increased above 3.8 eV. The optimum efficiency has been attained with a terbium front contact ($\varphi_{\text{terbium}} = 3$ eV) and a silver rear contact, resulting in the following PV parameters: $J_{sc} = 16.48 \text{ mA/cm}^2$, $V_{oc} = 2.27 \text{ V}$, $FF = 91.45\%$, and $PCE = 34.25\%$.

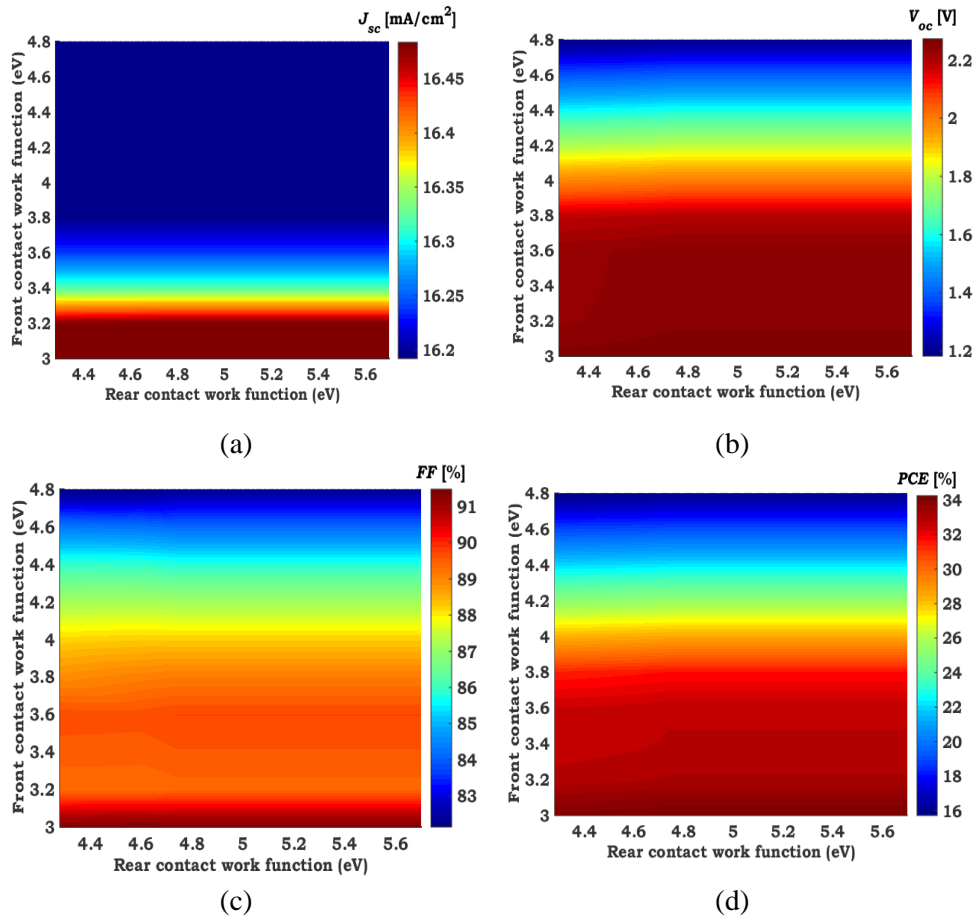


Figure 4.13 Contour graphs of tandem cell performance parameters dependence on front and rear contact work function.

4.5 Summary

This chapter presented a simulation study for a 2T monolithic all-BaSi₂ tandem cell. In the proposed design, a BaSi₂ bottom sub-cell with a bandgap of 1.3 eV, and a Ba(C_xSi_{1-x})₂ top sub-cell with a tunable bandgap were utilized. It was found that a bandgap of 1.8 eV, which corresponds to $x = 0.78$, is the optimum choice to obtain the maximum initial PCE of 30%. Then, the tandem performance was optimized by investigating the impact of doping and the thickness of both absorber layers. Further, the current matching point was monitored whilst altering the thickness of the top cell in the range (0.85 – 1.25 μm) resulting in PCE = 32.83%. Additionally, we have inspected the consequence of the absorbers defect density in the range ($10^{12} - 10^{18} \text{ cm}^{-3}$) and the impact of the work functions of the contacts on the performance parameters of the TSC. It was found that contacts having a work function ≥ 4.5 eV for rear contact and ≤ 3.8 eV for front contact guarantee good performance. These results can offer possible routes leading in the direction of the advancement of low-cost, environmentally friendly, and efficient TSCs.

CHAPTER 5
ANTIMONY SULFIDE/SILICON
TANDEM CELL

This page is intentionally left blank

CHAPTER 5

ANTIMONY SULFIDE/SILICON TANDEM CELL

5.1 Introduction

Antimony sulfide (Sb_2S_3) is one of the most appropriate top cell candidates for next-generation TSCs owing to its desired broad bandgap of 1.7 eV [44], intrinsic stability [45,46], non-toxicity, and less expensive constituent elements. As well, it has been theoretically shown that combining c-Si as a bottom sub-cell along with a top sub-cell whose material bandgap is 1.72 eV in a 2T TSC, an efficiency near 43% can be reached [47]. Consequently, Sb_2S_3 , whose bandgap is 1.7 eV, can be a proper top cell partner combined with an optimal bottom cell like silicon in TSCs. A few studies have recently investigated Sb_2S_3 as a top cell in Si-based TSCs [59–61]. Recently, a tandem cell based on Sb_2S_3 and Sb_2Se_3 as top and bottom cells, respectively, was fabricated and a PCE of 7.93% was reported which surpasses the independently top Sb_2S_3 and bottom Sb_2Se_3 cells [62]. This experimental study proves the suitability of Sb_2S_3 -based solar cell as a top cell of TSC and establishes a proof of concept.

This chapter proposes a TSC that combines Sb_2S_3 and thin film c-Si materials for the top and bottom sub-cells, respectively. Devices based on these materials are considered environmentally friendly solar cells, in addition to their low processing cost. Using all thin film layers results in flexible tandem cells that may be used in some applications like wearable electronics. Before the simulation of our proposed TSC, the two standalone sub-cells are calibrated versus experimental studies by applying the appropriate geometrical and physical parameters to validate the simulator. Next, the Sb_2S_3 top cell is optimized by designing the cell without HTL to avoid its organic issues and tuning the CBO between the ETL and the Sb_2S_3 absorber. Then, optimization

steps are carried out to design the tandem for maximum possible efficiency. The first step is to optimize the ETL thickness and doping concentration. Further, the effect of changing the absorber defect density and the series resistance of the top cell on the TSC performance is investigated. Furthermore, the impact of varying the thicknesses of the top and bottom absorbers on the TSC is also explored to highlight the potential paths for promoting tandem efficiency.

5.2 Simulator Validation and Device Structure

5.2.1 Validation of Silvaco Atlas Simulator

The simulation study was performed using the Silvaco Atlas simulator. The physical models incorporated into Atlas are selected as follows. SRH recombination is predominant in Sb_2S_3 cells because of the considerable recombination observed in Sb_2S_3 films with high defect density [88,89]. Besides, Auger recombination (AUGER) is enabled to account for recombination occurring in the regions of high doping. In addition, the Fermi-Dirac statistics (Fermi), optical recombination (OPTR), and concentration-dependent mobility (CONMOB) models are invoked. In a 2T TSC, the two sub-cells are interconnected using a 10 nm interlayer of ITO material as a common electrode allowing effective current transport across the tandem sub-cells [70]. Appropriate lumped resistance ($10^{16} \Omega$) is added to the common electrode to prevent the flow of current in the added electrode and to force the current to flow within the tandem cell without significant limitation.

The simulator was first calibrated against two experimental cells, a heterojunction Sb_2S_3 cell and a homojunction c-Si cell, as follows. A heterojunction top Sb_2S_3 cell having an $n-i-p$ structure is based on a practical configuration of a fabricated solar cell containing the same transport layer materials [90]. A lightly doped p - Sb_2S_3 film is sandwiched between lightly doped n - TiO_2 and

p⁺-Spiro-OMeTAD layers to create a heterojunction solar cell and extract photoexcited electron-hole pairs. In [90], The experimental steps of the Sb₂S₃ fabrication were performed firstly by preparing a diluted CS₂ in an ethanol precursor solution and followed by dissolving the low-cost Sb₂O₃ and Sb-source in the solution. The produced Sb₂S₃ film has a lateral grain size up to 12 μm which was achieved through spin-coating and annealing at 300 °C for 2 minutes. More details about the processing steps and conditions as well as the electrical characterization are found in [90]. **Figure 5.1**(a) and (b) depict the top cell's device design and energy band diagram, respectively. The key parameters of cell layers derived from previously published studies are summarized in **Table 5.1** [91–95]. In addition, Defect parameters in the cell layers and at the interfaces (TiO₂/Sb₂S₃ and Sb₂S₃/Spiro-OMeTAD) are presented in **Table 5.2**. The work function of the FTO (transparent conducting top contact) is set to 4 eV, whereas that of the rear Au contact is taken to be 5.1 eV. A parasitic series resistance (*R*_s) is fitted at 10 Ω cm² to match the experimental results [90]. Upon utilizing the listed parameters, the illuminated current density-voltage (*J*–*V*) along with the external quantum efficiency (*EQE*) characteristics of both simulated and experimental Sb₂S₃ cells [90] are presented in **Figure 5.1**(c) and (d), respectively. The simulated cell gives: (*J*_{sc} = 12.91 mA/cm², *V*_{oc} = 0.636 V, FF = 52.45%, and PCE = 4.31%). These PV parameters well match the reported experimental parameters, as shown in the inset of **Figure 5.1**(c), implying that the simulation model employed in Silvaco Atlas software has been validated.

Table 5.1 Basic parameters of the Sb_2S_3 and thin c-Si solar cell layers

Parameters	Top Cell				Bottom Cell		
	FTO	TiO ₂	Sb ₂ S ₃	Spiro-OMeTAD	n+ Si	p Si	p+ Si
t (μm)	0.5	0.03	0.125	0.2	0.1	20	0.2
E_g (eV)	3.5	3.2	1.7	3.17	1.12	1.12	1.12
χ (eV)	4	4.26	3.70	2.05	4.05	4.05	4.05
ϵ_r	9	9	7	3	11.7	11.7	11.7
μ_n (cm^2/Vs)	20	20	0.8	2×10^{-4}	Default values		
μ_p (cm^2/Vs)	10	10	0.2	2×10^{-4}			
N_c (cm^{-3})	2.2×10^{18}	2×10^{18}	3×10^{19}	2.2×10^{18}	2.8×10^{19}	2.8×10^{19}	2.8×10^{19}
N_v (cm^{-3})	1.8×10^{19}	1.8×10^{19}	7×10^{19}	1.8×10^{19}	1×10^{19}	1×10^{19}	1×10^{19}
N_D (cm^{-3})	2×10^{19}	1×10^{16}	-	-	1×10^{19}	-	-
N_A (cm^{-3})	-	-	1×10^{15}	2×10^{19}	-	1×10^{15}	1×10^{20}
Reference	[91]	[92]	[93,94]	[92]	[96]	[96]	[96]

Table 5.2 Defects parameters in the Sb_2S_3 solar cell layers and at the interfaces.

	Interface Defects		Bulk Defects		
	TiO ₂ /Sb ₂ S ₃	Sb ₂ S ₃ /Spiro	TiO ₂	Sb ₂ S ₃	Spiro
Defect type	Neutral	Neutral	Acceptor	Acceptor	Acceptor
Electron and hole capture cross-section	$1 \times 10^{-15} \text{ cm}^2$	$1 \times 10^{-15} \text{ cm}^2$	$1 \times 10^{-15} \text{ cm}^2$	$1 \times 10^{-15} \text{ cm}^2$	$1 \times 10^{-15} \text{ cm}^2$
Energetic distribution	Single	Single	Single	Single	Single
Energy level to the highest E_v	0.85 eV	0.85 eV	0.60 eV	0.85 eV	0.60 eV
Total density	$1 \times 10^{15} \text{ cm}^{-2}$	$1 \times 10^{15} \text{ cm}^{-2}$	$1 \times 10^{15} \text{ cm}^{-3}$	$4.1 \times 10^{16} \text{ cm}^{-3}$	$1 \times 10^{15} \text{ cm}^{-3}$

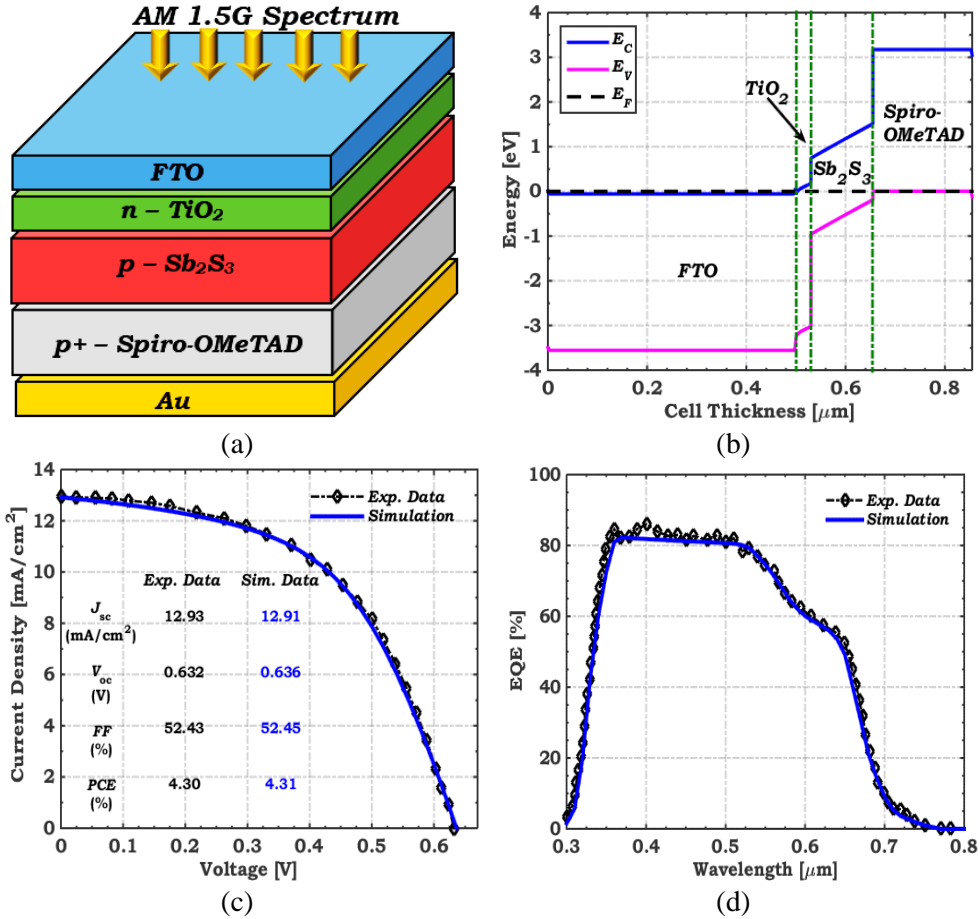


Figure 5.1 (a) Basic layers structure, and (b) Energy band diagram after contact at the dark condition of Sb₂S₃-based cell. (c) Illuminated J - V and (d) EQE curves of both simulated and experimental Sb₂S₃ cells [90].

On the other hand, a homojunction bottom c-Si cell having a n^+ - p - p^+ configuration is calibrated against the experimental thin c-Si cell, yielding the following performance parameters: ($J_{sc} = 29.60$ mA/cm², $V_{oc} = 0.617$ V, FF = 77.90%, and PCE = 14.30%) [97]. In [97], the first step in the experimental processes of the fabricated c-Si bottom cell was firstly to etch a 380 μ m Czochralski crystalline silicon wafer to produce a 20 μ m thin c-Si substrate. The emitter and back surface field (BSF) regions were then created by employing the spin-on-dopant technique. Finally, Al electrodes were defined by using a thermal evaporator. More details about the manufacturing and characterization

steps can be found in [97]. **Figure 5.2**(a) and (b) depict the cell design and energy band diagram of the n^+pp^+ -Si bottom cell. The essential parameters of cell layers are summarized in **Table 5.1** [96]. In addition, carrier mobility and carrier lifetime within cell layers are based on default values incorporated in Atlas. The illuminated J - V and EQE characteristics of both simulated and experimental c-Si cells are obtained as presented in **Figure 5.2**(c) and (d). The cell gives the following performance factors: ($J_{sc} = 29.66 \text{ mA/cm}^2$, $V_{oc} = 0.615 \text{ V}$, $FF = 78.16\%$, and $PCE = 14.26\%$), indicating an insignificant difference between our simulation results and experimental data [97] and also validating the simulation model employed in Silvaco Atlas software.

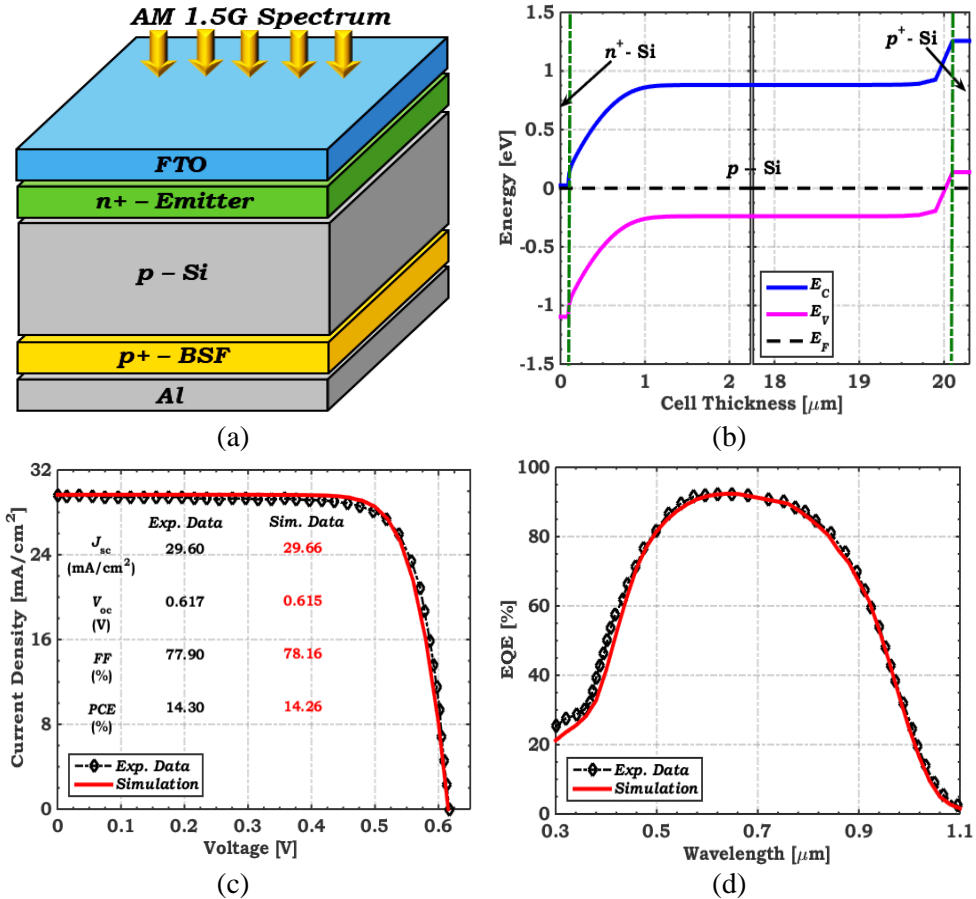


Figure 5.2 (a) Basic layers structure, and (b) Energy band profile after contact at the dark condition of a thin c-Si cell. (c) Illuminated J - V and (d) EQE curves of both simulated and experimental thin c-Si cells [97].

5.2.2 Initial Sb₂S₃/Si tandem cell

This subsection presents a 2T monolithic initial Sb₂S₃/Si tandem cell. **Figure 5.3(a)** depicts the cell's suggested structure. In a 2T monolithic tandem cell, the two sub-cells are interconnected using a 10 nm interlayer of ITO material as a common electrode that is modeled by a lumped resistance as indicated here before. Furthermore, the current flowing in a TSC is controlled by the smaller current transporting through either the front or the back sub-cell. Therefore, current matching situation must be provided to minimize the current loss. Additionally, since a broad bandgap absorber is required for the top sub-cell, as explained herein. Therefore, our design adopts an Sb₂S₃ solar cell having a bandgap of 1.7 eV as a front cell along with the thin c-Si back cell.

The initial TSC is simulated using Atlas under AM1.5G illumination, and the simulation results are displayed in **Figure 5.3(b)** and (c). The cell performance metrics are ($J_{sc} = 13.61$ mA/cm², $V_{oc} = 1.23$ V, FF = 60.55%, and PCE = 10.10%). V_{oc} of the TSC is nearly equal to the sum of V_{oc} of the individual sub-cells, while its current (13.61 mA/cm²) is limited by the current of the Sb₂S₃ top cell (12.89 mA/cm²). As shown in **Figure 5.3(b)**, The photocurrent of the Sb₂S₃ sub-cell exhibited a strong bias dependency. The different generated photocurrents in the sub-cells develop a negative bias across the sub-cell with lower photocurrent due to the excess photocurrent in the adjacent sub-cell [98,99]. This negative bias would improve the current collection efficiency and increase the photocurrent from 12.89 to 13.61 mA/cm².

As seen, there is a significant deterioration in tandem performance which is attributed to recombination losses due to bulk defects in the Sb₂S₃ absorber layer; thus, V_{oc} is reduced, which is the dominant bottleneck of high-performance antimony chalcogenide solar cells [100]. Furthermore, interface defects are typically caused by a mismatch lattice between the TiO₂ buffer layer and the Sb₂S₃ absorber layer. Thus, the recombination defects at the Sb₂S₃/TiO₂

interface [101] would demolish the photocarriers. Therefore, the Sb_2S_3 top cell has to be optimized, especially for conduction band offset (CBO), before incorporating it in a 2T monolithic $\text{Sb}_2\text{S}_3/\text{Si}$ tandem cell.

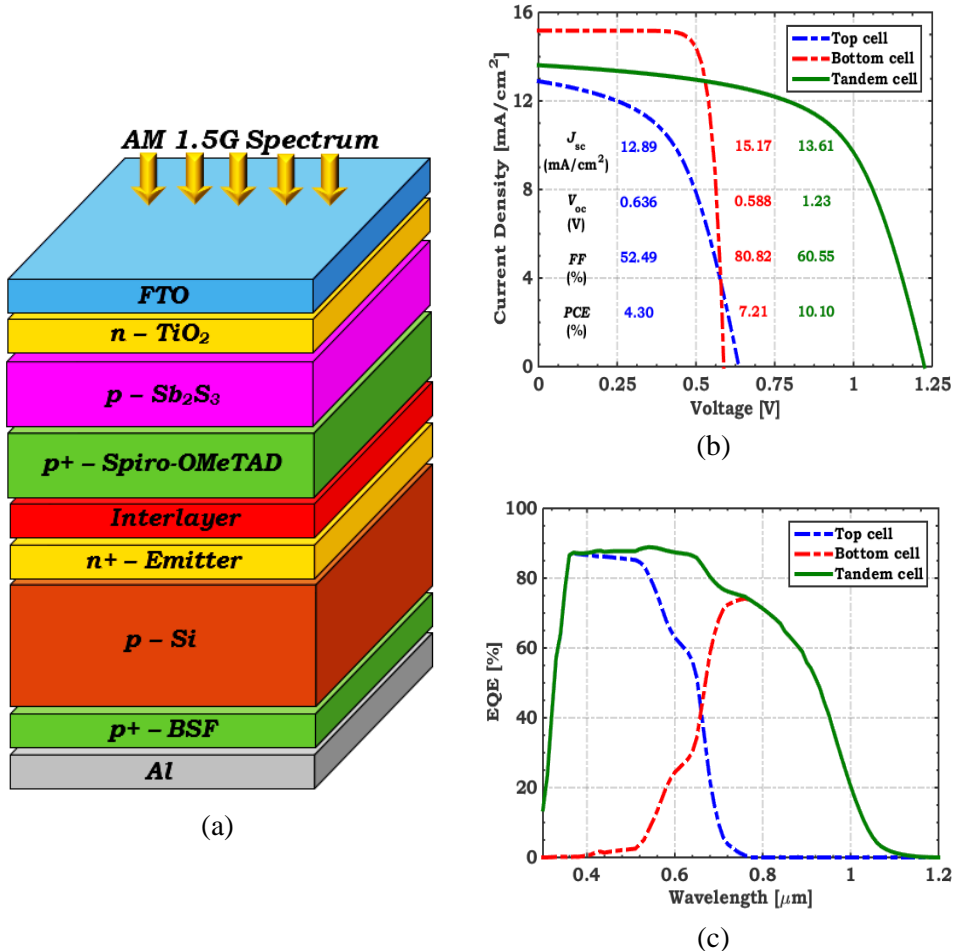


Figure 5.3 (a) Schematic illustration indicating basic layers, (b) the illuminated $J-V$ characteristics, and (c) EQE curve of an initial $\text{Sb}_2\text{S}_3/\text{Si}$ tandem cell.

5.3 Initial Enhancement of Sb_2S_3 Top Cell

The principal role of ETL and HTL is to ease the extraction of photogenerated carriers from the absorber layer to both contacts. Nonetheless, interface defects at the Sb_2S_3 interfaces promote electron and hole recombination and

degrade overall solar cell performance [102,103]. To improve Sb_2S_3 top cell performance while avoiding the technological and financial challenges associated with HTL, we continue to design the cell without an HTL and with a ternary compound ETL, as shown in **Figure 5.4**. So, the cell is designed as an HTL-free cell meaning that it is an np heterojunction instead of the conventional nip structure. This configuration implies that the p-absorber (Sb_2S_3 in our case) will serve as both an absorber and as a hole transporting layer without the need for an extra layer.

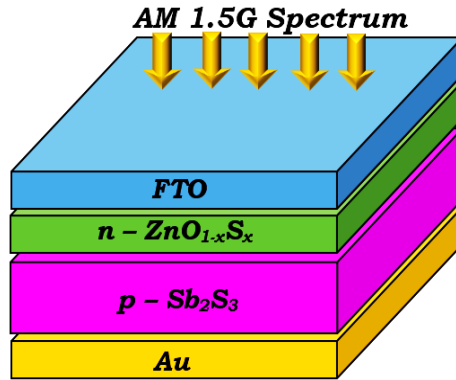


Figure 5.4 The proposed structure of HTL-free Sb_2S_3 top cell.

Since the selectivity of the ETL affects the solar cell performance, primarily characterized by energetics and transport features such as band alignment and charge carrier mobility, perfect ETL can significantly reduce interfacial recombination. An optimum CBO can be obtained by performing a suitable band alignment at the ETL/ Sb_2S_3 interface [104]. CBO is a crucial factor in determining V_{oc} and cell efficiency, and it is described as

$$CBO = \Delta E_c = \chi_{\text{absorber}} - \chi_{\text{ETL}} \quad (5.1)$$

At the interface, there are three options for band alignment, as illustrating in **Figure 5.5**. The first is a cliff-like band offset by a negative CBO value. A positive CBO spike-like band offset is the second encountered condition. Finally, a flat band condition derives from the third potential situation for a zero CBO. The cliff-like band offset at the interface is well known to cause severe

interface recombination [105]. Furthermore, a substantial spike-like band offset, which signifies a CBO greater than 0.3 eV, may inhibit interface carrier transfer [105]. Generally, a flat band or a slight spike-like band offset is preferable in thin film solar cells [106].

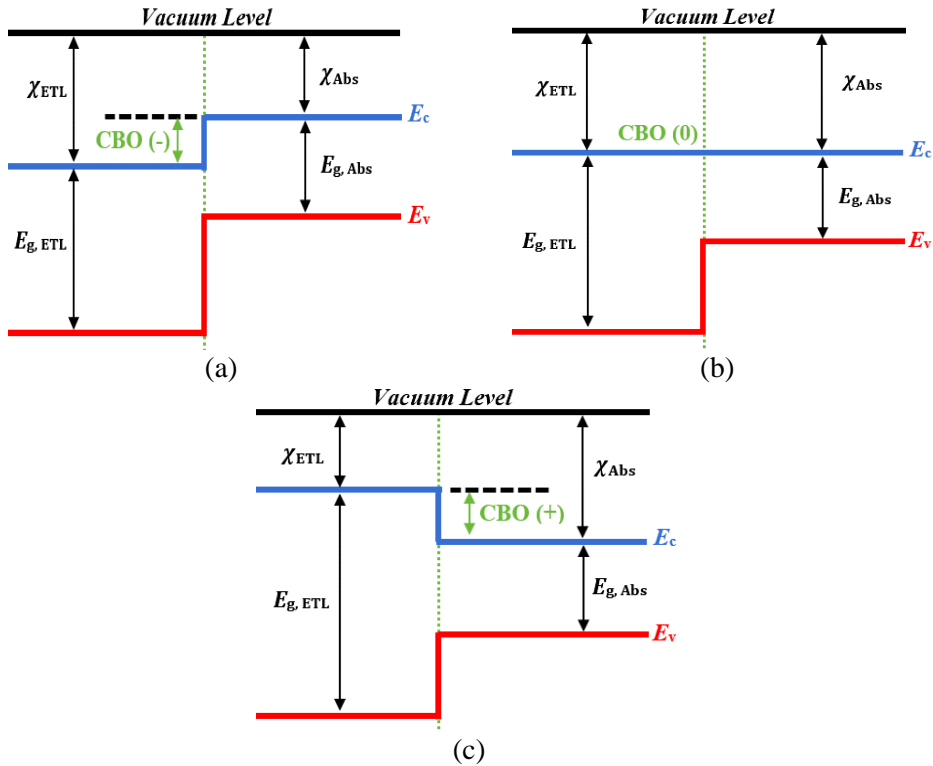


Figure 5.5 Schematic energy band diagram illustrating various cases of CBOs: (a) a cliff-like band offset, (b) a flat band offset, and (c) a spike-like band offset.

Herein, we apply the ternary compound $\text{ZnO}_{1-x}\text{S}_x$ as an ETL to tune the interface band alignment. $\text{ZnO}_{1-x}\text{S}_x$ and bilayer $\text{ZnO}_{1-x}\text{S}_x/\text{CdS}$ ETLs have been used in antimony chalcogenide-based solar cells with promising results [107,108]. The variation of bandgap energy (E_g), and electron affinity (χ) of $\text{ZnO}_{1-x}\text{S}_x$ with sulfur (S) content percentage were extracted from the literature [109], as illustrated in **Figure 5.6(a)**. In addition, **Figure 5.6(b)** presents the variation of $\text{ZnO}_{1-x}\text{S}_x$ CBO with S content. Moreover, the refractive index n'

and extinction coefficient κ dependency on wavelength of $\text{ZnO}_{1-x}\text{S}_x$ were obtained from experimental data [109,110]. **Figure 5.7** depicts the dependence of performance metrics on S content. As illustrated in **Figure 5.7**, all performance parameters almost follow the same trend for S content values in the range less than 80%. They gradually increase with increasing S content and almost saturate above $S = 60\%$. Although V_{oc} increases with $S > 80\%$, other parameters decrease, especially FF which decreases significantly. The maximum PCE is attained when $S = 80\%$, resulting in almost zero CBO and hence a flat band offset. As a result, $\text{ZnO}_{0.2}\text{S}_{0.8}$ is a suitable material for use as ETL in the proposed HTL-free sub-cell.

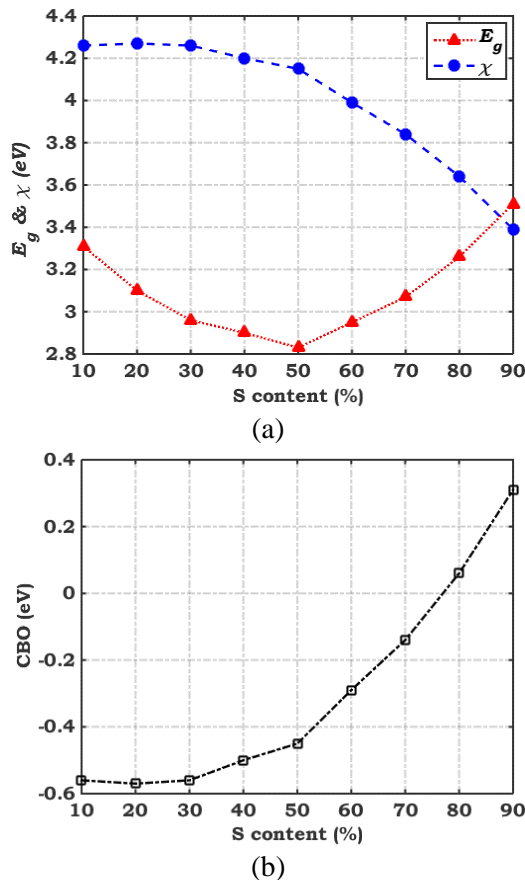


Figure 5.6 Variation in (a) E_g and χ and (b) CBO of $\text{ZnO}_{1-x}\text{S}_x$ depending on the S content percent.

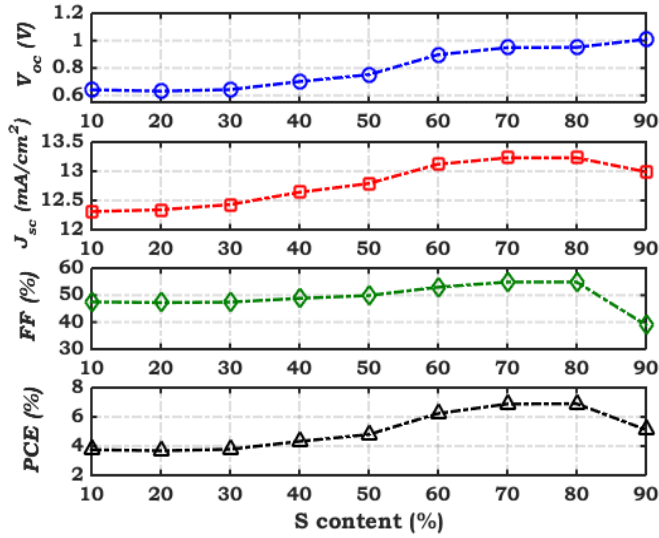


Figure 5.7 Performance parameters of $ZnO_{1-x}S_x$ with different S content.

For a physical explanation of the results shown in **Figure 5.7**, representative band diagrams of three distinct CBOs are plotted, as well as the recombination rate along the absorber, as illustrated in **Figure 5.8**. The first CBO is -0.57eV for $ZnO_{0.8}S_{0.2}$, which shows a cliff-like band in **Figure 5.8(a)**. The second one, shown in **Figure 5.8(b)**, is 0.31eV for $ZnO_{0.1}S_{0.9}$ with a spike-like band. The last is 0.06eV for $ZnO_{0.2}S_{0.8}$, which has a nearly flat band, as depicted in **Figure 5.8(c)**. Although the cliff band case, depicted in **Figure 5.8(a)**, does not impede the extraction of photogenerated electrons from the absorber layer to the front metal, it affects the activation energy associated with carrier recombination. In this case, the activation energy (E_a) is less than the absorber bandgap (E_g), and thus the dominant recombination process within the solar cell is the interfacial recombination losses [104,111]. Remarkably, E_a has a direct influence on V_{oc} ; thus, V_{oc} is decreased for S content values less than 70% (negative CBO values), as illustrated in **Figure 5.7**. Conversely, a spike is formed at the $ZnO_{0.1}S_{0.9}/Sb_2S_3$ interface, as shown in **Figure 5.8(b)**. This spike obstructs the extraction of photoexcited electrons from the absorber layer toward the front metal. When the spike is sufficiently low, it

becomes ineffective, allowing electrons to flow properly towards the contact. However, as in the $\text{ZnO}_{0.1}\text{S}_{0.9}/\text{Sb}_2\text{S}_3$ case, the spike is too high, significantly altering the regular flow of electrons toward the front metal. Consequently, the cell's equivalent series resistance rises, resulting in fill factor deterioration (see **Figure 5.7**) [13,112,113].

Finally, a flat band is formed at the $\text{ZnO}_{0.2}\text{S}_{0.8}/\text{Sb}_2\text{S}_3$ interface, as shown in **Figure 5.8(c)**. In this case, no barrier obstructs the carrier flow, and E_a is not compromised, resulting in a higher V_{oc} value. As a result, the optimum case is the flat band case. The recombination rate of the three situations is depicted in **Figure 5.8(d)** to confirm these findings. $\text{ZnO}_{0.2}\text{S}_{0.8}$ has the lowest recombination rate along the absorber layer. Therefore, with $\text{PCE} = 6.90\%$, $\text{ZnO}_{0.2}\text{S}_{0.8}$ is the best selection for the ETL in the proposed HTL-free cell. In addition, **Figure 5.9(a)** and **(b)** depict a comparison between the illuminated $J-V$ and EQE curves concerning the initial and the HTL-free cells using TiO_2 , $\text{ZnO}_{0.4}\text{S}_{0.6}$, and $\text{ZnO}_{0.2}\text{S}_{0.8}$ as ETLs. Their performance metrics are listed in **Table 5.3**. The results show that when the ETL is appropriately designed, there is a significant improvement. A percentage rise of about 60% is yielded when $\text{ZnO}_{0.2}\text{S}_{0.8}$ is designed as an ETL in the proposed HTL-free cell when compared to the initial conventional cell.

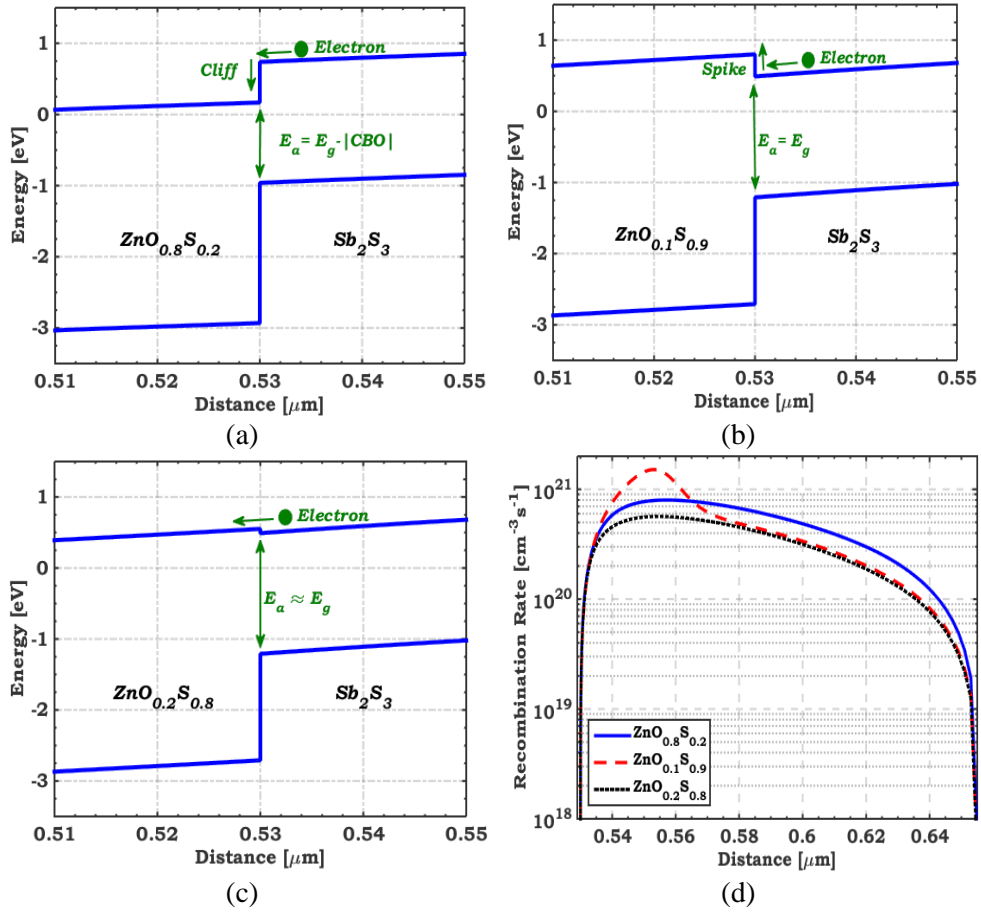


Figure 5.8 Energy band diagrams of three various cases of CBOs (a) a cliff-like band appears regarding ZnO_{0.8}S_{0.2}/Sb₂S₃, (b) a spike-like band occurs regarding ZnO_{0.1}S_{0.9}/Sb₂S₃ and (c) almost flat band regarding ZnO_{0.2}S_{0.8}/Sb₂S₃. (d) recombination rate along the Sb₂S₃ absorber layer.

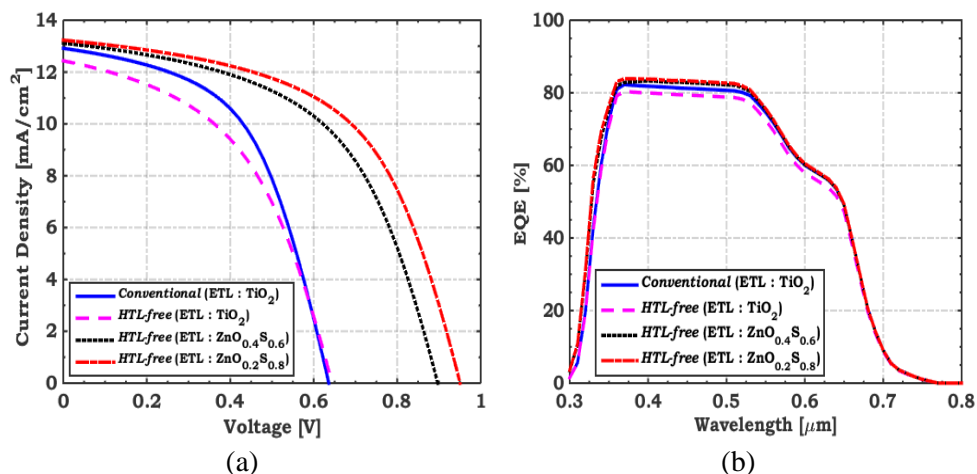


Figure 5.9 A comparison between (a) the illuminated $J-V$ and (b) EQE curves for the initial and HTL-free cells using TiO_2 , $\text{ZnO}_{0.4}\text{S}_{0.6}$, and $\text{ZnO}_{0.2}\text{S}_{0.8}$ as ETLs.

Table 5.3 A comparison between the solar cell performance metrics concerning the initial and HTL-free cells when utilizing TiO_2 , $\text{ZnO}_{0.4}\text{S}_{0.6}$, and $\text{ZnO}_{0.2}\text{S}_{0.8}$ as ETLs.

Structure	Conventional TiO_2	HTL-free TiO_2	HTL-free $\text{ZnO}_{0.4}\text{S}_{0.6}$	HTL-free $\text{ZnO}_{0.2}\text{S}_{0.8}$
V_{oc} (V)	0.636	0.644	0.897	0.951
J_{sc} (mA/cm^2)	12.91	12.44	13.12	13.23
FF (%)	52.45	47.46	52.95	54.88
PCE (%)	4.31	3.80	6.23	6.90

5.4 Tandem Cell Optimization

This subsection presents the following optimization steps for a 2T monolithic $\text{Sb}_2\text{S}_3/\text{Si}$ TSC. First, the impact of thickness and doping of the top cell ETL on the tandem performance is studied. Then, the effect of changing the absorber defect density and the series resistance of the top cell on the TSC performance is investigated. Furthermore, we investigated the impact of top and bottom absorber thicknesses on TSC working metrics. Finally, we inspected for the current matching point to get the maximum available PCE.

Figure 5.10 depicts the proposed structure utilized in the $\text{Sb}_2\text{S}_3/\text{Si}$ tandem cell optimization steps.

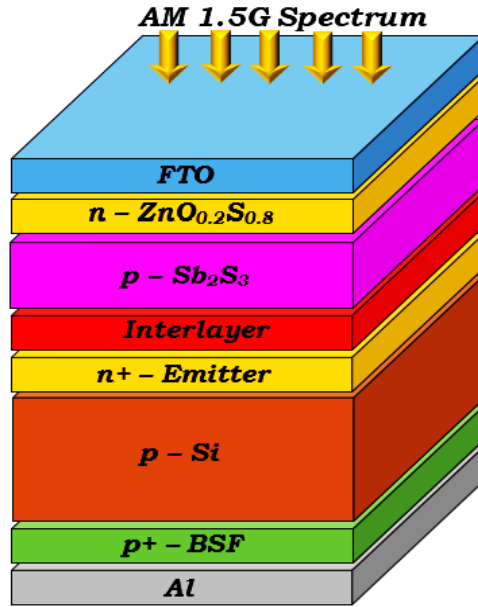


Figure 5.10 The proposed structure utilized in different optimization steps of the $\text{Sb}_2\text{S}_3/\text{Si}$ tandem cell.

5.4.1 Thickness and Doping of The Top Cell ETL

Changing the conductivity of different solar cell layers is critical in cell design. The amount of doping, which can be p -type or n -type depending on the type of dopants, can regulate conductivity. **Figure 5.11** describes the variation in tandem performance factors with variation in doping concentration of the top cell ETL. The doping density was changed from 1×10^{16} to 1×10^{19} cm^{-3} , while other parameters were fixed. As indicated in the figure, all performance parameters follow the same trend. They gradually increase and become constant beyond a concentration of 2×10^{18} cm^{-3} . Furthermore, the thickness was varied from 20 to 50 nm, while maintaining the other parameters unchanged. Owing to its wide bandgap (3.26eV), the ETL thickness has no effect on the tandem performance. Therefore, the ETL thickness is maintained unchanged (30 nm). The best performance is chosen when the ETL doping is

$5 \times 10^{18} \text{ cm}^{-3}$, where the Tandem metrics are ($J_{sc} = 14.19 \text{ mA/cm}^2$, $V_{oc} = 1.57 \text{ V}$, $\text{FF} = 63.50\%$, and $\text{PCE} = 14.15\%$).

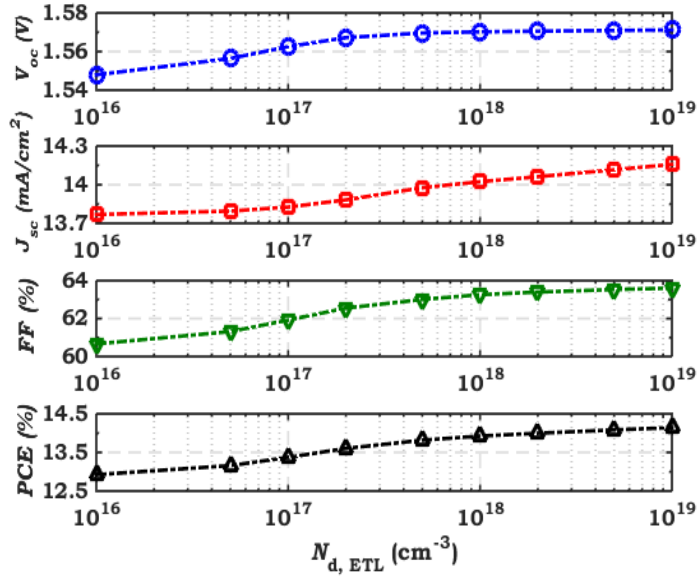


Figure 5.11 Variation in tandem performance parameters depending on variation in doping concentration of the top cell ETL.

To physically interpret this enhancement, the electric field distribution, and the spatial distribution of the electron conductivity at the maximum power point (MPP) before and after ETL optimization are plotted and shown in **Figure 5.12**. As illustrated in **Figure 5.12(a)**, increasing $\text{ZnO}_{0.2}\text{S}_{0.8}$ doping increases the electric field substantially, which in turn will increase the ability to separate carriers and collect them at the respective electrodes. Moreover, to comprehensively represent the carrier separation, the electron conductivity is plotted as seen in **Figure 5.12(b)**. Carrier conductivity is considered a key factor that controls the carrier separation in the solar cell [114]. As clarified in **Figure 5.12(b)**, increasing $\text{ZnO}_{0.2}\text{S}_{0.8}$ doping increases the electron conductivity in the $\text{ZnO}_{0.2}\text{S}_{0.8}$ and the $\text{ZnO}_{0.2}\text{S}_{0.8}/\text{Sb}_2\text{S}_3$ interface resulting in faster separation of photogenerated carriers, lower recombination rates, and improved cell performance. So, the enhancement resulting from the high doping

is accomplished due to the concurrent improvement of both the electric field as a driving force and the conductivity as a source of current enhancement.

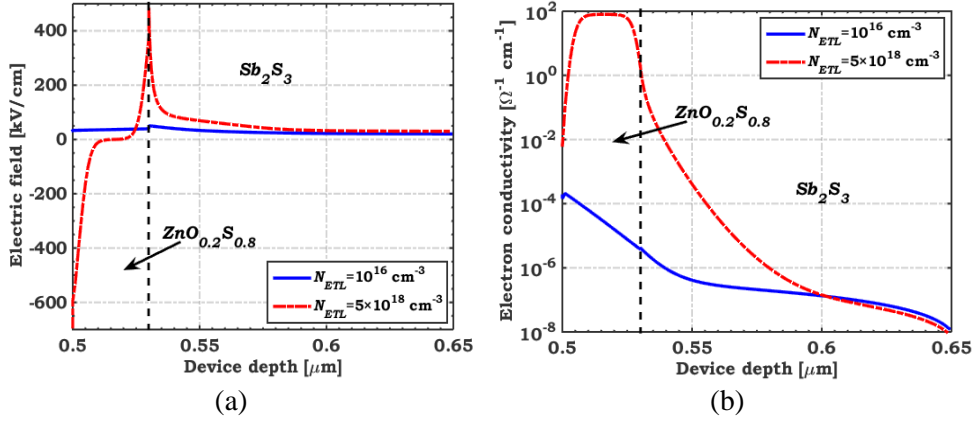


Figure 5.12 (a) The electric field distribution, and (b) the spatial distribution of the electron conductivity at the MPP before and after optimizing the top cell ETL.

5.4.2 Defect Density of The Sb_2S_3 Absorber

Figure 5.13 depicts the change in tandem cell performance metrics with the variation in bulk defect density of the top cell absorber. The defect density varies from 1×10^{12} to $5 \times 10^{16} \text{ cm}^{-3}$ while maintaining the other parameters unchanged. As the figure shows, all performance parameters follow the same trend. They are nearly constantly up to about $1 \times 10^{15} \text{ cm}^{-3}$ and then gradually degraded when increasing the defect density beyond this value. The defect density of $1 \times 10^{14} \text{ cm}^{-3}$ is adapted, at which output parameters are ($J_{sc} = 14.57 \text{ mA/cm}^2$, $V_{oc} = 1.61 \text{ V}$, $FF = 76.43\%$, and $PCE = 17.86\%$). This value of defect density was already reported in the literature upon the enhancement of fabrication methods [115,116]. This significant improvement in cell performance with decreasing defect density is attributed to decreased carrier recombination (which means higher diffusion lengths), as shown in **Figure 5.14**. The figure demonstrates the recombination rate (R) behavior for the absorber layer with various defect densities under short-circuit conditions. In addition, the generation rate (G) is shown to give a comparative figure. As expected, as trap

density grows, the recombination rate climbs dramatically, indicating poor performance. Several approaches, including trap state passivation in the Sb_2S_3 absorber layer, post-annealing and interlayer passivation, have been used to reduce defect density and increase carrier lifetime and V_{oc} [117].

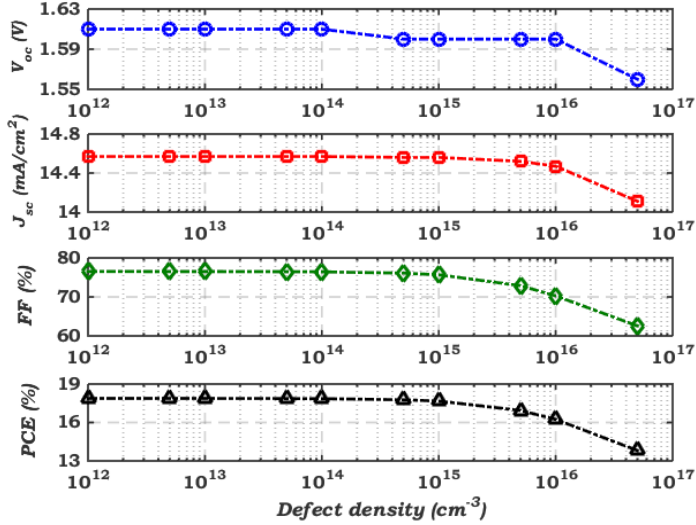


Figure 5.13 Variation in tandem performance parameters depending on the variation of the Sb_2S_3 absorber defect density.

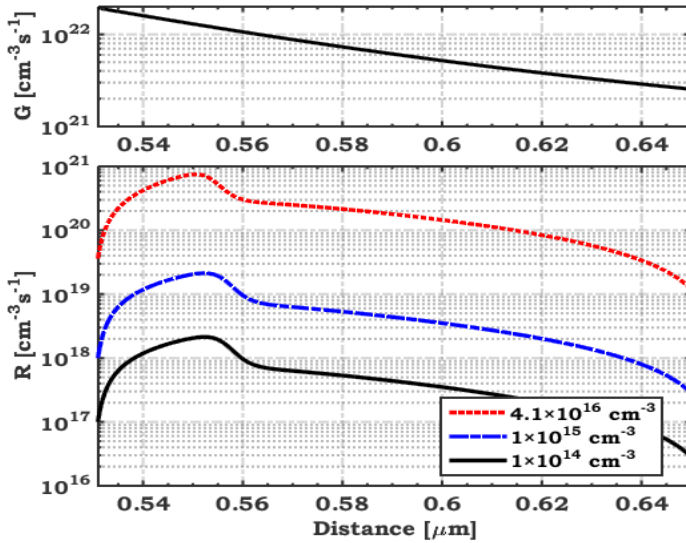


Figure 5.14 The generation and recombination rate behavior drawn at the illuminated short-circuit condition for the top absorber layer.

5.4.3 Series Resistance of The Top Cell

Solar cells' parasitic resistances lead to resistive effects, lowering their overall performance. The resistance of the cell layers, as well as metal contact resistances, cause the series resistance to appear. The fill factor (FF) is the most influenced factor by the series resistance. **Figure 5.15** shows the variation in tandem performance parameters as a function of the external series resistance (R_s). When R_s is increased from 0 (ideal case) to $10 \Omega \text{ cm}^2$, J_{sc} remain nearly unaffected while the FF decreases, resulting in efficiency reduction. The decrease in FF is due to more dissipating power with higher R_s . These results confirmed that R_s should be kept as low as possible to attain an efficient cell. The ideal case is chosen to inspect the limit of possible higher efficiencies utilized by the tandem cell. The solar cell metrics, in this case, are ($J_{sc} = 14.58 \text{ mA/cm}^2$, $V_{oc} = 1.61 \text{ V}$, $\text{FF} = 83.44\%$, and $\text{PCE} = 19.51\%$).

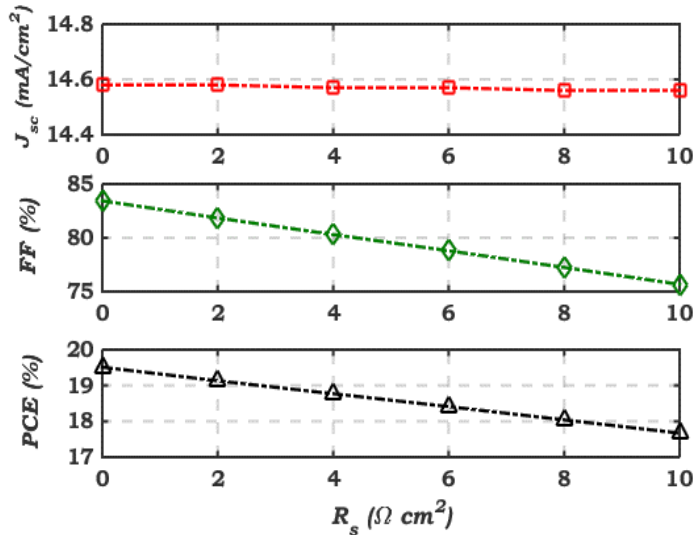


Figure 5.15 Variation of tandem performance parameters for different values of external series resistance.

5.4.4 Thicknesses of The Absorber Layers

Figure 5.16 presents the dependency of TSC efficiency on the thickness of both top and bottom absorber layers. To investigate device performance,

the thickness of the top absorber (t_{TA}) was increased from 75 up to 750 nm and that of the bottom absorber (t_{BA}) was increased from 20 to 50 μm while the other parameters remained constant. As can be inferred from the figure, the PCE was unaffected by increasing t_{BA} from 20 to 50 μm and keeping t_{TA} below 175 nm. As t_{TA} falls lower than 150 nm, the PCE steadily reduces from 21% to 16%. Thicknesses of top and bottom cells are selected to be 200 nm and 30 μm , respectively. The solar cell metrics, in this case, are ($J_{sc} = 16.47 \text{ mA/cm}^2$, $V_{oc} = 1.62 \text{ V}$, $\text{FF} = 83.88\%$, and $\text{PCE} = 22.31\%$).

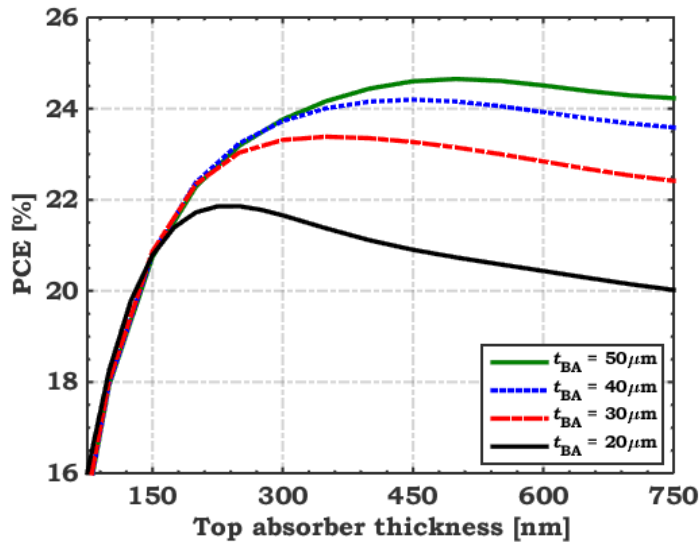


Figure 5.16 Tandem efficiency dependency on the thickness of the two absorber films.

5.4.5 Current Matching Point

In this part, the top cell's absorber thickness (t_{TA}) is changed from 200 to 350 nm, while the bottom c-Si thickness is fixed at 30 μm . **Figure 5.17(a)** displays the J_{sc} variation of the front and rear sub-cells against the thickness of the Sb_2S_3 absorber layer in the front cell, indicating considerable dependence on t_{TA} . As t_{TA} becomes thicker, J_{sc} of the top sub-cell increases, and that of the bottom sub-cell, in turn, declines. The reason is that the thicker the front cell is, the more photon absorption occurs, implying lesser transferred light to

the bottom sub-cell. A current matching point happens at $J_{sc} = 17.24 \text{ mA/cm}^2$ and $t_{TA} = 272 \text{ nm}$. Under this condition, the performance of the $\text{Sb}_2\text{S}_3/\text{c-Si}$ tandem cell has been simulated where the corresponding J - V curves of tandem, top, and back cells are represented in **Figure 5.17(b)**. The maximum value of J_{sc} is 17.24 mA/cm^2 with $V_{oc} = 1.63 \text{ V}$ and $\text{PCE} = 23.25\%$ for the TSC. The values of $V_{oc} = 1.63 \text{ V}$ and $\text{PCE} = 23.25\%$ are equal to the sum of those of the top cell ($V_{oc} = 1.05 \text{ V}$ and $\text{PCE} = 15.18\%$) and bottom cell ($V_{oc} = 0.58 \text{ V}$ and $\text{PCE} = 8.07\%$), demonstrating the efficient operation of the recombination junction.

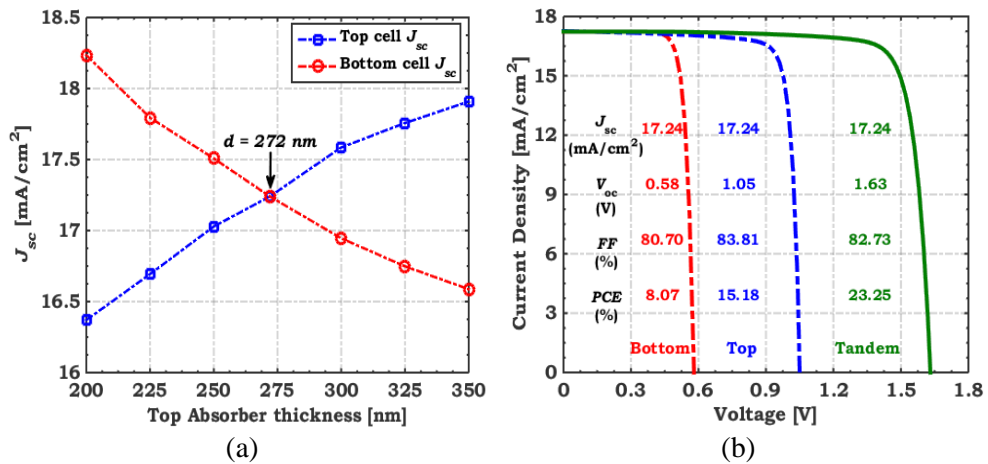


Figure 5.17 (a) J_{sc} of front- and rear-cells versus top absorber thickness. (b) J - V characteristics of tandem-, front-, and back-cells under current matching point and $30\mu\text{m}$ bottom cell absorber.

The performance parameters for $\text{Sb}_2\text{S}_3/\text{Si}$ tandem cells under various optimization steps are presented in **Table 5.4**. Further, **Figure 5.18** depicts PCE of the various optimization steps and the improvement percentage in PCE over the previous step. The most significant effect parameters among the various factors are the optimization of N_t and CBO, which provide 36.73% and 28.51% enhancement relative percentages, respectively. This highlights the significance of trap state passivation in the Sb_2S_3 film and CBO engineering

in reducing defect density and avoiding interface recombination that negatively impacts the cell performance. In addition, **Figure 5.19** displays the illuminated J - V characteristics and EQE curves of a conventional and a final optimized tandem cell. This considerable improvement in tandem performance is attributed to the overall optimization steps, which attained a maximum PCE of 23.25% with a relative percentage enhancement of 130.20% compared with the initial TSC.

Table 5.4 A comparison between the performance metrics for Sb_2S_3/Si tandem cells under various optimization steps.

Cell Structure	J_{sc} (mA/cm ²)	V_{oc} (V)	FF (%)	PCE (%)
Initial	13.61	1.23	60.55	10.10
Optimized CBO	13.84	1.55	60.63	12.98
Optimized ETL	14.19	1.57	63.50	14.15
Optimized N_t	14.57	1.61	76.43	17.86
Optimized R_s	14.58	1.61	83.44	19.51
Optimized t_{abs}	16.47	1.62	83.88	22.31
Final Optimization	17.24	1.63	82.73	23.25

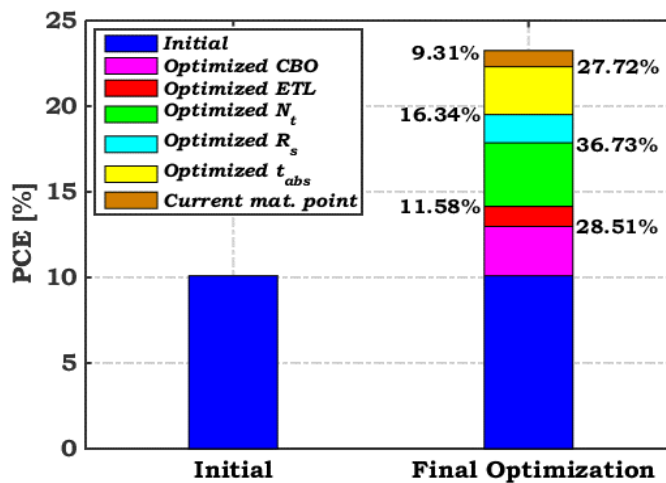


Figure 5.18 Calculated efficiency improvements for different cases of tandem cells showing the enhancement relative percentage.

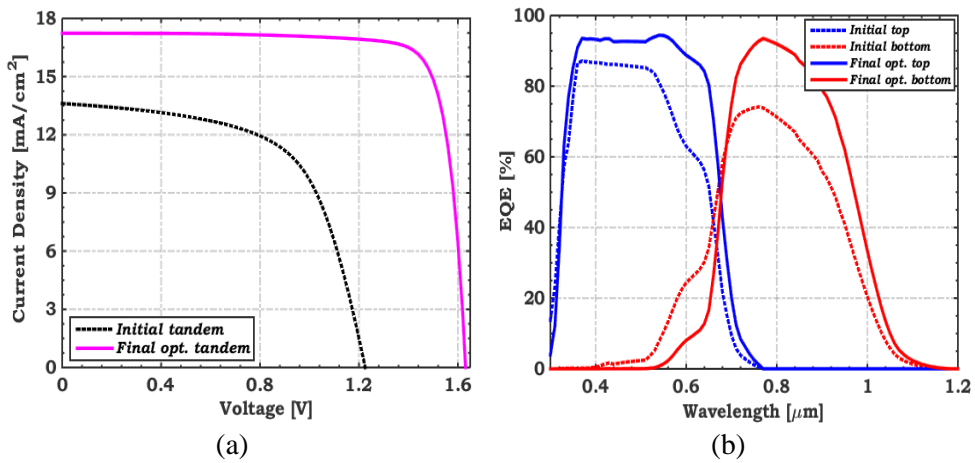


Figure 5.19 A comparison between (a) illuminated $J-V$ and (b) EQE curves of an initial and a final optimized tandem cell.

Moreover, we investigated the effect of bottom absorber thickness by extending it to $50 \mu\text{m}$, which is the limit for thin film silicon solar cells [118–121]. In this context, the current matching point is evaluated by engineering the top cell thickness to get the best tandem performance, as illustrated in **Figure 5.20**. In this case, the top absorber thickness is varied from 275 to 475 nm resulting in current matching point at $d = 375 \text{ nm}$. Under this condition, the performance metrics of the optimized TSC are ($J_{sc} = 18.04 \text{ mA}/\text{cm}^2$, $V_{oc} = 1.64 \text{ V}$, $FF = 82.41\%$, and $PCE = 24.34\%$).

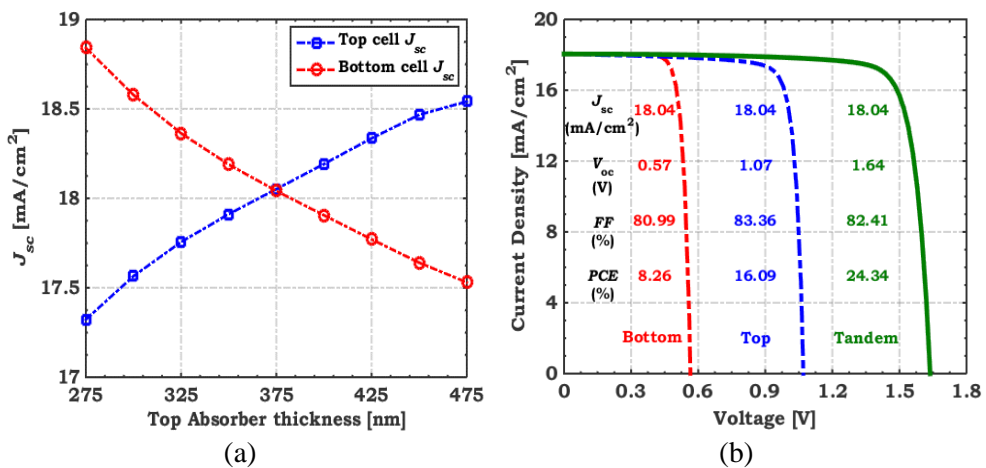


Figure 5.20 (a) J_{sc} of front- and rear-cells versus d of top cell absorber film. (b) $J-V$ characteristics of tandem-, front-, and back-cells under current matching point and $50 \mu\text{m}$ bottom cell absorber.

5.5 Summary

This chapter presented a simulation study for a 2T monolithic $\text{Sb}_2\text{S}_3/\text{Si}$ tandem cell combining a Sb_2S_3 top sub-cell (1.7) eV and a thin c-Si bottom sub-cell (1.12 eV). The standalone top and bottom sub-cells are calibrated versus experimental data, giving a PCE of 4.31% and 14.26%, respectively. The initial tandem cell achieves a PCE of 10.10%, implying that the top cell should be optimized in order to surpass the PCE of the bottom cell. Thus, the Sb_2S_3 top cell is optimized by designing an HTL-free np heterojunction cell and tuning CBO between the ETL and the Sb_2S_3 absorber. Then, we optimize the tandem cell by inspecting the appropriate ETL thickness and doping concentration. Also, the impact of changing the absorber defect density and the series resistance of the top cell on the tandem performance is investigated to get the maximum available PCE. At defect density of $1 \times 10^{14} \text{ cm}^{-3}$ and ideal zero series resistance, the tandem efficiency is improved from 10.10% to 19.51%. Additionally, we have inspected the consequence of the top absorber thickness on TSC performance parameters for two cases of bottom absorber thickness (t_{Si}). At the designed matching point for each case, the optimum efficiency was achieved giving $J_{\text{sc}} = 17.24 \text{ mA/cm}^2$, and PCE = 23.25% for $t_{\text{Si}} = 30 \text{ }\mu\text{m}$, while $J_{\text{sc}} = 18.04 \text{ mA/cm}^2$, and PCE = 24.34% for $t_{\text{Si}} = 50 \text{ }\mu\text{m}$. These results can provide potential routes for advancing low-cost, environmentally friendly, and efficient thin film tandem solar cells which can be used in flexible applications.

This page is intentionally left blank

CHAPTER 6
POLYMER/SILICON TANDEM
CELL

This page is intentionally left blank

CHAPTER 6

POLYMER/SILICON TANDEM CELL

6.1 Introduction

Recently, Bulk heterojunction polymer solar cells are gaining attention as they have the potential to provide flexible, lightweight, and cost-effective alternatives to silicon-based solar cells [48]. Researchers have been working on improving the charge selectivity of inverted polymer-based solar cells by inserting a sub-monolayer of dyes containing functional cyano-carboxylic at the interface between the inorganic metal oxide (ZnO) and organic active layer, resulting in an improved conversion efficiency to 3.52% [49]. Y. Yan et al. [50] recently synthesized and used TiO₂ nanoparticles as the electron-transport layer in single-junction inverted polymer solar cells, resulting in a high FF of 72% and the best PCE of 10.55%, making it one of the best single-junction inverted polymer solar cells ever reported, with superior stability under ambient conditions when compared to conventional device configuration.

This chapter proposes a 2T monolithic TSC combining a top polymer-based sub-cell with a bottom thin film c-Si sub-cell. Solar cells established on these materials, which are cost-effective to manufacture, are considered environmentally sustainable. When all the layers are thin film, a flexible tandem can be produced and employed in various uses, including wearable devices. We calibrate the separate sub-cells against experimental investigations to validate our simulator, considering the proper geometric and physical considerations before modeling our suggested TSC. Next, we optimize the tandem performance by tuning the valence band offset (VBO) of the top sub-cell. Then, the influence of varying the top absorber defect density on the tandem performance is investigated. Furthermore, we vary the thickness of both absorbers to boost the tandem efficiency. Finally, the current matching point is inspected

for maximum obtainable PCE. The provided TCAD simulation study can shed light on an emerging technology that could become one of the top alternative materials for thin Si-based TSCs.

6.2 Simulator Validation and Device Structures

6.2.1 Validation of Silvaco Atlas Simulator

This study uses the Silvaco TCAD simulator to model and simulate the proposed tandem cell's electrical and optical characteristics. The physical models incorporated into Atlas are selected as follows. The Shockley–Read–Hall (SRH) mechanism is allowed to consider the trap recombination through the bandgap defect levels of the simulated material. In addition, the models for optical recombination, Fermi-Dirac distribution, and concentration-dependent mobility are also utilized. In a 2T TSC, the two sub-cells are interconnected using a 10 nm interlayer of ITO material as a common electrode allowing effective current transport across the tandem sub-cells [70]. Appropriate lumped resistance ($10^{16} \Omega$) is added to the common electrode to prevent the flow of current in the added electrode and to force the current to flow within the tandem cell without significant limitation.

We utilized a homojunction bottom c-Si cell which is calibrated against an experimental thin c-Si cell, as mentioned in **subsection 5.2.1**. On the other hand, an $n-i-p$ heterojunction polymer top cell is presented on the basis of an experimental solar cell structure [122]. The active layer blends PDTBTBz-2F as the polymer donor and PC₇₁BM as the fullerene acceptor. Photogenerated electron-hole pairs (EHP) are extracted by sandwiching the active layer between low n -type doped Zinc oxide (ZnO) and high-doped p^+ -PEDOT:PSS layers. The schematic structure and energy band profile of the polymer-based top cell are illustrated in **Figure 6.1(a)** and (b), respectively. **Table 6.1** pre-

sents the layers' essential parameters obtained from previously available investigations [19,20,122–125]. **Table 6.2** also includes defect parameters in the absorber layer and at the two interfaces (ZnO/Polymer and Polymer/PEDOT:PSS). The front indium-doped tin oxide (ITO) contact has a work function of 4.4 eV, whereas the work function of the back Ag contact is considered 4.74 eV. The illuminated (AM1.5G) current-voltage (J - V) curves are presented in **Figure 6.1(c)** for both simulated and experimental data [122]. In addition, the simulated external quantum efficiency (EQE) curve is also shown in **Figure 6.1(d)**. The simulated cell gives: ($J_{sc} = 13.35 \text{ mA/cm}^2$, $V_{oc} = 1 \text{ V}$, $FF = 74.44\%$, and $PCE = 10\%$). These PV parameters agree with the reported experimental parameters, as shown in the inset of **Figure 6.1(c)**, implying that the simulation model employed in Silvaco Atlas software has been validated.

Table 6.1 Basic parameters of polymer sub-cell layers.

Parameters	ZnO	PDTBTBz-2F:PC ₇₁ BM	PEDOT:PSS
t (μm)	30	110	30
E_g (eV)	3.2	1.39	1.3
χ (eV)	4.26	4.11	3.6
ϵ_r	9	3	3.5
μ_n (cm^2/Vs)	200	1.1×10^{-3}	1×10^{-4}
μ_p (cm^2/Vs)	5	1.15×10^{-3}	2×10^{-5}
N_c (cm^{-3})	2×10^{18}	1×10^{20}	1×10^{21}
N_v (cm^{-3})	1.8×10^{19}	1×10^{20}	1×10^{21}
N_D (cm^{-3})	1×10^{17}	-	-
N_A (cm^{-3})	-	-	1×10^{19}
References	[123]	[19,20,122,124]	[125]

Table 6.2 Defects parameters in the top absorber layer and at the interfaces [19,20].

Parameter	Interface Defects		Bulk Defects
	ZnO/Polymer	Polymer/PEDOT:PSS	Polymer
Defect type	Neutral	Neutral	Acceptor
Carriers capture cross-section	$1 \times 10^{-15} \text{ cm}^2$	$1 \times 10^{-15} \text{ cm}^2$	$1 \times 10^{-15} \text{ cm}^2$
Energetic distribution	Single	Single	Single
Energy level to the highest E_v	0.6 eV	0.6 eV	0.6 eV
Total density	$5 \times 10^6 \text{ cm}^{-2}$	$5 \times 10^6 \text{ cm}^{-2}$	$1 \times 10^{11} \text{ cm}^{-3}$

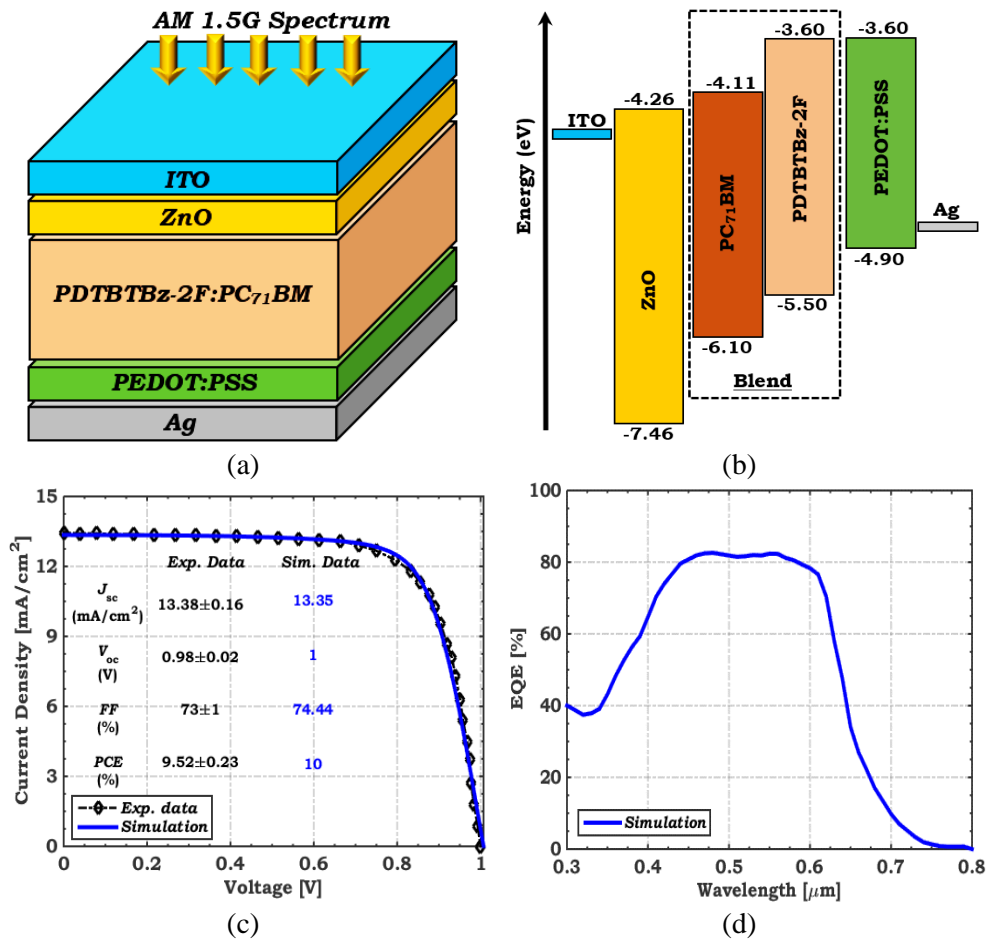


Figure 6.1 (a) Basic layers structure, (b) Energy band profile before contact, (c) Comparison of the simulated $J-V$ curve with the measured data [122] under AM 1.5 illumination condition, and (d) EQE of a polymer-based cell.

6.2.2 Initial Polymer/Si Tandem Cell

This subsection presents the suggested structure of the polymer/Si TSC, as shown in **Figure 6.2(a)**. As previously stated, in a 2T TSC, the two sub-cells are interconnected using a 10 nm interlayer of ITO material as a common electrode that is modeled by a lumped resistance. Furthermore, the lower current that passes through either sub-cell controls the TSC current. Therefore, current

matching situation should be maintained to reduce the current loss. The designed configuration combines a wide bandgap polymer top cell with a thin c-Si bottom cell. **Figure 6.2(b)** and (c) display the simulation results (J - V and EQE) of the TSC. The corresponding PV parameters are as follows: $J_{sc} = 13.39$ mA/cm², $V_{oc} = 1.60$ V, FF = 77.61%, and PCE = 16.58%. The results show that the smallest sub-cell current regulates the tandem current, while the tandem V_{oc} is almost equivalent to the sum of the standalone sub-cells' V_{oc} .

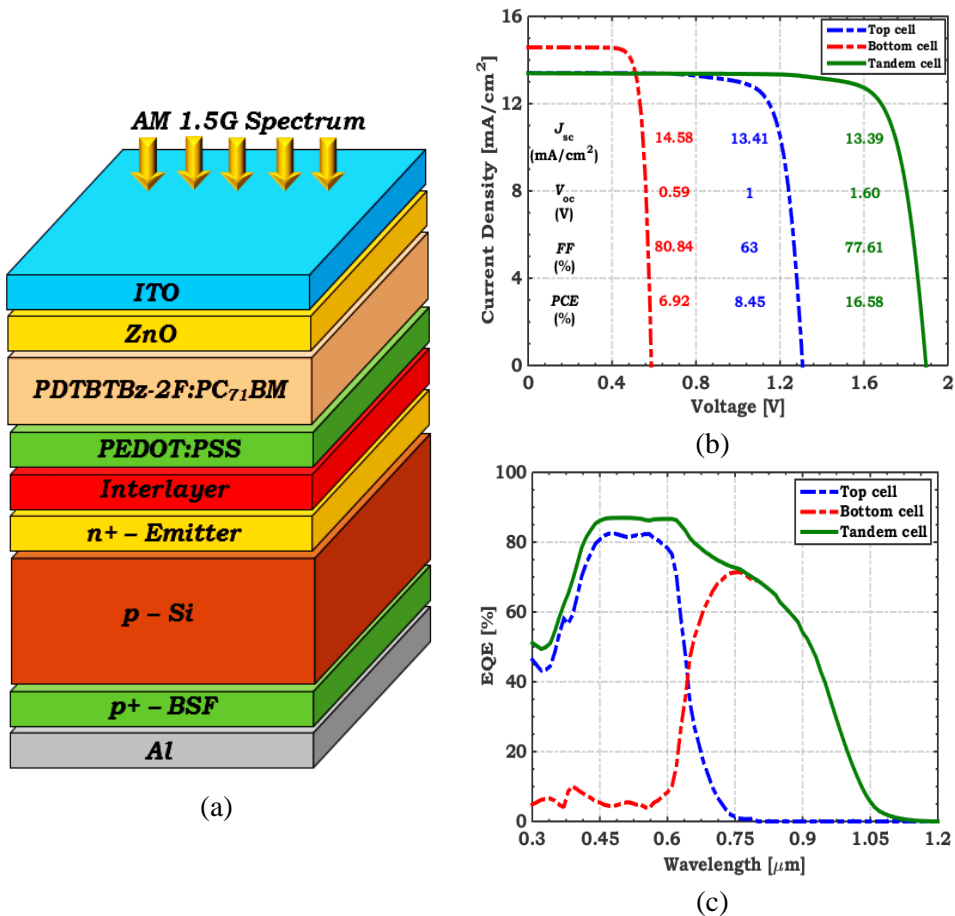


Figure 6.2 (a) Basic layers structure, (b) Illuminated J - V , and (c) EQE curves of an initial polymer/Si TSC.

6.3 Tandem Cell Optimization

In this section, we handle the optimization steps for the polymer/Si TSC. First, the VBO impact of the front sub-cell on the TSC performance is examined. Then, we investigate the influence of changing the defect density of the top absorber on tandem working metrics. Furthermore, the influence of both absorber thicknesses on tandem performance is investigated. Finally, the CMP is inspected for maximum conversion efficiency.

6.3.1 Valence Band Offset of The Top Cell

Generally, ETLs and HTLs help to extract photogenerated EHP from the absorber layer, which is then transported to each contact. The selectivity of the carriers' transport layers influences the performance of solar cells. Consequently, a well-designed transport layer should pass one type of carriers and reject the other type. In addition, perfect transport layers should significantly suppress interfacial recombination. An optimum band offset can be achieved using an appropriate band alignment at both interfaces [104]. Initially, a polymer material (PEDOT:PSS) is utilized as an HTL for the top cell. As depicted in **Figure 6.3**, the VBO for PEDOT:PSS is -0.6 eV (large hole cliff).

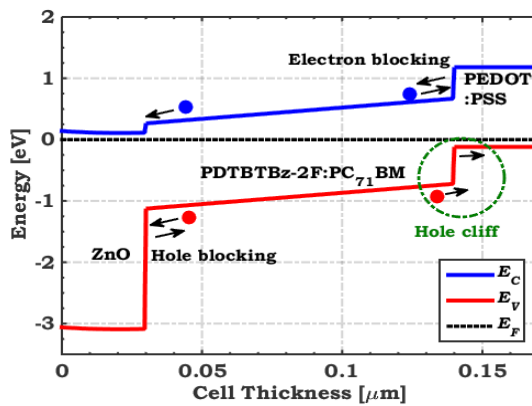


Figure 6.3 Energy band profile of tandem top cell with initial transport layers (ZnO and PEDOT:PSS).

VBO play a vital role in determining V_{oc} and thus cell efficiency, and it is described as [104],

$$VBO = \Delta E_V = (\chi + E_g)_{HTL} - (\chi + E_g)_{absorber} \quad (6.1)$$

At the interface, there are three options for band alignment, as illustrating in **Figure 6.4**. The first is a cliff-like band offset by a negative VBO value. A positive VBO spike-like band offset is the second encountered condition. Finally, a flat band condition derives from the third potential situation for a zero VBO. The cliff-like band offset at the interface is well known to cause severe interface recombination [105]. Furthermore, a substantial spike-like band offset, which signifies a VBO greater than 0.3 eV, may inhibit interface carrier transfer [105]. In thin-film solar cells, it is generally preferred that the bands be flat or have a slight spike-like band offset [106]. So, we have to substitute PEDOT:PSS with a suitable HTL to adjust the interface band alignment. As a theoretical study, VBO is varied from -0.6 to 0.5 eV with different electron barrier values. **Figure 6.5** exhibits the tandem conversion efficiency with different electron barriers as a function of the VBO of the Polymer/PEDOT:PSS interface. As depicted in **Figure 6.5**, the optimum range of VBO is from -0.3 to 0.3 eV with an electron barrier higher than 0.5 eV.

To get the best tandem performance, we apply various materials such as CBTS, CuO, Cu₂O, and P3HT, which fulfill the optimum VBO and electron barrier values. **Table 6.3** summarizes these materials' main required parameters, indicating each material's VBO and electron barrier values at the HTL terminal. In addition, **Figure 6.6** compares the illuminated $J-V$ characteristics regarding the initial and TSCs when employing P3HT, CuO, Cu₂O, and CBTS as top HTLs. Their PV parameters are presented in **Table 6.4**. It is clear that when the top cell VBO is adequately designed, the tandem FF is enhanced, and thus the overall performance is improved. The highest performance is

achieved when CBTS is utilized as a top HTL, resulting in an improvement of 25.15% over the initial TSC.

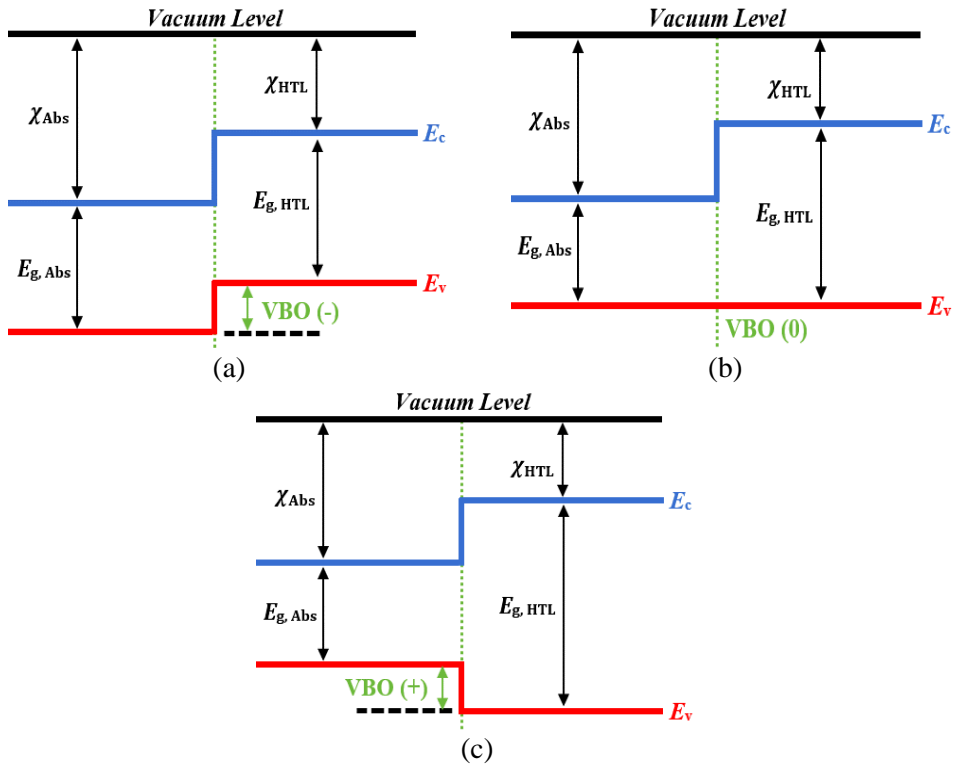


Figure 6.4 Schematic energy band diagram illustrating various cases of VBOs: (a) a cliff-like band offset, (b) a flat band offset, and (c) a spike-like band offset.

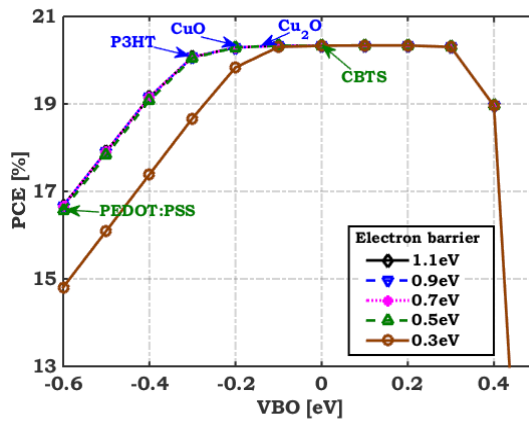
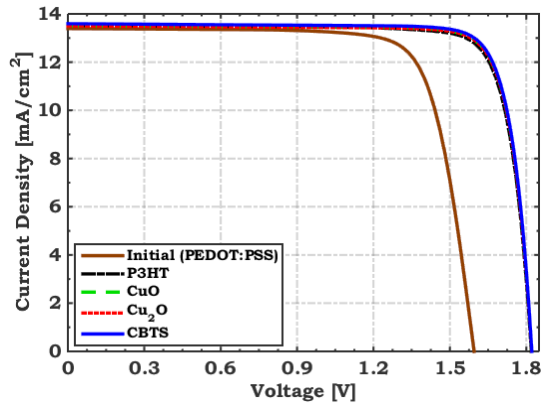


Figure 6.5 A theoretical study for conversion efficiency dependency on VBO of top HTL layer with different electron barriers.

Table 6.3 Basic parameters of various top HTL materials.

Parameters	CBTS	P3HT	Cu ₂ O	CuO
E_g (eV)	1.9	2	2.17	2.1
χ (eV)	3.6	3.2	3.2	3.2
VBO (eV)	0	-0.3	-0.13	-0.2
EB (eV)	0.51	0.91	0.91	0.91
ϵ_r	5.4	3	7.1	7.11
μ_n (cm ² /Vs)	30	1×10^{-4}	200	3.4
μ_p (cm ² /Vs)	10	1×10^{-3}	80	3.4
N_c (cm ⁻³)	2.2×10^{18}	1×10^{21}	2.5×10^{18}	2.2×10^{18}
N_v (cm ⁻³)	1.8×10^{19}	1×10^{21}	1.8×10^{19}	1.8×10^{18}
References	[126]	[17]	[127]	[32]

**Figure 6.6** A comparative analysis between the illuminated J - V characteristics for the initial and TSCs utilizing P3HT, CuO, Cu₂O and CBTS as top HTLs.**Table 6.4** PV parameters for the initial and TSCs using P3HT, CuO, Cu₂O and CBTS as top HTLs.

Top HTL	V_{oc} (V)	J_{sc} (mA/cm ²)	FF (%)	PCE (%)
Initial (PEDOT:PSS)	1.60	13.39	77.61	16.58
P3HT	1.82	13.52	82.94	20.41
CuO	1.82	13.51	83.80	20.62
Cu ₂ O	1.82	13.50	83.80	20.60
CBTS	1.82	13.59	83.82	20.75

Figure 6.7 illustrates the energy band profiles of two different VBOs, which physically interpret the findings in **Figure 6.6**. First, the VBO for P3HT is -0.3 eV, which is indicated by the cliff-like band in **Figure 6.7(a)**. The second for CBTS, displayed in **Figure 6.7(b)**, has a flat band. The cliff-like band situation helps to extract photogenerated holes from the absorber film to the HTL, but it decreases the activation energy required for carrier recombination. Thus, the principal recombination mechanism in the cell is recombination losses at the interfaces, where the activation energy (E_a) is less than the absorber bandgap (E_g), resulting in fill factor degradation [104,111]. Finally, as shown in **Figure 6.7(b)**, a flat band is created at the CBTS/Absorber interface. In this case, the carrier flow is not interrupted, and E_a remains unaffected, leading to a higher FF value. Consequently, the flat band case is considered to be the most appropriate case. Therefore, with PCE = 20.75%, CBTS is the best choice for the top HTL.

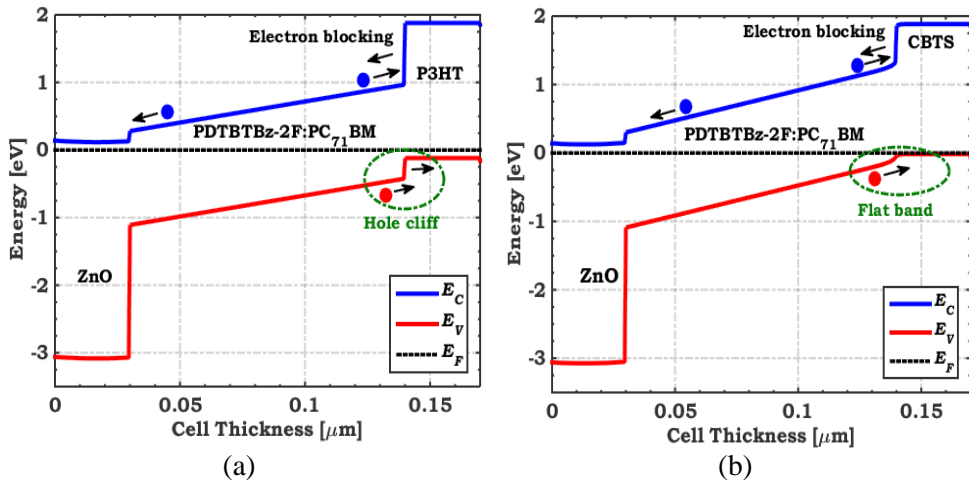


Figure 6.7 Energy band diagrams of (a) a cliff-like band occurs concerning P3HT/Absorber and (b) a flat band concerning CBTS/Absorber.

6.3.2 Defect Density of The Polymer Absorber

Figure 6.8 depicts the change in tandem cell performance metrics with the variation in bulk defect density of the polymer absorber. The defect density varies from 1×10^{10} to $1 \times 10^{14} \text{ cm}^{-3}$ while maintaining the other parameters unchanged. As the figure shows, all performance parameters follow the same trend. They are constantly up to about $1 \times 10^{11} \text{ cm}^{-3}$ and then gradually degraded when increasing the defect density beyond this value. The defect density of $1 \times 10^{11} \text{ cm}^{-3}$ is selected and output parameters, in this case, are ($J_{sc} = 13.59 \text{ mA/cm}^2$, $V_{oc} = 1.82 \text{ V}$, $FF = 83.82\%$, and $PCE = 20.75\%$). The decline in cell performance with increasing defect density is attributed to increased carrier recombination (which means lower diffusion lengths), as shown in **Figure 6.9**. The figure demonstrates the recombination rate (R) behavior for the absorber layer with various defect densities under short-circuit conditions. In addition, the generation rate (G) is depicted to give a comparative figure. As expected, as the trap density increases, the recombination rate climbs dramatically, leading to poor performance.

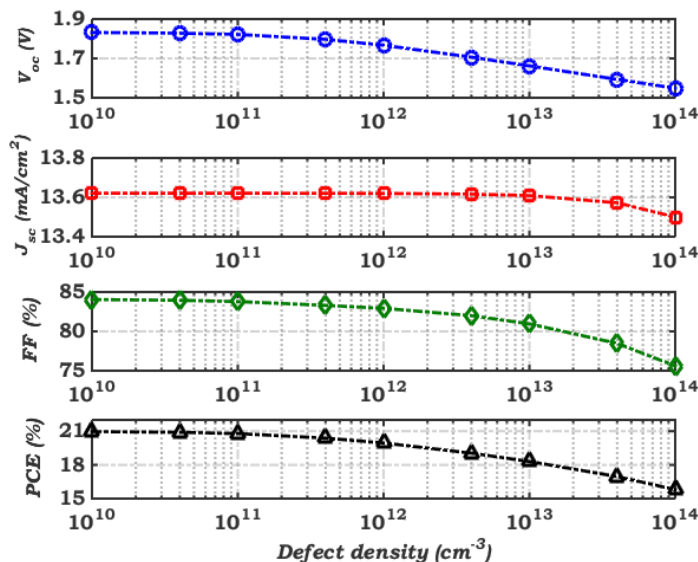


Figure 6.8 Variation in tandem performance parameters depending on the variation of the polymer absorber defect density.

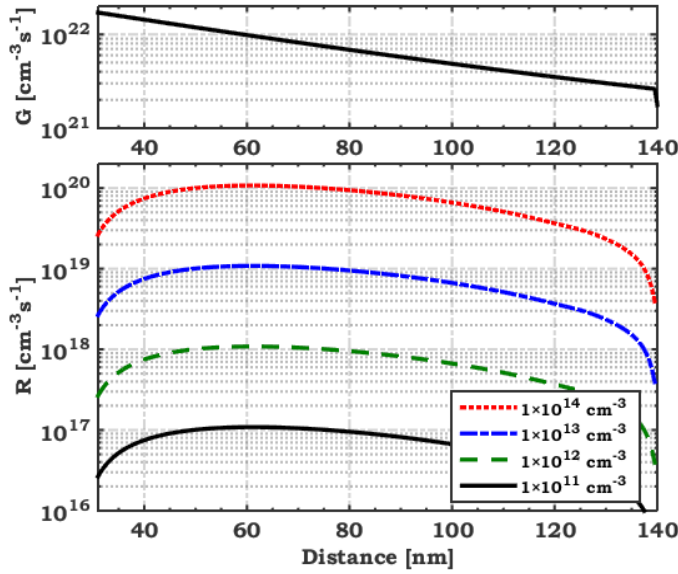


Figure 6.9 The generation and recombination rate behavior drawn at the illuminated short-circuit condition for the polymer absorber layer.

6.3.3 Thicknesses of The Absorber Layers

Figure 6.10 signifies the dependency of the tandem efficiency on the thickness of both absorber layers. We varied the top absorber thickness (t_{TA}) from 100 to 450 nm, while that of the bottom absorber (t_{BA}) was varied in the range (20 – 50 μm). As can be inferred from the figure, the PCE was unaffected by increasing t_{BA} from 30 to 50 μm and keeping t_{TA} below 175 nm. As t_{TA} falls lower than 150 nm, the PCE steadily reduces from 22.5% to 20%. In addition, changing t_{BA} from 20 to 50 μm does not affect PCE while keeping t_{TA} constant below 150 nm. The best tandem performance is achieved with $t_{TA} = 250$ nm and $t_{BA} = 40$ μm , providing the following PV parameters: $J_{sc} = 16.17$ mA/cm², $V_{oc} = 1.8$ V, FF = 82.59%, and PCE = 24%.

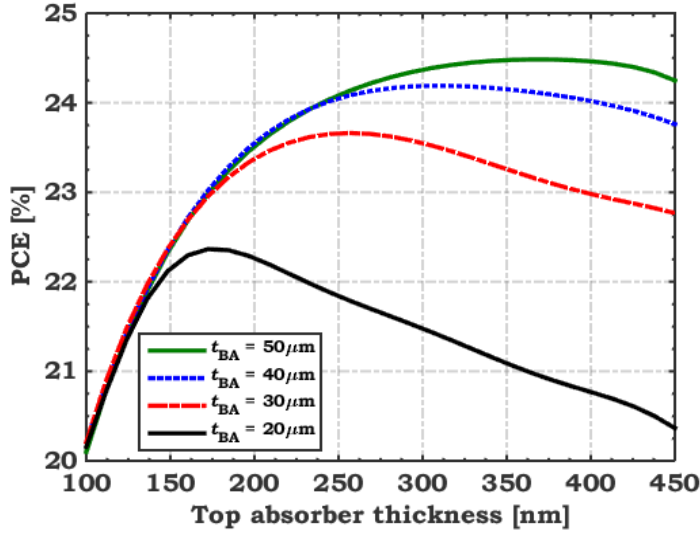


Figure 6.10 Tandem efficiency dependency on the thickness of the two absorber films.

6.3.4 Current Matching Point

In this subsection, we inspect for the current matching point (CMP) by changing t_{TA} from 200 to 340 nm while keeping t_{BA} fixed at 40 μm . **Figure 6.11(a)** depicts the J_{sc} dependence of the two sub-cells on t_{TA} . As expected, increasing the t_{TA} leads to more photon absorption and, thus, less transferred light to the rear cell. Therefore, increasing the t_{TA} increases the J_{sc} of the top cell and reduces that of the bottom cell, confirmed by the results in **Figure 6.11**. A CMP is obtained at $J_{sc} = 16.42 \text{ mA/cm}^2$ and $t_{TA} = 270 \text{ nm}$. The TSC has been simulated by applying this condition, and **Figure 6.11(b)** shows the illuminated J - V characteristics for both the TSC and its sub-cells. The maximum value of J_{sc} is 16.42 mA/cm^2 with $V_{oc} = 1.80 \text{ V}$ and $\text{PCE} = 24.21\%$ for the TSC. $V_{oc} = 1.80 \text{ V}$ equals the sum of the top cell (1.23 V) and bottom cell (0.57 V), demonstrating the efficient operation of the recombination junction. Moreover, the EQE of the TSC and its sub-cells at CMP is exhibited in **Figure 6.11(c)**. The EQE of the back c-Si sub-cell exceeds 85% at a wavelength of around 800 nm.

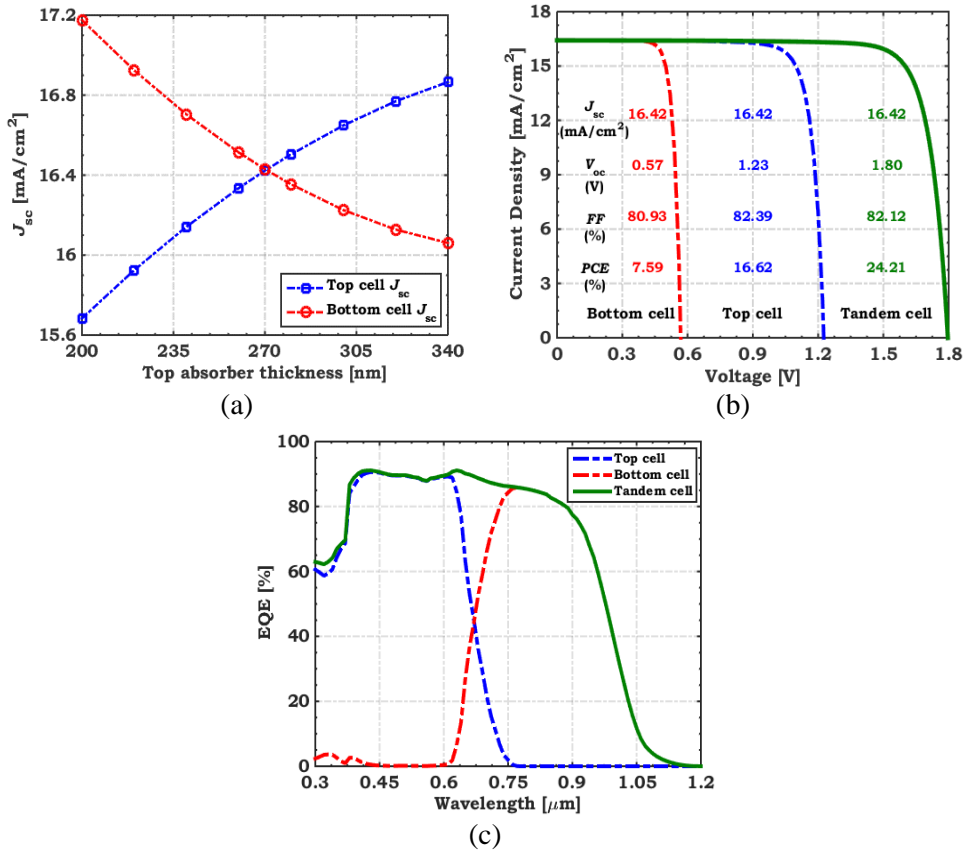


Figure 6.11 (a) J_{sc} dependence of the two sub-cells on the top absorber thickness (t_{TA}), (b) illuminated J - V and (c) EQE spectra of the polymer/Si TSC and its sub-cells under CMP.

6.4 Summary

This chapter presented a simulation study for a 2T thin-film tandem cell comprising of a polymer-based top sub-cell and a thin c-Si bottom sub-cell. The photoactive layer of the top sub-cell is a blend of PDTBTBz-2F as a polymer donor and PC₇₁BM as a fullerene acceptor. Initially, a calibration of the two sub-cells is carried out against experimental studies, providing a PCE of 10% for the top sub-cell and 14.26% for the bottom sub-cell. Upon incorporating into a tandem structure, the resulting cell shows a PCE of 16.58% and a J_{sc} of 13.39 mA/cm². Then, the tandem performance is optimized by controlling the VBO of the top cell. Furthermore, we inspected the influences of

the top absorber defect density as well as both absorber thicknesses for better tandem performance. After optimizing and designing the current matching point, the J_{sc} and PCE of the tandem cell are enhanced to 16.42 mA/cm^2 and 24.21%, respectively. These findings suggest that the proposed design can pave the way for flexible, environmentally friendly, and high-efficiency tandem cells.

This page is intentionally left blank

CHAPTER 7
CONCLUSIONS AND
FUTURE WORK

This page is intentionally left blank

CHAPTER 7

CONCLUSIONS AND FUTURE WORK

7.1 Conclusions

The performance of multi-junction solar cells surpasses single-junction cells due to their ability to utilize a broader spectrum. In this thesis, three novel monolithic multi-junction cells are proposed and investigated using TCAD numerical simulation. The investigated multi-junction cells are:

(i) A 2T monolithic all-BaSi₂ tandem solar cell (TSC) combines a BaSi₂ bottom sub-cell with a bandgap of 1.3 eV, and Ba(C_{0.78}Si_{0.22})₂ with a 1.8 eV bandgap. After optimizing the doping and the thickness of both absorber layers, and at the designed matching point, the current density, and the power conversion efficiency (PCE) of the TSC are enhanced up to 16.47 mA/cm² and 32.83%, respectively. Additionally, we have inspected the consequence of changing the absorbers defect density in the range (10¹² – 10¹⁸ cm⁻³) and the impact of the work functions of the contacts on the performance parameters of the TSC. It was found that contacts having a work function ≥ 4.5 eV for rear contact and ≤ 3.8 eV for front contact were adequate for better performance.

(ii) A 2T monolithic Sb₂S₃/Si tandem cell utilizes Sb₂S₃ having a 1.7 eV bandgap as a front cell, while thin c-Si with a 1.12 eV bandgap is incorporated as the bottom cell. The calibrated standalone top and bottom cells provide a PCE of 4.31% and 14.26%, respectively. Then, the Sb₂S₃ top cell is optimized by designing the cell without the organic hole transport layer (HTL) and tuning the conduction band offset (CBO) between the electron transport layer (ETL) and the Sb₂S₃ absorber.

Then, we optimize the TSC by inspecting the appropriate ETL thickness and doping concentration. Also, the impact of changing the absorber defect density and the series resistance of the top cell on the TSC performance is investigated to get the maximum available PCE. At defect density of $1 \times 10^{14} \text{ cm}^{-3}$ and ideal zero series resistance, the tandem efficiency is improved from 10.10% to 19.51%. Additionally, we have inspected the consequence of the top absorber thickness on TSC performance parameters for two cases of bottom absorber thickness (t_{Si}). At the designed matching point for each case, the optimum efficiency was achieved giving $J_{\text{sc}} = 17.24 \text{ mA/cm}^2$, and $\text{PCE} = 23.25\%$ for $t_{\text{Si}} = 30 \text{ }\mu\text{m}$, while $J_{\text{sc}} = 18.04 \text{ mA/cm}^2$, and $\text{PCE} = 24.34\%$ for $t_{\text{Si}} = 50 \text{ }\mu\text{m}$.

(iii) A 2T monolithic polymer/Si tandem cell comprises a polymer-based top sub-cell and a thin c-Si bottom sub-cell. The photoactive layer of the top sub-cell is a blend of PDTBTBz-2F as a polymer donor and PC₇₁BM as a fullerene acceptor. Initially, a calibration of the two sub-cells is carried out against experimental studies, providing a PCE of 10% for the top sub-cell and 14.26% for the bottom sub-cell. Then, we investigated the VBO impact of the front cell on the TSC performance. Furthermore, we inspected the influences of the top polymer defect density as well as both absorber thicknesses for optimum tandem performance. After optimizing the TSC and at the designed CMP, the J_{sc} and PCE of the tandem cell are enhanced to 16.42 mA/cm^2 and 24.21%, respectively.

Finally, we provide a comparison between our optimized TSCs and other tandem candidates, as shown in **Table 7.1**. Some of the reported tandem cells are based on experimental investigations, while others are computed numerically, as illustrated in the table. According to current experimental efforts, the efficiency of all Antimony Chalcogenide and Polymer/Si tandem cells has not exceeded the limit of 8% and 16%, respectively. Moreover, most of tandem

cells with lead-based perovskite top cell give higher efficiencies than our proposed thin film tandem cells; however, the toxicity of such tandems is a serious issue that limits their use and commercialization. For $\text{Sb}_2\text{S}_3/\text{Si}$ tandem cell, one of the main limitations is the high level of Sb_2S_3 bulk defects. This limitation has been investigated by many research studies [128–130]. It is also obvious from the high value of the series resistance that this is a serious limitation of the cell. However, by developing appropriate fabrication methods [45,107,115,116,131], both limitations can be alleviated to push the efficiency and thereby to enhance the overall performance of the tandem cells including Sb_2S_3 .

Table 7.1 A state-of-art comparison between performance parameters of our proposed tandem cells and state-of-the-art tandem cells stated in the literature.

Material	Method	J_{sc} (mA/cm^2)	V_{oc} (V)	FF (%)	PCE (%)	Ref.
Lead-based PVK/Si	Exp.	15.80	1.692	79.90	21.4	[132]
$\text{GaAs}_{0.75}\text{P}_{0.25}/\text{Si}$		17.34	1.732	77.70	23.4	[133]
Lead-based PVK/Si		18.14	1.753	78.50	25.0	[134]
$\text{Sb}_2\text{S}_3/\text{Sb}_2\text{Se}_3$		-	-	-	7.93*	[62]
Polymer/Si		15.81	1.08	55.57	8.32	[63]
Polymer/Si		-	-	-	15.25*	[63]
Lead-free PVK/Si	Sim.	16.01	1.76	86.7	24.4	[135]
Lead-based PVK/Si		18.81	2.01	83.61	31.67	[136]
$\text{Ba}(\text{C}_{0.75}\text{Si}_{0.25})_2/\text{Si}$		17.6	1.94	88.4	30.3	[58]
Lead-based PVK/CIGS		20.49	1.81	81.8	30.5	[137]
Polymer/Si		16.43	2.04	84.81	24.21	This work
$\text{Sb}_2\text{S}_3/\text{Si}$		18.04	1.64	82.41	24.34	
$\text{Ba}(\text{C}_{0.78}\text{Si}_{0.22})_2/\text{BaSi}_2$	16.48	2.27	91.45	34.25		

Sim. = simulation, Exp. = experiment, PVK = perovskite, *: it is a 4T tandem cell.

7.2 Future Work

The simulation studies provided in this thesis have revealed several photovoltaic materials that could be used as top and bottom sub-cells in a tandem cell, thereby improving the overall cell efficiency. The corresponding simulations have been validated against measurements to establish design guidelines

that can be used to suggest and recommend future experiments. These guidelines take into account practical constraints, which could potentially save time and cost in future experiments. Our future goal is to fabricate the proposed tandem structures. Despite the possibility of cost-prohibitive challenges depending on the availability of a process line, the physical construction and utilization of these structures in the real world would provide further validation to the simulation results and further solidify the proposed structures in this thesis. These structures have been designed to produce low-cost, environmentally friendly, and efficient thin film tandem solar cells that can be used in flexible applications.

Furthermore, in order for these tandem cells to become more competitive in the PV market, the construction of triple-junction cells is imperative. The careful selection of a third cell to tune up and exploit the entire solar spectrum can be achieved through the construction of a triple-junction cell, which will significantly boost their efficiencies to high levels. This will pave the way for the future development of highly efficient and cost-effective solar cells, which could have far-reaching implications for the renewable energy sector.

REFERENCES

This page is intentionally left blank

REFERENCES

- [1] A. Zekry, A road map for transformation from conventional to photovoltaic energy generation and its challenges, *J. King Saud Univ. Eng. Sci.* 32 (2020) 407–410. <https://doi.org/10.1016/j.jksues.2020.09.009>.
- [2] D.M. Chapin, C.S. Fuller, G.L. Pearson, A New Silicon *p-n* Junction Photocell for Converting Solar Radiation into Electrical Power, *J. Appl. Phys.* 25 (1954) 676–677. <https://doi.org/10.1063/1.1721711>.
- [3] A. Luque, S. Hegedus, *Handbook of Photovoltaic Science and Engineering*, Second Edition, Wiley, 2011. <https://doi.org/10.1002/9780470974704>.
- [4] A. Sahbel, N. Hassan, M.M. Abdelhameed, A. Zekry, Experimental performance characterization of photovoltaic modules using DAQ, *Energy Procedia.* 36 (2013) 323–332. <https://doi.org/10.1016/j.egypro.2013.07.037>.
- [5] M. Nakamura, K. Yamaguchi, Y. Kimoto, Y. Yasaki, T. Kato, H. Sugimoto, Cd-Free Cu(In,Ga)(Se,S)₂ thin-film solar cell with record efficiency of 23.35%, *IEEE J. Photovoltaics.* 9 (2019) 1863–1867. <https://doi.org/10.1109/JPHOTOV.2019.2937218>.
- [6] N. Qamhieh, A. Najjar, Z.N. Qamhieh, B. Abdel Aziz, A. Mansour, I. Alghoul, Synthesis and characterization of a perovskite film for solar cells applications, *Optik.* 171 (2018) 648–651. <https://doi.org/10.1016/j.ijleo.2018.05.066>.
- [7] M.S. Salem, A.J. Alzahrani, R.A. Ramadan, A. Alanazi, A. Shaker, M. Abouelatta, C. Gontrand, M. Elbanna, A. Zekry, Physically Based Analytical Model of Heavily Doped Silicon Wafers Based Proposed Solar Cell Microstructure, *IEEE Access.* 8 (2020) 138898–138906. <https://doi.org/10.1109/ACCESS.2020.3012657>.
- [8] M. Okil, M.S. Salem, T.M. Abdolkader, A. Shaker, From Crystalline to Low-cost Silicon-based Solar Cells : a Review, *Silicon.* 14 (2022) 1895–1911. <https://doi.org/10.1007/s12633-021-01032-4>.
- [9] R. Yasodharan, A. Senthilkumar, P. Mohankumar, J. Ajayan, R. Sivabalakrishnan, Investigation and influence of layer composition of tandem perovskite solar cells for applications in future renewable and sustainable energy, *Optik.* 212 (2020) 164723. <https://doi.org/10.1016/j.ijleo.2020.164723>.

- [10] M.M. Salah, A. Zekry, M. Abouelatta, A. Shaker, M. Mousa, F.Z. Amer, R.I. Mubarak, A. Saeed, High-Efficiency Electron Transport Layer-Free Perovskite/GeTe Tandem Solar Cell: Numerical Simulation, *Crystals*. 12 (2022) 878. <https://doi.org/10.3390/cryst12070878>.
- [11] J. Fricke, W.L. Borst, *Essentials of energy technology: sources, transport, storage, conservation*, Wiley, 2013.
- [12] B. Durão, J.P. N. Torres, C.A. F. Fernandes, R.A. Marques Lameirinhas, Socio-economic Study to Improve the Electrical Sustainability of the North Tower of Instituto Superior Técnico, *Sustainability*. 12 (2020) 1923. <https://doi.org/10.3390/su12051923>.
- [13] A. Zekry, A. Shaker, M. Salem, *Solar Cells and Arrays: Principles, Analysis, and Design*, in: *Adv. Renew. Energies Power Technol.*, Elsevier, 2018: pp. 3–56. <https://doi.org/10.1016/B978-0-12-812959-3.00001-0>.
- [14] S.M. Sze, K.K. Ng, *Physics of Semiconductor Devices*, Wiley, 2006. <https://doi.org/10.1002/0470068329>.
- [15] M. Petrović-Randelović, N. Kocić, B. Stojanović-Randelović, The importance of renewable energy sources for sustainable development, *Econ. Sustain. Dev.* 4 (2020) 15–24. <https://doi.org/10.5937/esd2002016p>.
- [16] R. Senthilkumar, S. Ramakrishnan, M. Balu, S.K. Batabyal, D.J. Yoo, D. Kumaresan, N.K. Kothurkar, $\text{Co}_x\text{Mo}_{(1-x)}\text{S}_2$ intermixed reduced graphene oxide as efficient counter electrode materials for high-performance dye-sensitized solar cells, *Int. J. Hydrogen Energy*. 48 (2023) 5901–5914. <https://doi.org/10.1016/j.ijhydene.2022.11.156>.
- [17] M.S. Salem, A. Shaker, M.M. Salah, Device Modeling of Efficient PBDB-T: PZT-Based All-Polymer Solar Cell: Role of Band Alignment, *Polymers*. 15 (2023) 869.
- [18] M. Okil, A. Shaker, I.S. Ahmed, T.M. Abdolkader, M.S. Salem, Evaluation of a proposed barium di-silicide tandem solar cell using TCAD numerical simulation, *Opt. Quantum Electron.* 55 (2023) 475. <https://doi.org/10.1007/s11082-023-04734-8>.
- [19] T.I. Alanazi, M. El Sabbagh, Proposal and Design of Flexible All-Polymer/CIGS Tandem Solar Cell, *Polymers*. 15 (2023) 1823. <https://doi.org/10.3390/polym15081823>.

- [20] M.S. Salem, A. Shaker, M. Abouelatta, A. Saeed, Full Optoelectronic Simulation of Lead-Free Perovskite/Organic Tandem Solar Cells, *Polymers*. 15 (2023) 784.
- [21] X. Li, H. Zhu, K. Wang, A. Cao, J. Wei, C. Li, Y. Jia, Z. Li, X. Li, D. Wu, Graphene-On-Silicon Schottky Junction Solar Cells, *Adv. Mater.* 22 (2010) 2743–2748. <https://doi.org/10.1002/adma.200904383>.
- [22] S. Das, D. Pandey, J. Thomas, T. Roy, The Role of Graphene and Other 2D Materials in Solar Photovoltaics, *Adv. Mater.* 31 (2019) 1802722. <https://doi.org/10.1002/adma.201802722>.
- [23] M.A. Green, E.D. Dunlop, G. Siefer, M. Yoshita, N. Kopidakis, K. Bothe, X. Hao, Solar cell efficiency tables (Version 61), *Prog. Photovoltaics Res. Appl.* 31 (2023) 3–16. <https://doi.org/10.1002/PIP.3646>.
- [24] M.C. Putnam, S.W. Boettcher, M.D. Kelzenberg, D.B. Turner-Evans, J.M. Spurgeon, E.L. Warren, R.M. Briggs, N.S. Lewis, H.A. Atwater, Si microwire-array solar cells, *Energy Environ. Sci.* 3 (2010) 1037–1041. <https://doi.org/10.1039/c0ee00014k>.
- [25] M.S. Salem, A. Zekry, A. Shaker, M. Abouelatta, Design and simulation of proposed low cost solar cell structures based on heavily doped silicon wafers, in: *Conf. Rec. IEEE Photovolt. Spec. Conf.*, 2016: pp. 2393–2397. <https://doi.org/10.1109/PVSC.2016.7750070>.
- [26] M.S. Salem, A.J. Alzahrani, R.A. Ramadan, A. Alanazi, A. Shaker, M. Abouelatta, C. Gontrand, M. Elbanna, A. Zekry, Physically Based Analytical Model of Heavily Doped Silicon Wafers Based Proposed Solar Cell Microstructure, *IEEE Access*. 8 (2020) 138898–138906. <https://doi.org/10.1109/ACCESS.2020.3012657>.
- [27] M. Salem, A. Zekry, M. Abouelatta, M.T. Alshammari, A. Alanazi, K.A. Al-Dhlan, A. Shaker, Influence of base doping level on the npn microstructure solar cell performance: A TCAD study, *Opt. Mater.* 121 (2021) 111501. <https://doi.org/10.1016/j.optmat.2021.111501>.
- [28] G. Kim, G. Kim, J.W. Lim, J.W. Lim, J. Kim, J. Kim, S.J. Yun, S.J. Yun, M.A. Park, Transparent Thin-Film Silicon Solar Cells for Indoor Light Harvesting with Conversion Efficiencies of 36% without Photodegradation, *ACS Appl. Mater. Interfaces*. 12 (2020) 27122–27130. <https://doi.org/10.1021/acsami.0c04517>.
- [29] P. Gao, M. Grätzel, M.K. Nazeeruddin, Organohalide lead perovskites

- for photovoltaic applications, *Energy Environ. Sci.* 7 (2014) 2448–2463. <https://doi.org/10.1039/c4ee00942h>.
- [30] A. Kojima, K. Teshima, Y. Shirai, T. Miyasaka, Organometal halide perovskites as visible-light sensitizers for photovoltaic cells, *J. Am. Chem. Soc.* 131 (2009) 6050–6051. <https://doi.org/10.1021/ja809598r>.
- [31] W.S. Yang, B.W. Park, E.H. Jung, N.J. Jeon, Y.C. Kim, D.U. Lee, S.S. Shin, J. Seo, E.K. Kim, J.H. Noh, S. Il Seok, Iodide management in formamidinium-lead-halide-based perovskite layers for efficient solar cells, *Science* (80). 356 (2017) 1376–1379. <https://doi.org/10.1126/science.aan2301>.
- [32] M.M. Salah, M. Abouelatta, A. Shaker, K.M. Hassan, A. Saeed, A Comprehensive Simulation Study of Hybrid Halide Perovskite Solar Cell with Copper Oxide as HTM, *Semicond. Sci. Technol.* 34 (2019) 115009.
- [33] R. Singh, P.K. Singh, B. Bhattacharya, H.W. Rhee, Review of current progress in inorganic hole-transport materials for perovskite solar cells, *Appl. Mater. Today.* 14 (2019) 175–200. <https://doi.org/10.1016/j.apmt.2018.12.011>.
- [34] T. Suemasu, N. Usami, Exploring the potential of semiconducting BaSi₂ for thin-film solar cell applications, *J. Phys. D. Appl. Phys.* 50 (2017) 023001. <https://doi.org/10.1088/1361-6463/50/2/023001>.
- [35] K. Toh, T. Saito, T. Suemasu, Optical absorption properties of BaSi₂ epitaxial films grown on a transparent silicon-on-insulator substrate using molecular beam epitaxy, *Jpn. J. Appl. Phys.* 50 (2011) 068001. <https://doi.org/10.1143/JJAP.50.068001>.
- [36] M.A. Khan, T. Saito, K. Nakamura, M. Baba, W. Du, K. Toh, K. Toko, T. Suemasu, Electrical characterization and conduction mechanism of impurity-doped BaSi₂ films grown on Si(111) by molecular beam epitaxy, in: *Thin Solid Films*, 2012: pp. 95–99. <https://doi.org/10.1016/j.tsf.2012.09.005>.
- [37] M. Baba, K. Toh, K. Toko, N. Saito, N. Yoshizawa, K. Jiptner, T. Sekiguchi, K.O. Hara, N. Usami, T. Suemasu, Investigation of grain boundaries in BaSi₂ epitaxial films on Si(111) substrates using transmission electron microscopy and electron-beam-induced current technique, *J. Cryst. Growth.* 348 (2012) 75–79. <https://doi.org/10.1016/j.jcrysgr.2012.03.044>.

- [38] K.O. Hara, N. Usami, K. Nakamura, R. Takabe, M. Baba, K. Toko, T. Suemasu, Determination of bulk minority-carrier lifetime in BaSi₂ earth-abundant absorber films by utilizing a drastic enhancement of carrier lifetime by post-growth annealing, *Appl. Phys. Express.* 6 (2013) 112302. <https://doi.org/10.7567/APEX.6.112302>.
- [39] K. Takahashi, Y. Nakagawa, K.O. Hara, Y. Kurokawa, N. Usami, Investigation of p-type emitter layer materials for heterojunction barium disilicide thin film solar cells, *Jpn. J. Appl. Phys.* 56 (2017). <https://doi.org/10.7567/JJAP.56.05DB04>.
- [40] Y. Tian, R. Vismara, S. Van Doorene, P. Šutta, L. Vančo, M. Veselý, P. Vogrinčič, O. Isabella, M. Zeman, Oxidation-Induced Structure Transformation: Thin-Film Synthesis and Interface Investigations of Barium Disilicide toward Potential Photovoltaic Applications, *ACS Appl. Energy Mater.* 1 (2018) 3267–3276. <https://doi.org/10.1021/acsaem.8b00486>.
- [41] Y. Tian, A.R. Bento Montes, L. Vančo, M. Čaplovičová, P. Vogrinčič, P. Šutta, L. Satrapinsky, M. Zeman, O. Isabella, Toward BaSi₂/Si Heterojunction Thin-Film Solar Cells: Insights into Heterointerface Investigation, Barium Depletion, and Silicide-Mediated Silicon Crystallization, *Adv. Mater. Interfaces.* 7 (2020) 1–11. <https://doi.org/10.1002/admi.202000887>.
- [42] K. Morita, M. Kobayashi, T. Suemasu, Effects of Sr addition on crystallinity and optical absorption edges in ternary semiconducting silicide Ba_{1-x}Sr_xSi₂, *Thin Solid Films.* 515 (2007) 8216–8218. <https://doi.org/10.1016/j.tsf.2007.02.047>.
- [43] Y. Imai, A. Watanabe, Assessment of the possibility of band gap widening of BaSi₂ by incorporation of carbon, *Intermetallics.* 18 (2010) 1432–1436. <https://doi.org/10.1016/j.intermet.2010.03.019>.
- [44] H. Deng, Y. Zeng, M. Ishaq, S. Yuan, H. Zhang, X. Yang, M. Hou, U. Farooq, J. Huang, K. Sun, R. Webster, H. Wu, Z. Chen, F. Yi, H. Song, X. Hao, J. Tang, Quasiepitaxy Strategy for Efficient Full-Inorganic Sb₂S₃ Solar Cells, *Adv. Funct. Mater.* 29 (2019). <https://doi.org/10.1002/adfm.201901720>.
- [45] Y.C. Choi, D.U. Lee, J.H. Noh, E.K. Kim, S. Il Seok, Highly improved Sb₂S₃ sensitized-inorganic-organic heterojunction solar cells and quantification of traps by deep-level transient spectroscopy, *Adv.*

- Funct. Mater. 24 (2014) 3587–3592. <https://doi.org/10.1002/adfm.201304238>.
- [46] D.H. Kim, S.J. Lee, M.S. Park, J.K. Kang, J.H. Heo, S.H. Im, S.J. Sung, Highly reproducible planar Sb₂S₃-sensitized solar cells based on atomic layer deposition, *Nanoscale*. 6 (2014) 14549–14554. <https://doi.org/10.1039/c4nr04148h>.
- [47] M.A. Green, Silicon wafer-based tandem cells: The ultimate photovoltaic solution?, in: *Physics, Simulation, Photonic Eng. Photovolt. Devices III*, SPIE, 2014: p. 89810L. <https://doi.org/10.1117/12.2044175>.
- [48] A.J. Heeger, 25th anniversary article: Bulk heterojunction solar cells: Understanding the mechanism of operation, *Adv. Mater.* 26 (2014) 10–28. <https://doi.org/10.1002/adma.201304373>.
- [49] S.B. Ambade, R.B. Ambade, S. Kim, H. Park, D.J. Yoo, S.H. Lee, Performance enhancement in inverted solar cells by interfacial modification of ZnO nanoparticle buffer layer, *J. Nanosci. Nanotechnol.* 14 (2014) 8561–8566. <https://doi.org/10.1166/jnn.2014.9996>.
- [50] Y. Yan, F. Cai, L. Yang, J. Li, Y. Zhang, F. Qin, C. Xiong, Y. Zhou, D.G. Lidzey, T. Wang, Light-Soaking-Free Inverted Polymer Solar Cells with an Efficiency of 10.5% by Compositional and Surface Modifications to a Low-Temperature-Processed TiO₂ Electron-Transport Layer, *Adv. Mater.* 29 (2017) 1604044. <https://doi.org/10.1002/adma.201604044>.
- [51] W. Shockley, H.J. Queisser, Detailed balance limit of efficiency of p-n junction solar cells, *J. Appl. Phys.* 32 (1961) 510–519. <https://doi.org/10.1063/1.1736034>.
- [52] A. De Vos, Detailed balance limit of the efficiency of tandem solar cells, *J. Phys. D. Appl. Phys.* 13 (1980) 839–846. <https://doi.org/10.1088/0022-3727/13/5/018>.
- [53] J. Sun, J. Wu, X. Tong, F. Lin, Y. Wang, Z.M. Wang, Organic/Inorganic Metal Halide Perovskite Optoelectronic Devices beyond Solar Cells, *Adv. Sci.* 5 (2018) 1700780. <https://doi.org/10.1002/advs.201700780>.
- [54] M. Fillali, B. Dennai, Impact of tunnel heterojunction (INGaP/GaA) doping concentration on the performance of INGaP/GaAS tandem solar

- cell using silvaco-atlas software, *J. Ovonic Res.* 15 (2019) 279–285.
- [55] H. Shen, S.T. Omelchenko, D.A. Jacobs, S. Yalamanchili, Y. Wan, D. Yan, P. Phang, T. Duong, Y. Wu, Y. Yin, C. Samundsett, J. Peng, N. Wu, T.P. White, G.G. Andersson, N.S. Lewis, K.R. Catchpole, In situ recombination junction between *p*-Si and TiO₂ enables high-efficiency monolithic perovskite/Si tandem cells, *Sci. Adv.* 4 (2018). <https://doi.org/10.1126/sciadv.aau9711>.
- [56] L. Wang, J. He, X. Shang, M. Li, Y. Yu, G. Zha, H. Ni, Z. Niu, Enhanced tunneling in the GaAs p⁺-n⁺ junction by embedding InAs quantum dots, *Semicond. Sci. Technol.* 27 (2012). <https://doi.org/10.1088/0268-1242/27/11/115010>.
- [57] R. Vismara, O. Isabella, M. Zeman, Organometallic halide perovskite/barium di-silicide thin-film double-junction solar cells, *Photonics Sol. Energy Syst.* VI. 9898 (2016) 98980J. <https://doi.org/10.1117/12.2227174>.
- [58] D. Tianguo, Carrier transport properties in BaSi₂ and structure design of BaSi₂ solar cells, PhD diss., University of Tsukuba, 2019.
- [59] R. Kondrotas, C. Chen, J. Tang, Sb₂S₃ Solar Cells, *Joule.* 2 (2018) 857–878. <https://doi.org/10.1016/j.joule.2018.04.003>.
- [60] S. Lu, C. Chen, J. Tang, Possible top cells for next-generation Si-based tandem solar cells, *Front. Optoelectron.* 13 (2020) 246–255. <https://doi.org/10.1007/s12200-020-1050-y>.
- [61] C. Gao, M. Xu, B.K. Ng, L. Kang, L. Jiang, Y. Lai, F. Liu, In situ growth of Sb₂S₃ thin films by reactive sputtering on n-Si(100) substrates for top sub-cell of silicon based tandem solar cells, *Mater. Lett.* 195 (2017) 186–189. <https://doi.org/10.1016/j.matlet.2017.02.046>.
- [62] J. Zhang, W. Lian, Y. Yin, X. Wang, R. Tang, C. Qian, X. Hao, C. Zhu, T. Chen, All Antimony Chalcogenide Tandem Solar Cell, *Sol. RRL.* 4 (2020) 1–6. <https://doi.org/10.1002/solr.202000048>.
- [63] H.J. Park, S.H. Park, S.W. Lee, Y. Kang, D. Kim, H.J. Son, H.S. Lee, Novel Polymer-Based Organic/c-Si Monolithic Tandem Solar Cell: Enhanced Efficiency using Interlayer and Transparent Top Electrode Engineering, *Macromol. Rapid Commun.* 42 (2021) 1–9. <https://doi.org/10.1002/marc.202100305>.
- [64] Atlas User's Manual, Silvaco Inc., Santa Clara, USA, (n.d.).

- https://silvaco.com/products/tcad/device_simulation/atlas/atlas.html
(accessed June 1, 2022).
- [65] R. Pandey, A. Singla, J. Madan, R. Sharma, R. Chaujar, Toward the design of monolithic 23.1% efficient hysteresis and moisture free perovskite/c-Si HJ tandem solar cell: a numerical simulation study, *J. Micromechanics Microengineering*. 29 (2019) 64001.
- [66] X. Huang, J. Long, D. Wu, S. Ye, X. Li, Q. Sun, Z. Xing, W. Yang, M. Song, Y. Guo, others, Flexible four-junction inverted metamorphic AlGaInP/AlGaAs/In_{0.17}Ga_{0.83}As/In_{0.47}Ga_{0.53}As solar cell, *Sol. Energy Mater. Sol. Cells*. 208 (2020) 110398.
- [67] W. Yoon, D. Scheiman, Y.W. Ok, Z. Song, C. Chen, G. Jernigan, A. Rohatgi, Y. Yan, P. Jenkins, Sputtered indium tin oxide as a recombination layer formed on the tunnel oxide/poly-Si passivating contact enabling the potential of efficient monolithic perovskite/Si tandem solar cells, *Sol. Energy Mater. Sol. Cells*. 210 (2020) 110482. <https://doi.org/10.1016/j.solmat.2020.110482>.
- [68] X. Chen, Z. Jia, Z. Chen, T. Jiang, L. Bai, F. Tao, J. Chen, X. Chen, T. Liu, X. Xu, C. Yang, W. Shen, W.E.I. Sha, H. Zhu, Y. (Michael) Yang, Efficient and Reproducible Monolithic Perovskite/Organic Tandem Solar Cells with Low-Loss Interconnecting Layers, *Joule*. 4 (2020) 1594–1606. <https://doi.org/10.1016/j.joule.2020.06.006>.
- [69] K.O. Brinkmann, T. Becker, F. Zimmermann, C. Kreuzel, T. Gahlmann, M. Theisen, T. Haeger, S. Olthof, C. Tückmantel, M. Günster, T. Maschwitz, F. Göbelsmann, C. Koch, D. Hertel, P. Caprioglio, F. Peña-Camargo, L. Perdigón-Toro, A. Al-Ashouri, L. Merten, A. Hinderhofer, L. Gomell, S. Zhang, F. Schreiber, S. Albrecht, K. Meerholz, D. Neher, M. Stollerfoht, T. Riedl, Perovskite–organic tandem solar cells with indium oxide interconnect, *Nature*. 604 (2022) 280–286. <https://doi.org/10.1038/s41586-022-04455-0>.
- [70] S. Kashyap, R. Pandey, J. Madan, R. Sharma, Design and Simulation of a-Si:H/PbS Colloidal Quantum Dots Monolithic Tandem Solar Cell for 12% Efficiency, *Phys. Status Solidi*. 217 (2020) 2000252. <https://doi.org/10.1002/pssa.202000252>.
- [71] M. Zeman, J. Krc, Optical and electrical modeling of thin-film silicon solar cells, *J. Mater. Res*. 23 (2008) 889–898. <https://doi.org/10.1557/jmr.2008.0125>.

- [72] H. Yu, S. Ji, X. Luo, Q. Xie, Technology CAD (TCAD) simulations of Mg₂Si/Si heterojunction photodetector based on the thickness effect, *Sensors*. 21 (2021). <https://doi.org/10.3390/s21165559>.
- [73] H. Yu, C. Gao, J. Zou, W. Yang, Q. Xie, Simulation study on the effect of doping concentrations on the photodetection properties of Mg₂Si/Si heterojunction photodetector, *Photonics*. 8 (2021). <https://doi.org/10.3390/photonics8110509>.
- [74] K.O. Hara, N. Usami, K. Toh, M. Baba, K. Toko, T. Suemasu, Investigation of the recombination mechanism of excess carriers in undoped BaSi₂ films on silicon, *J. Appl. Phys.* 112 (2012) 083108. <https://doi.org/10.1063/1.4759246>.
- [75] R. Takabe, K.O. Hara, M. Baba, W. Du, N. Shimada, K. Toko, N. Usami, T. Suemasu, Influence of grain size and surface condition on minority-carrier lifetime in undoped *n*-BaSi₂ on Si(111), *J. Appl. Phys.* 115 (2014) 193510. <https://doi.org/10.1063/1.4878159>.
- [76] T. Deng, T. Suemasu, D.A. Shohonov, I.S. Samusevich, A.B. Filonov, D.B. Migas, V.E. Borisenko, Transport properties of *n*- and *p*-type polycrystalline BaSi₂, *Thin Solid Films*. 661 (2018) 7–15. <https://doi.org/10.1016/j.tsf.2018.07.006>.
- [77] S. Yachi, R. Takabe, K. Toko, T. Suemasu, Effect of *p*-BaSi₂ layer thickness on the solar cell performance of *p*-BaSi₂/*n*-Si heterojunction solar cells, *Jpn. J. Appl. Phys.* 56 (2017). <https://doi.org/10.7567/JJAP.56.05DB03>.
- [78] T. Deng, Z. Xu, Y. Yamashita, T. Sato, K. Toko, T. Suemasu, Modeling the effects of defect parameters on the performance of a *p*-BaSi₂/*n*-Si heterojunction solar cell, *Sol. Energy Mater. Sol. Cells*. 205 (2020) 110244. <https://doi.org/10.1016/j.solmat.2019.110244>.
- [79] M.A. Green, Improved silicon optical parameters at 25°C, 295 K and 300 K including temperature coefficients, *Prog. Photovoltaics Res. Appl.* 30 (2022) 164–179. <https://doi.org/10.1002/pip.3474>.
- [80] K. Kodama, R. Takabe, T. Deng, K. Toko, T. Suemasu, Spectroscopic evidence of photogenerated carrier separation by built-in electric field in Sb-doped *n*-BaSi₂/B-doped *p*-BaSi₂ homojunction diodes, *Jpn. J. Appl. Phys.* 57 (2018) 050310. <https://doi.org/10.7567/JJAP.57.050310>.
- [81] G.E. Eperon, M.T. Hörantner, H.J. Snaith, Metal halide perovskite

- tandem and multiple-junction photovoltaics, *Nat. Rev. Chem.* 1 (2017). <https://doi.org/10.1038/S41570-017-0095>.
- [82] B.M. Soucase, I. Guaita Pradas, K.R. Adhikari, Numerical Simulations on Perovskite Photovoltaic Devices, in: *Perovskite Mater. Synth. Characterisation, Prop. Appl.*, InTech, 2016. <https://doi.org/10.5772/61751>.
- [83] F. Anwar, S. Afrin, S.S. Satter, R. Mahbub, S.M. Ullah, Simulation and performance study of nanowire CdS/CdTe solar cell, *Int. J. Renew. Energy Res.* 7 (2017) 885–893.
- [84] H. Liao, Q. Deng, Y. Shen, G. Wang, S. Wang, Y. Mao, Theoretical analysis of doping concentration, layer thickness and barrier height effects on BaSi₂ based homojunction solar cells toward high efficiency, *Sol. Energy.* 201 (2020) 857–865. <https://doi.org/10.1016/j.solener.2020.03.056>.
- [85] P. Sawicka-Chudy, Z. Starowicz, G. Wisz, R. Yavorskyi, Z. Zapukhlyak, M. Bester, GŁowa, M. Sibiński, M. Cholewa, Simulation of TiO₂/CuO solar cells with SCAPS-1D software, *Mater. Res. Express.* 6 (2019). <https://doi.org/10.1088/2053-1591/ab22aa>.
- [86] M.S. Salem, A. Shaker, M.S. Othman, A.H. Al-Bagawia, M. Fedawy, G.M. Aleid, Numerical analysis and design of high performance HTL-free antimony sulfide solar cells by SCAPS-1D, *Opt. Mater.* 123 (2022). <https://doi.org/10.1016/j.optmat.2021.111880>.
- [87] G.N. Derry, M.E. Kern, E.H. Worth, Recommended values of clean metal surface work functions, *J. Vac. Sci. Technol. A Vacuum, Surfaces, Film.* 33 (2015) 060801. <https://doi.org/10.1116/1.4934685>.
- [88] D.U. Lee, S. Woo Pak, S. Gook Cho, E. Kyu Kim, S. Il Seok, Defect states in hybrid solar cells consisting of Sb₂S₃ quantum dots and TiO₂ nanoparticles, *Appl. Phys. Lett.* 103 (2013) 023901. <https://doi.org/10.1063/1.4813272>.
- [89] P. Myagmarsereejid, M. Ingram, M. Batmunkh, Y.L. Zhong, Doping Strategies in Sb₂S₃ Thin Films for Solar Cells, *Small.* 17 (2021) 2100241. <https://doi.org/10.1002/sml.202100241>.
- [90] X. Wang, J. Li, W. Liu, S. Yang, C. Zhu, T. Chen, A fast chemical approach towards Sb₂S₃ film with a large grain size for high-performance planar heterojunction solar cells, *Nanoscale.* 9 (2017) 3386–3390. <https://doi.org/10.1039/c7nr00154a>.

- [91] M.S. Salem, A. Shaker, A. Zekry, M. Abouelatta, A. Alanazi, M.T. Alshammari, C. Gontand, Analysis of hybrid hetero-homo junction lead-free perovskite solar cells by scaps simulator, *Energies*. 14 (2021) 5741. <https://doi.org/10.3390/en14185741>.
- [92] N. Gamal, S.H. Sedky, A. Shaker, M. Fedawy, Design of lead-free perovskite solar cell using $Zn_{1-x}Mg_xO$ as ETL: SCAPS device simulation, *Optik*. 242 (2021) 167306. <https://doi.org/10.1016/j.ijleo.2021.167306>.
- [93] S. Yuan, H. Deng, D. Dong, X. Yang, K. Qiao, C. Hu, H. Song, H. Song, Z. He, J. Tang, Efficient planar antimony sulfide thin film photovoltaics with large grain and preferential growth, *Sol. Energy Mater. Sol. Cells*. 157 (2016) 887–893. <https://doi.org/10.1016/j.solmat.2016.07.050>.
- [94] H. Chen, Z.Q. Li, B. Sun, X.D. Feng, Towards high-efficiency planar heterojunction antimony sulfide solar cells, *Opt. Mater.* 121 (2021) 111556. <https://doi.org/10.1016/j.optmat.2021.111556>.
- [95] M.S. Salem, A. Shaker, M.S. Othman, A.H. Al-Bagawia, M. Fedawy, G.M. Aleid, Numerical analysis and design of high performance HTL-free antimony sulfide solar cells by SCAPS-1D, *Opt. Mater.* 123 (2022) 111880. <https://doi.org/10.1016/j.optmat.2021.111880>.
- [96] T. Deng, Z. Xu, Y. Yamashita, T. Sato, K. Toko, T. Suemasu, Modeling the effects of defect parameters on the performance of a p -BaSi₂/ n -Si heterojunction solar cell, *Sol. Energy Mater. Sol. Cells*. 205 (2020). <https://doi.org/10.1016/j.solmat.2019.110244>.
- [97] I. Hwang, Y. Jeong, Y. Shiratori, J. Park, S. Miyajima, I. Yoon, K. Seo, Effective Photon Management of Non-Surface-Textured Flexible Thin Crystalline Silicon Solar Cells, *Cell Reports Phys. Sci.* 1 (2020) 100242. <https://doi.org/10.1016/j.xcrp.2020.100242>.
- [98] A.R. Jeong, S. Bin Choi, W.M. Kim, J.K. Park, J. Choi, I. Kim, J.H. Jeong, Electrical analysis of c -Si/CGSe monolithic tandem solar cells by using a cell-selective light absorption scheme, *Sci. Rep.* 7 (2017) 1–11. <https://doi.org/10.1038/s41598-017-15998-y>.
- [99] I. Gharibshahian, S. Sharbati, A.A. Orouji, Design of $CuIn_{1-y}Ga_ySe_2/Si_{1-x}Ge_x$ Tandem solar cells with controlled current matching, *IET Optoelectron.* 14 (2020) 199–209. <https://doi.org/10.1049/iet-opt.2019.0060>.

- [100] C. Chen, J. Tang, Open-Circuit Voltage Loss of Antimony Chalcogenide Solar Cells: Status, Origin, and Possible Solutions, *ACS Energy Lett.* 5 (2020) 2294–2304. <https://doi.org/10.1021/acsenergylett.0c00940>.
- [101] C.E. Patrick, F. Giustino, Structural and electronic properties of semiconductor-sensitized solar-cell interfaces, *Adv. Funct. Mater.* 21 (2011) 4663–4667. <https://doi.org/10.1002/adfm.201101103>.
- [102] P. Qin, S. Tanaka, S. Ito, N. Tetreault, K. Manabe, H. Nishino, M.K. Nazeeruddin, M. Grätzel, Inorganic hole conductor-based lead halide perovskite solar cells with 12.4% conversion efficiency, *Nat. Commun.* 5 (2014). <https://doi.org/10.1038/ncomms4834>.
- [103] J. Xiang, Y. Li, F. Huang, D. Zhong, Effect of interfacial recombination, bulk recombination and carrier mobility on the: J-V hysteresis behaviors of perovskite solar cells: A drift-diffusion simulation study, *Phys. Chem. Chem. Phys.* 21 (2019) 17836–17845. <https://doi.org/10.1039/c9cp03548f>.
- [104] T. Minemoto, M. Murata, Theoretical analysis on effect of band offsets in perovskite solar cells, *Sol. Energy Mater. Sol. Cells.* 133 (2015) 8–14. <https://doi.org/10.1016/j.solmat.2014.10.036>.
- [105] R. Scheer, H.W. Schock, *Chalcogenide Photovoltaics: Physics, Technologies, and Thin Film Devices*, John Wiley & Sons, 2011. <https://doi.org/10.1002/9783527633708>.
- [106] C. Chen, X. Liu, K. Li, S. Lu, S. Wang, S. Li, Y. Lu, J. He, J. Zheng, X. Lin, J. Tang, High-efficient Sb₂Se₃ solar cell using Zn_xCd_{1-x}S *n*-type layer, *Appl. Phys. Lett.* 118 (2021) 172103. <https://doi.org/10.1063/5.0030430>.
- [107] Y. Zhao, C. Li, J. Niu, Z. Zhi, G. Chen, J. Gong, J. Li, X. Xiao, Zinc-based electron transport materials for over 9.6%-efficient S-rich Sb₂(S,Se)₃ solar cells, *J. Mater. Chem. A.* 9 (2021) 12644–12651. <https://doi.org/10.1039/d1ta02356j>.
- [108] Y. Zhou, Y. Li, J. Luo, D. Li, X. Liu, C. Chen, H. Song, J. Ma, D.J. Xue, B. Yang, J. Tang, Buried homojunction in CdS/Sb₂Se₃ thin film photovoltaics generated by interfacial diffusion, *Appl. Phys. Lett.* 111 (2017) 013901. <https://doi.org/10.1063/1.4991539>.
- [109] I. Gharibshahian, A.A. Orouji, S. Sharbati, Efficient Sb₂(S,Se)₃/Zn(O,S) solar cells with high open-circuit voltage by

- controlling sulfur content in the absorber-buffer layers, *Sol. Energy*. 227 (2021) 606–615. <https://doi.org/10.1016/j.solener.2021.09.039>.
- [110] L.Y. Lin, Y. Qiu, Y. Zhang, H. Zhang, Analysis of effect of Zn(O,S) buffer layer properties on CZTS solar cell performance using AMPS, *Chinese Phys. Lett.* 33 (2016). <https://doi.org/10.1088/0256-307X/33/10/107801>.
- [111] K. Tanaka, T. Minemoto, H. Takakura, Analysis of heterointerface recombination by Zn_{1-x}Mg_xO for window layer of Cu(In,Ga)Se₂ solar cells, *Sol. Energy*. 83 (2009) 477–479. <https://doi.org/10.1016/j.solener.2008.09.003>.
- [112] R. Kondrotas, C. Chen, J. Tang, Sb₂S₃ Solar Cells, *Joule*. 2 (2018) 857–878. <https://doi.org/10.1016/j.joule.2018.04.003>.
- [113] M.A. Green, Accurate expressions for solar cell fill factors including series and shunt resistances, *Appl. Phys. Lett.* 108 (2016) 081111. <https://doi.org/10.1063/1.4942660>.
- [114] U. Wurfel, A. Cuevas, P. Wurfel, Charge carrier separation in solar cells, *IEEE J. Photovoltaics*. 5 (2015) 461–469. <https://doi.org/10.1109/JPHOTOV.2014.2363550>.
- [115] H. Deng, Y. Zeng, M. Ishaq, S. Yuan, H. Zhang, X. Yang, M. Hou, U. Farooq, J. Huang, K. Sun, R. Webster, H. Wu, Z. Chen, F. Yi, H. Song, X. Hao, J. Tang, Quasiepitaxy Strategy for Efficient Full-Inorganic Sb₂S₃ Solar Cells, *Adv. Funct. Mater.* 29 (2019). <https://doi.org/10.1002/adfm.201901720>.
- [116] L. Zhang, W. Lian, X. Zhao, Y. Yin, T. Chen, C. Zhu, Sb₂S₃ Seed-Mediated Growth of Low-Defect Sb₂S₃ on a TiO₂ Substrate for Efficient Solar Cells, *ACS Appl. Energy Mater.* 3 (2020) 12417–12422. <https://doi.org/10.1021/acsaem.0c02400>.
- [117] J. Dong, Y. Liu, Z. Wang, Y. Zhang, Boosting V_{OC} of antimony chalcogenide solar cells: A review on interfaces and defects, *Nano Sel.* 2 (2021) 1818–1848. <https://doi.org/10.1002/nano.202000288>.
- [118] I. Hwang, H.D. Um, B.S. Kim, M. Wober, K. Seo, Flexible crystalline silicon radial junction photovoltaics with vertically aligned tapered microwires, *Energy Environ. Sci.* 11 (2018) 641–647. <https://doi.org/10.1039/c7ee03340k>.
- [119] W. Hadibrata, F. Es, S. Yerci, R. Turan, Ultrathin Si solar cell with nanostructured light trapping by metal assisted etching, *Sol. Energy*

- Mater. Sol. Cells. 180 (2018) 247–252. <https://doi.org/10.1016/j.solmat.2017.06.029>.
- [120] S. Wang, B.D. Weil, Y. Li, K.X. Wang, E. Garnett, S. Fan, Y. Cui, Large-area free-standing ultrathin single-crystal silicon as processable materials, *Nano Lett.* 13 (2013) 4393–4398. <https://doi.org/10.1021/nl402230v>.
- [121] S. Zhou, Z. Yang, P. Gao, X. Li, X. Yang, D. Wang, J. He, Z. Ying, J. Ye, Wafer-Scale Integration of Inverted Nanopyramid Arrays for Advanced Light Trapping in Crystalline Silicon Thin Film Solar Cells, *Nanoscale Res. Lett.* 11 (2016). <https://doi.org/10.1186/s11671-016-1397-6>.
- [122] S. Rasool, Q.V. Hoang, D. Van Vu, C.E. Song, H.K. Lee, S.K. Lee, J.C. Lee, S.J. Moon, W.S. Shin, High-efficiency single and tandem fullerene solar cells with asymmetric monofluorinated diketopyrrolopyrrole-based polymer, *J. Energy Chem.* 64 (2022) 236–245. <https://doi.org/10.1016/j.jechem.2021.04.032>.
- [123] K. Deepthi Jayan, Enhancement of efficiency of (FA)₂BiCuI₆ based perovskite solar cells with inorganic transport layers, *Opt. Mater.* 122 (2021) 111671. <https://doi.org/10.1016/j.optmat.2021.111671>.
- [124] S.J. Ko, Q.V. Hoang, C.E. Song, M.A. Uddin, E. Lim, S.Y. Park, B.H. Lee, S. Song, S.J. Moon, S. Hwang, P.O. Morin, M. Leclerc, G.M. Su, M.L. Chabinye, H.Y. Woo, W.S. Shin, J.Y. Kim, High-efficiency photovoltaic cells with wide optical band gap polymers based on fluorinated phenylene-alkoxybenzothiadiazole, *Energy Environ. Sci.* 10 (2017) 1443–1455. <https://doi.org/10.1039/c6ee03051c>.
- [125] U. Aeberhard, A. Schiller, Y. Masson, S.J. Zeder, B. Blülle, B. Ruhstaller, Analysis and Optimization of Organic Tandem Solar Cells by Full Opto-Electronic Simulation, *Front. Photonics.* 3 (2022) 1–12. <https://doi.org/10.3389/fphot.2022.891565>.
- [126] M.K. Hossain, M.H.K. Rubel, G.F.I. Toki, I. Alam, M.F. Rahman, H. Bencherif, Effect of Various Electron and Hole Transport Layers on the Performance of CsPbI₃-Based Perovskite Solar Cells: A Numerical Investigation in DFT, SCAPS-1D, and wxAMPS Frameworks, *ACS Omega.* 7 (2022) 43210–43230. <https://doi.org/10.1021/acsomega.2c05912>.
- [127] M.R. Jani, M.T. Islam, S.M. Al Amin, M.S. Us Sami, K.M.

- Shorowordi, M.I. Hossain, S. Chowdhury, S.S. Nishat, S. Ahmed, Exploring solar cell performance of inorganic Cs₂TiBr₆ halide double perovskite: A numerical study, *Superlattices Microstruct.* 146 (2020) 106652. <https://doi.org/10.1016/j.spmi.2020.106652>.
- [128] A. Basak, U.P. Singh, Numerical modelling and analysis of earth abundant Sb₂S₃ and Sb₂Se₃ based solar cells using SCAPS-1D, *Sol. Energy Mater. Sol. Cells.* 230 (2021) 111184. <https://doi.org/10.1016/j.solmat.2021.111184>.
- [129] Y. Xiao, H. Wang, H. Kuang, Numerical simulation and performance optimization of Sb₂S₃ solar cell with a hole transport layer, *Opt. Mater.* 108 (2020) 110414. <https://doi.org/10.1016/j.optmat.2020.110414>.
- [130] F. Ayala-Mató, O. Vigil-Galán, M.M. Nicolás-Marín, M. Courel, Study of loss mechanisms on Sb₂(S_{1-x}Se_x)₃ solar cell with n-i-p structure: Toward an efficiency promotion, *Appl. Phys. Lett.* 118 (2021). <https://doi.org/10.1063/5.0032867>.
- [131] X. Wang, J. Li, W. Liu, S. Yang, C. Zhu, T. Chen, A fast chemical approach towards Sb₂S₃ film with a large grain size for high-performance planar heterojunction solar cells, *Nanoscale.* 9 (2017) 3386–3390. <https://doi.org/10.1039/c7nr00154a>.
- [132] J. Werner, C.H. Weng, A. Walter, L. Fesquet, J.P. Seif, S. De Wolf, B. Niesen, C. Ballif, Efficient Monolithic Perovskite/Silicon Tandem Solar Cell with Cell Area >1 cm², *J. Phys. Chem. Lett.* 7 (2016) 161–166. <https://doi.org/10.1021/acs.jpcelett.5b02686>.
- [133] M.A. Green, E.D. Dunlop, J. Hohl-Ebinger, M. Yoshita, N. Kopidakis, K. Bothe, D. Hinken, M. Rauer, X. Hao, Solar cell efficiency tables (Version 60), *Prog. Photovoltaics Res. Appl.* 30 (2022) 687–701. <https://doi.org/10.1002/pip.3595>.
- [134] Y. Cheng, L. Ding, Perovskite/Si tandem solar cells: Fundamentals, advances, challenges, and novel applications, *SusMat.* 1 (2021) 324–344. <https://doi.org/10.1002/sus2.25>.
- [135] K. Amri, R. Belghouthi, M. Aillerie, R. Gharbi, Device optimization of a lead-free perovskite/silicon tandem solar cell with 24.4% power conversion efficiency, *Energies.* 14 (2021). <https://doi.org/10.3390/en14123383>.
- [136] M. Bacha, A. Saadoune, I. Youcef, O. terghini, Design and numerical investigation of Perovskite/Silicon tandem solar cell, *Opt. Mater.* 131

- (2022) 112671. <https://doi.org/10.1016/j.optmat.2022.112671>.
- [137] M. Mousa, M.M. Salah, F.Z. Amer, A. Saeed, R.I. Mubarak, High Efficiency Tandem Perovskite/CIGS Solar Cell, 2020 2nd Int. Conf. Smart Power Internet Energy Syst. SPIES 2020. (2020) 224–227. <https://doi.org/10.1109/SPIES48661.2020.9242927>.

على معايير الأداء لسلكيين مختلفين للطبقة الممتصة السفلية. عند نقطة تطابق التيار المصممة لكل حالة، تم تحقيق الكفاءة المثلى مما أعطى شدة تيار ١٧,٢٤ مللي أمبير لكل سنتيمتر مربع و كفاءة ٢٣,٢٥٪ لسلك ٣٠ ميكرومتر للطبقة الممتصة السفلية بينما كانت شدة التيار ١٨,٠٤ مللي أمبير لكل سنتيمتر مربع وكانت الكفاءة ٢٤,٣٤٪ لسلك ٥٠ ميكرومتر للطبقة الممتصة السفلية.

(٣) الخلية التراكبية (Polymer/Si) تحتوى على خلية فرعية علوية قائمة على البوليمر و خلية فرعية سفلية سليكونية رقيقة. الطبقة النشطة ضوئيًا للخلية الفرعية العلوية هي مزيج من (PDTBTBz-2F) كمانح من البوليمر و (PC₇₁BM) كمستقبل من الفوليرين. في البداية، تم إجراء معايرة للخليتين الفرعيتين مقابل دراسات تجريبية و كانت كفاءة التحويل ١٠٪ للخلية الفرعية العليا و ١٤,٢٦٪ للخلية الفرعية السفلية. عند دمج الخليتين في خلية ترادفية متجانسة، تم الحصول على كفاءة تحويل طاقة بنسبة ١٦,٥٨٪ و شدة تيار ١٣,٣٩ مللي أمبير لكل سنتيمتر مربع. بعد ذلك، تم تحسين أداء الخلية من خلال التحكم فى فرق مستوى حزمة التكافؤ (VBO) للخلية العلوية. علاوة على ذلك، قمنا بفحص تأثيرات كثافة العزل للطبقة الممتصة العلوية وكذلك سمك كلا الطبقتين الممتصتين لتحقيق أفضل أداء للخلية. بعد تحسين وتصميم نقطة تطابق التيار، تم تحسين شدة التيار و كفاءة تحويل الطاقة للخلية الترادفية إلى ١٦,٤٢ مللي أمبير لكل سنتيمتر مربع و ٢٤,٢١٪ على التوالي.

تهدف تلك الدراسات إلى تقديم خلايا شمسية تراكبية مبنية على تصميم رقيق كليًا و الذى قد يكون مناسبًا لتطبيقات مثل الإلكترونيات المرنة.

ملخص الرسالة باللغة العربية

أصبحت الخلايا الشمسية مصدرًا أساسياً ومستداماً للطاقة في السنوات الأخيرة. تقوم هذه الخلايا بتحويل ضوء الشمس مباشرة إلى كهرباء ويمكن استخدامها لتشغيل مجموعة واسعة من التطبيقات، من الأجهزة المنزلية الصغيرة إلى المجمعات الصناعية الكبيرة. نتيجة لذلك، أصبحت الخلايا الشمسية خيارًا شائعًا بشكل متزايد لكل من التطبيقات السكنية والتجارية، مما يساهم في مستقبل أنظف وأكثر استدامة. كُرست الأطروحة الحالية لدراسة ثلاث خلايا تراكيبية جديدة باستخدام تقنية المحاكاة العددية TCAD وهي:

(١) الخلية التراكيبية (All-BaSi₂) تحتوى على خلية فرعية سفلية BaSi₂ ذات فجوة طاقة مقدارها ١,٣ إلكترون فولت و خلية فرعية علوية Ba(C_xSi_{1-x})₂ ذات فجوة طاقة متغيرة قابلة للضبط. ثبت أن الخلية الفرعية العليا ذات فجوة ١,٨ إلكترون فولت هي الخيار الأمثل للحصول على الحد الأقصى لكفاءة تحويل الطاقة بنسبة ٣٠٪. بعد ذلك، تم تحسين أداء الخلية التراكيبية من خلال دراسة تأثير كثافة الإشابة وسمك كلا الطبقتين الممتصتين. علاوة على ذلك، تم تغيير سمك الخلية العلوية في النطاق من ٠,٨٥ إلى ١,٢٥ ميكرومتر للحصول على نقطة تطابق التيار وزيادة كفاءة تحويل الطاقة إلى ٣٢,٨٣٪. بالإضافة إلى ذلك، قمنا بدراسة تأثير كلا من كثافة العلل للممتصات، ودالة شغل موصلات الخلية على معايير الأداء.

(٢) الخلية التراكيبية (Sb₂S₃/Si) تحتوى على خلية فرعية سفلية سليكونية رقيقة ذات فجوة طاقة ١,١٢ إلكترون فولت و خلية فرعية علوية Sb₂S₃ ذات فجوة طاقة ١,٧ إلكترون فولت. تم التوصل إلى كفاءة تحويل الطاقة للخلايا العلوية و السفلية المستقلة المعايير بمقدار ٤,٣١٪ و ١٤,٢٦٪ على التوالي. عند دمج الخليتين في خلية ترادفية متجانسة، تم تحقيق كفاءة تحويل طاقة بنسبة ١٠,١٠٪، مما يعني أنه يجب تحسين الخلية العلوية من أجل تجاوز كفاءة التحويل للخلية السفلية. وبالتالي، تم تحسين الخلية Sb₂S₃ من خلال تصميم الخلية بدون طبقة نقل الفجوات العضوية (HTL) وضبط فرق مستوى حزمة التوصيل (CBO) بين طبقة نقل الإلكترونات (ETL) و الممتص العلوى Sb₂S₃. بعد ذلك، تم تحسين الخلية الترادفية بدءًا من سمك وكثافة الإشابة لطبقة ETL للخلية العلوية. أيضًا، تم دراسة تأثير كثافة علل الطبقة الممتصة ومقاومة التوالى للخلية العلوية على أداء الخلية الترادفية للوصول للحد الأقصى المتاح من الكفاءة. عند خفض كثافة العلل ومقاومة التوالى، تحسنت الكفاءة الإجمالية للخلية الترادفية إلى ١٩,٥١٪. علاوة على ذلك، تم دراسة تأثير سمك طبقتي الامتصاص العلوية والسفلية على أداء الخلية. بالإضافة إلى ذلك، قمنا بدراسة تأثير سمك الطبقة الممتصة العلوية

قامت اللجنة الموقعة أدناه بتحكيم الرسالة تحت عنوان

خلايا شمسية مبتكرة متعددة الطبقات مبنية على ركائز من السيليكون

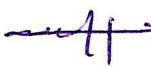
المقدمة من

المهندس/ محمد عقيل شوقي عبدالوهاب

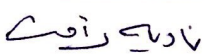
درجة الماجستير فى الفيزياء الهندسية - كلية الهندسة ببها - جامعة بنها (٢٠١٩)

كجزء من متطلبات الحصول علي درجة دكتوراه الفلسفة في العلوم الهندسية في
الفيزياء الهندسية

أعتمدت و أجازت من لجنة الحكم و المناقشة

(رئيساً) 


أ.د/ وائل فكرى فاروق فكرى
أستاذ متفرغ بقسم الفيزيكا والرياضيات الهندسية
كلية الهندسة - جامعة عين شمس

(عضواً) 


أ.د/ نادية حسين رأفت أحمد
أستاذ بقسم الرياضيات والفيزيكا الهندسية
كلية الهندسة - جامعة القاهرة

(عضواً) 

أ.د/ طارق محمد عبدالقادر حسن
أستاذ بقسم العلوم الهندسية الأساسية
كلية الهندسة ببها - جامعة بنها

(عضواً) 

أ.د/ أحمد شاكر أحمد غزالة
أستاذ بقسم الفيزيكا والرياضيات الهندسية
كلية الهندسة - جامعة عين شمس

(رئيس القسم) 

أعتمدت من قسم العلوم الهندسية الأساسية
أ.د/ طارق محمد عبدالقادر حسن

(وكيل الكلية للدراسات العليا)

أعتمدت من الدراسات العليا
أ.د/ أشرف يحيى حسن على



أعتمدت من الكلية
أ.د/ السيد على إبراهيم فؤاد

قامت اللجنة الموقعة أدناه بتحكيم الرسالة تحت عنوان

خلايا شمسية مبتكرة متعددة الطبقات مبنية على ركائز من السيليكون

المقدمة من

المهندس/ محمد عقيل شوقي عبدالوهاب

درجة الماجستير فى الفيزياء الهندسية – كلية الهندسة ببناها – جامعة بنها (٢٠١٩)

كجزء من متطلبات الحصول علي درجة دكتوراه الفلسفة في العلوم الهندسية في
الفيزياء الهندسية

أُعتمدت و أُجيزت من لجنة الحكم و المناقشة

(رئيساً)	أ.د/ وائل فكرى فاروق فكرى أستاذ متفرغ بقسم الفيزيكا والرياضيات الهندسية كلية الهندسة – جامعة عين شمس
(عضواً)	أ.د/ نادية حسين رأفت أحمد أستاذ بقسم الرياضيات والفيزيكا الهندسية كلية الهندسة – جامعة القاهرة
(عضواً)	أ.د/ طارق محمد عبدالقادر حسن أستاذ بقسم العلوم الهندسية الأساسية كلية الهندسة ببناها – جامعة بنها
(عضواً)	أ.د/ أحمد شاكر أحمد غزالة أستاذ بقسم الفيزيكا والرياضيات الهندسية كلية الهندسة – جامعة عين شمس
(رئيس القسم)	أ.د/ طارق محمد عبدالقادر حسن أُعتمدت من قسم العلوم الهندسية الأساسية
(وكيل الكلية للدراسات العليا)	أ.د/ أشرف يحيى حسن على أُعتمدت من الدراسات العليا
(عميد الكلية)	أ.د/ السيد على إبراهيم فؤاد أُعتمدت من الكلية



جامعة بنها
كلية الهندسة بنها
قسم العلوم الهندسية الأساسية

خلايا شمسية مبتكرة متعددة الطبقات مبنية على ركائز من السيليكون

الرسالة مقدمة للحصول علي درجة دكتوراه الفلسفة في العلوم الهندسية في
الفيزياء الهندسية

إعداد

المهندس/ محمد عقيل شوقي عبد الوهاب

درجة الماجستير في الفيزياء الهندسية – كلية الهندسة بنها – جامعة بنها (٢٠١٩)

المشرفون

أ.د/ أحمد شاكر أحمد غزالة
أستاذ بقسم الفيزيكا والرياضيات الهندسية
كلية الهندسة
جامعة عين شمس

أ.د/ طارق محمد عبدالقادر حسن
أستاذ بقسم العلوم الهندسية الأساسية
كلية الهندسة بنها
جامعة بنها

د/ إبراهيم سيد أحمد إبراهيم ماجد
مدرس بقسم العلوم الهندسية الأساسية
كلية الهندسة بنها
جامعة بنها

بنها ٢٠٢٣